ESTIMATION AND CONTROL OF LATERAL TIRE FORCES USING STEERING TORQUE

A DISSERTATION
SUBMITTED TO THE DEPARTMENT OF MECHANICAL ENGINEERING
AND THE COMMITTEE ON GRADUATE STUDIES
OF STANFORD UNIVERSITY
IN PARTIAL FULFILLMENT OF THE REQUIREMENTS
FOR THE DEGREE OF
DOCTOR OF PHILOSOPHY

Yung-Hsiang Judy Hsu
March 2009

I certify that I have read this dissertation and that, in my opinion, it is fully adequate in scope and quality as a dissertation for the degree of Doctor of Philosophy.

(J. Christian Gerdes)
Principal Advisor

I certify that I have read this dissertation and that, in my opinion, it is fully adequate in scope and quality as a dissertation for the degree of Doctor of Philosophy.

(John B. Ferris)

I certify that I have read this dissertation and that, in my opinion, it is fully adequate in scope and quality as a dissertation for the degree of Doctor of Philosophy.

(Stephen M. Rock)

Approved for the University Committee on Graduate Studies.

Dedicated to my mother, my father and Jessica.

Abstract

Over the past few decades, vehicle control systems have been developed to enhance vehicle handling and passenger safety. These systems seek to prevent unintended vehicle behavior through active vehicle control, assisting drivers in maintaining control of their vehicles. Unfortunately, these systems are limited by the lack of knowledge of the vehicle's state and operating conditions. Knowledge of the vehicle's sideslip angle, which relates its lateral velocity to its longitudinal velocity, is important information that is largely unavailable for current safety systems. The tire's lateral handling limit, which is the maximum grip a tire has on the road during a turn, is also generally unknown. As a result, current systems are reactive; they must detect a problem before corrective action can be taken. If onboard systems had accurate knowledge of sideslip angle (or equivalently, tire slip angle) and could predict the peak friction limit, control systems could anticipate rather than react to loss of control situations, further enhancing vehicle handling and increasing passenger safety.

This thesis presents several model-based estimation methods which utilize the early lateral limit information contained in steering torque measurements and the added sensing capability of GPS. During periods of GPS signal loss, a nonlinear observer is developed that utilizes pneumatic trail information in steering torque to identify both vehicle sideslip angle and the lateral force limits. Mathematically guaranteed to converge, the nonlinear observer uses readily available measurements on production vehicles. Most importantly, it takes advantage of the friction information encoded in the tire pneumatic trail, enabling early detection of the limits *before* they are reached. Finally, this work develops an envelope controller to keep the vehicle in a safe operating region using the estimated handling limit information from

the nonlinear observer. Theoretical results are confirmed by implementation on an experimental steer-by-wire vehicle. Testing conditions include maneuvers performed on dry, flat paved road, as well as on lower-friction, dry gravel.

Acknowledgments

I had a lot of help both during my graduate career and on the path leading up to it.

First to my advisor, Chris Gerdes, who in the span of five and a half years helped shape me from a wide-eyed, unsure graduate student to a confident and capable researcher. Never did I understand the importance of feeling comfortable collaborating with and speaking honestly to your advisor until I witnessed the struggle students around me went through without it. During my time at Stanford, Chris has become a lifelong friend and mentor, someone I could always approach during the good times and the bad. I admire his intellectual curiosity, the gifted way he connects and relates to students, his empathy, and leadership.

I am grateful to all of the professors on my defense committee. Professor Mark Cutkosky, who has seen me wander in and out of his lab for years, thankfully agreed to sit on my committee and get acquainted with my research. Professor Pam Hinds graciously chaired the committee, asking me thoughtful questions and bringing a refreshing perspective to my work. A heartfelt thanks to my dissertation reading committee, Professor John Ferris from Virginia Tech and Professor Steve Rock from the Stanford Aero/Astro Department. Their patience and willingness to read my thesis not only provided me with thorough and helpful feedback, but equally importantly ensured that more than two people would ever read this thesis. John offered his wealth of vehicle suspension and dynamics knowledge to more clearly introduce the technical foundation in Chapters 1 and 2, while Steve's wise suggestions enabled me to better tie together the theme, ideas and results presented in this work.

Many people supported and enabled this research in other ways. Professor Dave Beach selflessly volunteered his time to videotape our vehicle test runs at multiple

proving grounds. When he wasn't editing the footage himself, Dave cordially taught me how to use the video editing software to create effective video documentation and better present the experimental implementation of the nonlinear observer and envelope controller. Thanks go out to the kind Stanford teaching and support staff, without whose assistance I would not have been able to successfully execute or complete the research: Craig Milroy, Scott Sutton, Denise Curti, Jennifer Rahn, and Bernice Marshall.

The collaboration with our Nissan research sponsors Tadashi Suzuki, Katsunori Oshiage, Deguchi Yoshitaka, and Shinichiro Joe was one of the highlights of the entire research process. Their support shaped the technical purpose of this work, while their thoughtful hospitality during our visit to Japan introduced me to the culinary delights of Kobe beef, tender smoked cuttlefish, and refreshing mochi-like cold jello dessert, as well as to the once-confusing concept of "women only" floors in Japanese business hotels.

In educating myself on matters beyond engineering, I have incurred a great many debts. My graduate school experience would not be complete without acknowledging the great impact Professor Sheri Sheppard has had on not only myself, but on engineering graduate women as a whole. By forming a wonderful support community in the ME Women's Group, as well as founding the Women's Perspectives in Engineering seminar E311A, Sheri has enabled us to learn lessons about what is really meaningful in life, how to make difficult decisions, and how to overcome professional and personal hardships. Thanks, also, to the women who I was fortunate enough to meet through ME Women's Group: Julia Chen, Christie Draper, and Misty Davies.

An important benefit of graduate school is having the freedom to delve into one's extracurricular passions and endeavors. Three years of my time at Stanford was spent reconnecting with my Chinese heritage and learning the intricacies of the Chinese language. This effort fulfilled a void that I had long buried inside of me after struggling to adjust to my own identity as an Asian-American living here in the States. Among my most influential Chinese language teachers have been Professors Nina Lin, Marina Chung, and Huazhi Wang. They exhibited stellar patience and kindness, enabling me

to go from an shaking, verbally incontinent stutterer to a more developed, more confident speaker, reader and writer. My experience culminated with a summer in which I lived and researched in Beijing, China as part of the Stanford-Tsinghua graduate engineering exchange program. This opportunity would not have been possible without the program organizers Pam Hinds, Marta Espinoza, and Xiaohong Shen, and the remarkable support of my advisor Chris. The Stanford and Tsinghua student cohorts with whom I am thankful to have shared this amazing experience: my exchange program partner Shengbo Li, Stephanie Claussen, Quan Gan, Andrew Chang, Yang Chen, Sheng Zhou. Thanks, too, to the Tsinghua researching group who welcomed me into their lab: Professor Keqiang Li, Professor Frank Luo, and Zhou Lei. I also would like to acknowledge all the friends I made through my involvement in the Rains CA Program (planning social events with them was a blast) and the Stanford 6th Man Club Basketball Committee (for years of heart stopping excitement and occasional heartbreak, and for getting me on TV!).

In an educational environment not exactly known for cultivating social relationships, I was lucky to be a member of the Dynamic Design Lab (DDL) family. As the first female PhD graduate of the DDL, I recognize the importance of having a supportive network within a male-dominated car-loving field. Everyone I had the benefit of working with in the DDL is technically gifted, yes, but also kind enough to volunteer their time to help out anyone in need. My graduate career would not have been possible without the assistance and guidance of our many lab alumni: Paul Yih, Hong Bae, Justin Reed, Matt Schwall, Chris Carlson, Eric Rossetter, Jihan Ryu, and Greg Shaver. I am especially grateful to alumni Josh Switkes and Chris Gadda who served as unofficial graduate mentors, showing me the ropes in an unfamiliar research setting and donating their time to help me debug code, fix P1 (again), or put out some other fire before an impending sponsor visit. I am very grateful to have worked with Shad Laws, my Nissan research partner in crime for three years and the second half of the unstoppable "Shudy." Shad somehow manages to just get things done, with both amazing brilliance and generosity. All of my labmates who worked on P1 together with me contributed in many ways, but I am most thankful for their dedication to sustain a our wonderfully cool yet terribly high-maintenance

research vehicle: Rami Hindiyeh, Mick Kritayakirana, Christoph Voser, and machining wizard Allegra Shum. I could not imagine my graduate career without the other members of the DDL who I will remember fondly: Kirstin Talvala, Craig Beal, Carrie Bobier, Nikhil Ravi, Matt Roelle, David Hoffert, Adam Jungkunz, Sam Chang, and Hsien-Hsin Liao. Thankfully, our lab was blessed with two incredible visiting scholars, Markus Maurer and Gerrit Schmidt, both so very German in their humor and magnificently warmhearted. Markus, with his wisdom and approachability, served as a second graduate advisor to me. Gerrit is one of the most charming people I know, and I look forward to our next game of Doppelkopf together even though he has a knack of effortlessly and amiably beating us foolish Americans.

In my path leading up to graduate school, I've incurred a great many debts. My undergraduate education at Harvey Mudd College taught me how to work hard, succeed and fail at academic research, work effectively in engineering teams, flourish under the guidance of faculty, be humbled by people much smarter than yourself, and find my passion for leadership and interdisciplinary collaboration. I was fortunate to have not one, but two marvelous undergraduate mentors: Professors Lori Bassman and Jenn Rossmann. Both had a large part in my even applying to graduate school, and both taught me more about how to keep myself on a whole and proper path through life than they will ever know. With her dedication to our chapter of SWE, opening her home to host SWE sleepovers and making her famous oatmeal chocolate chip cookies, and her mentorship when times got very hard during my PhD, Lori is someone I will always look up to for her success and enduring impact on every student she interacts with. Words can't express the influence Jenn had me. She helped build my confidence, instilled in me lessons on the importance of a strong work ethic and good oral and written communication skills, and most of all, why personal fulfillment and happiness with your loved ones is far more important than any financial reward or professional triumphs. I profited from the excellent teaching from my other beloved Mudd faculty: Professors Philip Cha, Anthony Bright, Ziyad Duron, Patrick Little, Francis Su, and Thomas Donnelly.

My family is my foundation, providing me with the stability that has enabled me to continue to grow. First, to my mother, who I take after more than I would

have ever expected. I thank her for being my first and most influential role model. She was an early pioneer obtaining her PhD in Mechanical Engineering at a time when very few were, has the admirably strong will, and I would consider myself lucky if I become half the accomplished cook she is today. I may resemble her physical appearance from her younger days, but the most similarities reside inside, with our self-assuredness, thirst for knowledge, ambition, and capacity to love and nurture. My father, with his Civil Engineering doctorate, is no less accomplished. I admire his dedication to support of our family and each of our dreams, teaching me how to make life decisions using a scientific lens, and introducing me to the joys of anything seafood or spicy, traveling the world, bridge and mahjong. And finally my life would not be whole without my sister Jessica, who has come a long way from trying to suffocate me by throwing a pillow into my crib when I first arrived on the scene (our sibling jealously soon disappeared). Jess somehow dodged the engineering bullet and became the only *real* doctor in the family. She is my best friend and will always be the person I turn to for advice and sympathy. From our younger days when I annoyingly copied everything she wore, to as adults picking up the phone to plan our next tropical vacation together, I am eternally thankful I ended up with the best sister I could have wished for.

Finally, in life, one hopes for solid friendships and companionship. In my life, I have been able to build an extended family from the friendships I cultivated in grad school: my best friend and roommate Karlin Bark, the passionate and savvy Aneeta Rattan, the insightful and thoughtful Shantal Marshall, and the loving and joyful Julie Litzenberger. These wonderful ladies have always been in my corner. As a group, we are always ready to celebrate each of our successes and without hesitation rush in during our times of need. I want to especially thank Karlin for helping me survive this sometimes torturous academic marathon, and leading by example with her incredible consideration for others and, of course, sharing my love for good food and boba. Other great friends who helped me survive and enjoy this PhD adventure: Melinda Kong and Kim Nguyen (all those fun nights in the city, either rolling down hills or dancing the night way), Aaron Parness (who let me shave his head and chatted about our days over regular tea breaks) and Sanjay Dastoor (Fleischlos, anyone?). And finally,

to the caring men in my life who I've learned so much from and attribute much of my happy memories to, I am forever grateful: Tom Galvani, Charles Hudson and Matt Boswell. Thank you.

Contents

List of Tables

List of Figures

Chapter 1

Introduction

1.1 Motivation

Automobiles have become indispensable in our modern society. Consequently, vehicle safety has tremendous importance in our everyday lives. For some perspective, in the United States, motor vehicle crashes continue to be the leading cause of death for children, teens, and young adults [40, 45]. Worldwide, an estimated 1.2 million people are killed in road crashes each year and as many as 50 million are injured. Projections indicate that this will increase by about 65% over the next 20 years unless there is new commitment to prevention [46].

Over the past few decades, vehicle control systems have been developed to enhance vehicle handling and passenger safety. These systems seek to prevent unintended vehicle behavior through active vehicle control and assisting drivers in maintaining control of their vehicles. Among them, Anti-lock Brake Systems (ABS), Traction Control Systems (TCS), and Electronic Stability Control (ESC) (also known as Electronic Stability Program) are examples of automotive braking technologies that have improved handling and helped drivers avoid potentially dangerous situations.

ABS was the first of a series of three braking technology developments. ABS is a four-wheel system that prevents wheel lock-up by automatically modulating the brake pressure when the driver makes an emergency stop. Bosch and Mercedes-Benz introduced the first completely electronic 4-wheel multi-channel ABS system in

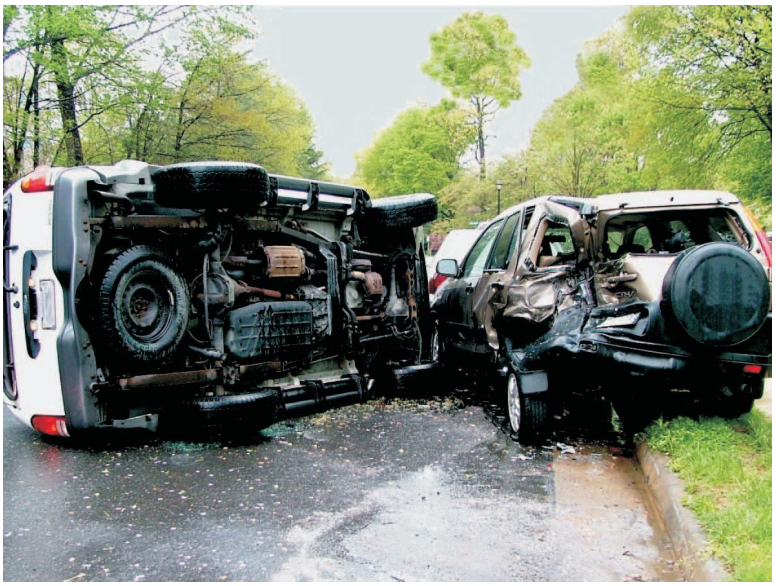

Figure 1.1: A Vehicle Crash [39]

trucks and the Mercedes-Benz S-Class in 1978, and in 2004 roughly 70% of vehicles worldwide have been equipped with ABS technology [2]. TCS, also known as Anti-Slip Regulation (ASR), was developed later to prevent loss of traction of the vehicle's driven wheels during acceleration.

ESC evolved from ABS and TCS, but incorporated important additional capabilities. ESC is a integrated with the vehicle's braking system and drivetrain and is designed to improve a vehicle's lateral stability by electronically detecting and automatically assisting drivers in dangerous situations (e.g., limit understeer and oversteer) and under unfavorable conditions (e.g., rain, snow, sleet, ice). ESC systems have sensors which monitor vehicle speed, steering wheel angle, yaw rate, and lateral acceleration [2, 63]. Data from the sensors are used to compare a driver's intended yaw rate with the vehicle's actual yaw rate to detect when a driver has lost control of a vehicle. It automatically intervenes by applying the brakes to individual wheels and possibly reducing engine torque to provide stability.

For example, if during a turn a vehicle's front wheels have begun to lose traction (i.e. limit understeering), ESC may brake the inside rear wheel, applying a torque to

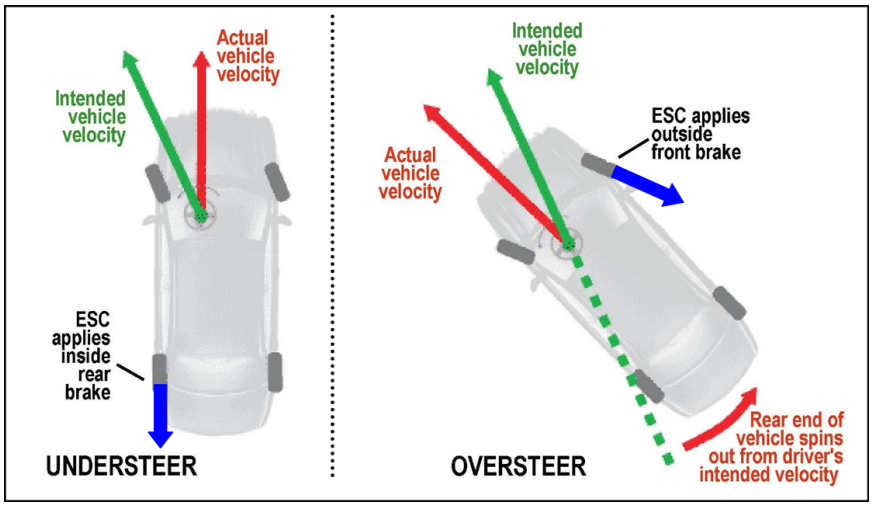

Figure 1.2: Electronic Stability Control [9]

correct the vehicle's orientation. The main task of ESC as an active safety system, however, is to prevent vehicle spin. If an ESC system detects that the rear wheels have begun to lose traction (i.e. limit oversteering), it may momentarily brake the outside front wheel, imparting a corrective torque to counteract the excessive yaw and stabilize the vehicle (see Fig 1.2). Depending on the driving situation, these brake interventions may also be used to slow down the vehicle. In 1995, Bosch first released ESC for the Mercedes-Benz S-Class sedan, and it was later installed in all models by Mercedes-Benz and BMW as standard equipment by 2000 and 2001, respectively [2]. Since its introduction, ESC has had a tremendous impact on vehicle safety [33]. Experts estimate, for instance, that ESC prevents 27% of loss of control accidents and reduces single-vehicle crashes rates by 36% by intervening when emergency situations are detected [1, 5].

While current vehicle safety systems such as ESC are unquestionably life-saving technologies, they are unfortunately limited by the lack of knowledge of the vehicle's state and operating conditions. Knowledge of the vehicle's sideslip angle, which is the angle between the vehicle's heading direction and actual velocity, is important information that is largely unavailable for current safety systems. The tire's lateral handling limits, which is the maximum potential grip a tire has on the road during a

turn, are also generally unknown.

As a result of this limited information, production stability control systems rely on detecting a difference between intended and actual vehicle yaw rate before the system can intervene [2, 63]. In other words, current systems are reactive; they must detect a problem before corrective action can be taken. If onboard systems had accurate knowledge of sideslip angle (and therefore tire slip angle) and could predict the peak lateral force limits, control systems could anticipate rather than react to loss of control situations, further enhancing vehicle handling and increasing passenger safety [63].

In addition to improving current safety systems, safety systems of the future would also greatly benefit from information on the vehicle's state and operating conditions. Future vehicles will likely have added actuator capability, such as four-wheel independent steer, drive or brake systems [16, 19, 36, 54, 66, 67]. Increased actuators enable active control of individual tire force generation. This opens exciting new avenues to more easily stabilize and control vehicle motion. Taken one step further, future safety systems could actively anticipate and prevent unexpected vehicle motion *before* the driver enters a dangerous situation. However, in order to realize this potential, knowledge of the tire's lateral handling limits is required well before the limits are reached. This motivates the importance of estimating the vehicle's state and road conditions predicatively and reliably.

Recently, researchers have looked at utilizing a new source of information for estimation: steering torque. Steering torque is the total torque about a tire's steer axis resulting from tire forces, the driver, and/or steering actuators. Steering torque measurements are available in research vehicles with steer-by-wire or production vehicles with Electric Power Steering (EPS) or Active Steering. It contains tire pneumatic trail information, which provides early limits detection well before tire force saturation [43]. Just as a skilled driver can sense the limits of tire adhesion through the steering wheel feel, steering torque is a promising new source of information for estimating the vehicle's lateral handling capability for safety systems.

Given early information of a vehicle's lateral limits, even with changing road conditions or tire properties, we can begin to imagine a more holistic approach to ensure vehicle safety. In aviation, a well-known integrated control strategy is envelope

protection (also known as carefree handling). Envelope protection uses available actuators to prevent an aircraft from entering state or control regions outside of the safe flight regime [41, 62]. Limitations are often imposed on an aircraft's state, such as angle of attack, airspeed, bank angle and altitude [65]. Modern military and commercial aircraft, including Airbus Industrie's A320, A330, and A340 series and Boeing's 777, all have onboard envelope protection systems that aim to keep the aircraft within a safe and controllable flight region [11, 41].

The idea of envelope protection, or envelope control, could similarly be extended to land vehicles [36]. During normal driving, drivers would be able to freely maneuver the vehicle. However, if there is danger of crossing the limits, the controller would engage and assist the driver in staying within operating bounds.

Previously out of reach due to a lack of information of the vehicle state and operating limits, vehicle driver assistance systems of the future could use available actuators – such as active steering, differential braking or active camber – to keep the vehicle within a safe operating envelope. Of course, just as with flight envelope protection, vehicle envelope control requires certain design considerations. The design choices made during the development of an envelope control system would rely heavily on how well the operating limits of the vehicle are understood. In addition, thoughtful design choices of how to use limited actuation ability, and how to trade off between coupled (and sometimes competing) objectives are among some of the difficulties that need to be addressed with an integrated control approach.

Overall, with improved knowledge of the vehicle's state and operating conditions, and with a coordinated approach to prevent unsafe vehicle trajectories, safety systems have an even greater potential to prevent vehicle accidents and reduce crash fatalities.

1.2 Background on Lateral Force

The motion of a vehicle is governed by the forces generated between the tire and the road. Lateral tire force (also known as side or cornering force) is the force necessary to hold a vehicle through a turn. It is generated by lateral tire deformation in the contact patch, as illustrated in Fig. 1.3. The angle of deformation, or the difference

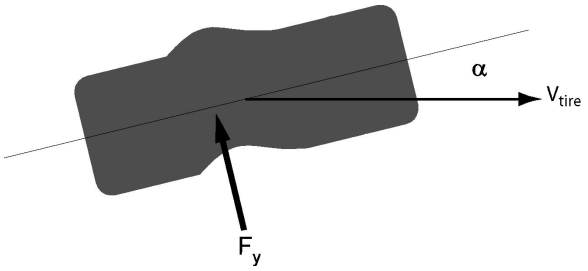

Figure 1.3: Lateral Tire Deformation

between the tire's heading and velocity, is known as the tire slip angle.

Lateral tire force F_y is in general a nonlinear function of the tire slip angle α. In the simplest nonlinear representation of the tire curve, lateral force can described by three parameters: cornering stiffness, tire-road coefficient of friction, and normal force (See Fig. 1.4). The relationship between side force and slip angle is initially linear, with a constant slope determined by the cornering stiffness C_α. This region of handling is referred to as the linear operating region. As slip angle grows, eventually the force starts to saturate due to limited friction on the road, entering the nonlinear region. In the absence of longitudinal forces, the limits of handling are defined by the maximum available lateral force, μF_z, where μ is the tire-road friction coefficient and F_z is the tire vertical force.

Conceptually, cornering stiffness is a property of the tire (and to a lesser extent the road surface due to changes in the tire contact patch area), and changes slowly with time due to tire wear, inflation pressure, and temperature fluctuations [52]. On the other hand, tire-road friction can change quickly. It depends on road surface type (e.g., asphalt, gravel, dirt) and conditions (e.g., dry, wet, icy). Normal force changes statically due to suspension tuning and onboard vehicle loading, and dynamically with longitudinal and lateral weight transfer and road bank or grade. And finally, tire slip angle changes dynamically as a function of steer angle, as well as the vehicle's lateral motion and forward speed.

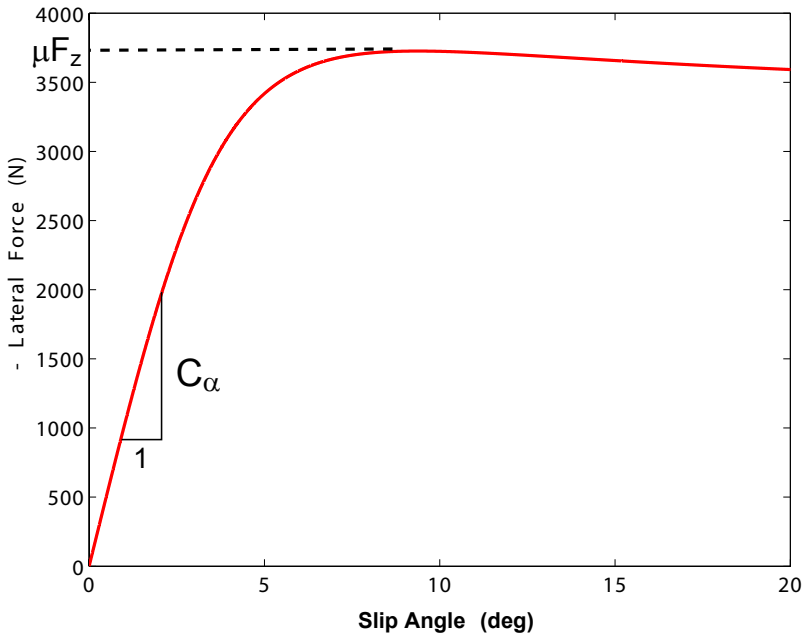

Figure 1.4: Generic Tire Curve

1.3 Existing Methodologies

1.3.1 Lateral Force Parameter Estimation

The problem of how to estimate the lateral force parameters has been an area of investigation in the vehicle dynamics community for over a decade [32, 34]. Tire slip angle, cornering stiffness, and tire-road friction, are in general not easily measured or modeled. In contrast, changes in tire vertical force can be modeled or measured easily. Therefore, previous work in the field has generally focused on how to estimate vehicle sideslip angle, which is related to tire slip angle through kinematics. Knowledge of slip angle can then be used to estimate cornering stiffness and friction. In this section, we give a brief overview of the existing techniques and approaches that have been developed in this area of study.

Sideslip Estimation

Current commercial safety systems, such as ESC, have access to measurements of lateral acceleration and yaw rate through onboard inertial sensors, but lack direct measurements of sideslip angle [63]. Previous approaches have attempted to estimate sideslip angle through sideslip rate integration. Sideslip rate is available through the following relationship:

$$a_y = V_x \left(\dot{\beta} + r \right) \tag{1.1}$$

where β is the sideslip angle at the vehicle's CG, V_x is the vehicle's longitudinal speed, a_y is the lateral acceleration, and r is the yaw rate. However, this relationship neglects the contribution of road grade, road bank and sensor biases. Thus, approaches which attempt to determine sideslip angle from sideslip rate integration are often prone to uncertainty and errors [18]. Other approaches have designed observers to estimate sideslip, but they often depend on accurate tire parametrization, which is problematic since tire parameters vary based on the road surface [28, 59, 64, 70].

An estimation approach that overcomes some of the drawbacks from previous approaches is the integration of inertial sensors with Global Positioning System (GPS) measurements. Bevly demonstrated that a combination of single-antenna GPS and Inertial Navigation System (INS) can provide accurate measurements of slip angle and cornering stiffness in the linear region of handling [7, 8]. Ryu showed that a combination of dual-antenna GPS and measurements can provide accurate sideslip estimates even in the presence of roll and pitch dynamics [49].

While GPS is inarguably useful in vehicle estimation algorithms, it is unfortunately not always available. GPS-based approaches require satellite visibility, which may be lost periodically in urban and forested driving environments. Furthermore, techniques which rely of sensors unavailable on production vehicles, such as dual-antenna GPS systems, are less likely to be adopted by automobile manufacturers. Because tire slip angle can change rapidly during emergency maneuvers, during periods of GPS signal loss, it is important to be able to estimate it *without* reliance on GPS.

Tire-Road Friction Estimation

Previous contributions in tire-road friction estimation generally face two main challenges: lack of sufficient excitation and reliance on sensors unavailable on production vehicles.

The first challenge is the persistence of excitation. Previous work has shown that either significant levels of longitudinal or lateral dynamics must be present before accurate estimation can begin. Matsuno attempted to identify tire-road friction based on a theoretical mapping between cornering stiffness and peak road friction coefficient [35]. Yet, cornering stiffness often varies significantly with tread wear, inflation pressure, temperature, normal load, and contact patch properties, all of which would make cornering stiffness based friction detection practically unreliable [52]. Several research groups propose that friction can be estimated from tire longitudinal stiffness at low values of slip ratio [23, 27, 47]. Nevertheless, experimental studies have shown that longitudinal stiffness estimates exhibit considerable sensitivity to tire inflation pressure, suggesting that any force-slip analysis must carefully consider a variety of factors before drawing any conclusions about the tire-road friction coefficient [10]. More recent methods developed rely on lateral force or lateral acceleration as an indication of friction limits [6, 21, 24]. Unfortunately, these methods necessitate a high level of lateral dynamics. In other words, the tires need to be near the limits of tire adhesion before friction can be identified. This is undesirable for stability control systems which often wish to intervene before the driver enters a dangerous situation.

The second challenge in friction estimation is relying on sensors that are available on production vehicles. Previously developed methods have the drawback of requiring costly sensor technology. For example, Hahn relies on GPS-based slip angle measurements to estimate both the coefficient of friction and cornering stiffness in real-time [24]. Pasterkamp developed an online neural-network based technique that uses lateral force and aligning torque measurements to estimate friction coefficient, although this approach relies on load-cells to measure tire vertical, longitudinal or lateral forces [44].

Motivated by this necessity, researchers have looked at steering torque as a new

source of information. Steering torque measurements are readily available in vehicles with steer-by-wire, EPS, or Active Steering systems. From steering torque, total aligning moment (the torque generated by lateral tire force) can be extracted easily. Because aligning moment decreases well before tire force saturation (due to its dependence on pneumatic trail), several approaches have been taken by Ono, Yasui and Endo to improve vehicle stability by limiting driver steering input once algorithms detect a noticeable decrease in self-aligning torque [15, 42, 68]. Their approaches unfortunately relied on linear observers for sideslip angle, which depend on accurate tire parametrization, and provided no direct determination of the friction limits. Finally, Nakajima demonstrated that steering torque can enhance ESC performance more than just relying on yaw rate measurements as an indication of vehicle instability [38]. Even though all of these methods recognized the value of total aligning moment as an early indication of exceeding the tire's lateral limits, none so far have provided explicit estimates of peak lateral force (or tire-road friction coefficient if normal force is known) and tire slip angle.

1.3.2 Envelope Control

As the control strategy in this thesis is inspired by envelope protection systems for aircraft, this section gives a brief discussion of previous work done in this area.

Envelope protection, also known as carefree handling, aims to prevent the aircraft from entering state or control regions outside of the safe flight regime. Limitations are often imposed on an aircraft's state, such as angle of attack, airspeed, bank angle and altitude [65]. Implementation of an envelope protection system can be divided into two necessary parts: "Limit Prediction" which detects the impending violation of the limit parameter, and "Limit Avoidance" where a preventive action is taken in the form of pilot cueing or autonomous limiting [50].

Envelope protection systems are commonly available on modern commercial aircraft. In 1998, Airbus Industrie launched envelope protection systems on all of their A320, A330 and A340 series fly-by-wire aircraft that prevent outside disturbances, or a pilot, from exceeding preset limits for angle-of-attack, speed, thrust asymmetry

and bank angles [11, 12]. The Boeing 777 has similar limits, except that the Boeing's strategy derives from the premise that pilots, not computers, should be the final authority in aircraft control. Their envelope protection system warns a pilot with aural and visual alarms when he or she reaches the envelope limits. The system will make it difficult, with increased yoke forces, for pilots to exceed the limits, but they will be able to do so if they persist [41].

Recently, researchers have made strides in improving aircraft envelope control technology. Sparks developed a decoupled wide envelope lateral/directional axes control design, separating gain-scheduling issues from aircraft performance issues [58]. Lapp used model predictive control to calculate optimal flight trajectories given a set of limitations and constraints (such as terrain), and Tomlin applied techniques of hybrid control for aerodynamic envelope protection and safe switching between flight modes [30, 60]. Work has also been done by Yavrucuk and Unnikrishnan to design methods that are adaptive to changing system configurations and support transient response limits [62, 69]. Finally, Sahani has extended aircraft envelope control methods to rotorcraft [51].

While envelope protection has been a well-known area of study in aviation, previous work in developing envelope protection system for production passenger vehicles is limited. This is largely due to the fact that vehicle driver assistance systems previously have lacked the "Limits Prediction" capability necessary for envelope control. Current stability control systems in production operate with incomplete information of the vehicle's state and lateral force limits [34, 63]. As a result, current stability control systems can only control quantities that are be directly measured or estimated reliably, such as yaw rate and sideslip rate (not sideslip angle), and do not consider tire-road friction limits [54, 66, 67]. However, controllers that aim to be robust to model uncertainties and parameter variation require an accurate estimate of sideslip angle [3, 4, 19]. It is this lack of state information has so far limited the application of holistic control strategies such as envelope protection on production vehicles.

1.4 Thesis Objectives

The primary focus of this thesis is the development and experimental validation of estimation methods which predict the lateral handling limits of a vehicle and estimates how close the vehicle is to approaching them. These estimation approaches all utilize the lateral limit information contained in steering torque measurements. In designing these methods, we set out to address two scenarios: when GPS measurements are available and when there are periods of GPS signal outage. When GPS is available, we have access to direct measurements of tire slip angle, which simplifies the estimation problem significantly [7, 8]. The GPS-based estimation approaches should satisfy the following criteria:

- Tire slip angle and peak lateral force limits should be estimated in real-time. Tire peak lateral force defines where the lateral limits are and slip angle quantifies how close the tire is to the limits. Thus, both quantities should be identified.
- In order to be of most use to vehicle control systems, the peak friction limits should be identified well before the force limits are exceeded. Thus, the methods should explore and capitalize on the predictive nature of tire pneumatic trail contained in steering torque measurements.
- The methods should be experimentally validated during a variety of driving conditions and maneuvers.

During periods of GPS signal loss, the estimation problem is more challenging. In addition to the criteria outlined above, a non-GPS based method must also satisfy the following:

- Aside from intermittent access to GPS, the method should use sensors that are reliable and available on production vehicles.
- Slip angle estimates from the nonlinear observer should mathematically be guaranteed to converge even in the presence of estimation error.

Estimators that meet these objectives would undoubtedly provide useful information about the handling capability of a vehicle. A remaining question to address is

how such an estimation method would be integrated into a vehicle control system. Therefore, this thesis's secondary area of focus is the design of a simple envelope controller to keep the vehicle within a safe handling envelope using the information provided by a non-GPS estimation approach.

The envelope controller should meet the following objectives:

- The controller should rely on the estimated handling limit information from the non-GPS based estimator developed earlier in the thesis.
- The controller should utilize front steering as the available control actuator.
- The controller should use front steering actuation as the main mechanism to keep the vehicle within the safe operating envelope, which we define as the maximum available tire grip of the front and rear tires.
- The integrated envelope controller and estimator system should be experimentally validated in simulation and experiment.

The envelope controller presented in this thesis is therefore an investigation of how the idea of envelope protection for aircraft could be extended to a land vehicle with front steering actuation.

1.5 Contributions

This thesis makes several contributions to the estimation and control of lateral tire forces using steering torque. Most of the theoretical results are demonstrated experimentally. This thesis:

1. **Develops four online estimation approaches for characterizing lateral tire forces with GPS.** All of the methods rely on GPS-based slip angle measurements and identify the remaining parameters which characterize lateral forces: tire cornering stiffness, and friction coefficient, and normal force. The first two methods are nonlinear regression approaches. The first uses lateral

force estimates, and the second is based on total aligning moment measurements, and both are validated experimentally. The final two methods rely on linear observer techniques to estimate cornering stiffness and utilize algebraic approaches to determine friction and normal load.

2. **Develops an online, nonlinear observer to characterize the lateral handling limits without reliance on GPS.** Based on steering torque measurements and other sensors available on production vehicles, this approach identifies tire slip angle (and therefore vehicle sideslip angle) and peak lateral force limits. By utilizing the early lateral limit information contained in pneumatic trail, this method is able to predict the limits before the tires have exited the linear handling regime. The slip angle-peak force observer is validated with simulation results and experiment tests on two different road surfaces.

3. **Demonstrates that the nonlinear slip angle-peak force observer is mathematically guaranteed to converge in the presence of estimation error.** Experimental results demonstrate that the slip angle estimates converge to actual values as the stability proof would suggest.

4. **Develops an envelope controller to keep the vehicle within its lateral limits using front steering actuation.** The nonlinear slip angle-peak force observer is combined with the envelope controller to keep the vehicle within its lateral limits. The overall observer/controller structure is demonstrated in simulation and onboard an experimental research vehicle.

1.6 Thesis Outline

The remainder of this thesis is organized as follows:

Chapter 2: Lateral Limit Estimation from Steering Torque provides a broad overview of how torques generated in a vehicle's steering system can be used to provide valuable information about the tire's handling limits. This chapter is organized into three parts. First, it describes the key components that are important

to consider and the simplifying assumptions that can be made when using steering system torques for this estimation problem. The second portion of the chapter provides an overview of the estimation methods developed in the thesis and outline the benefits and drawbacks of each method. Finally, the chapter delves into the details of how to extract the useful contribution of torque from the overall steering torque measurement for estimation purposes. It also presents the models for the forces and moments in the steering system which are used in the estimation methods designed in subsequent chapters.

Chapter 3: Lateral Limit Estimation using GPS investigates methods for characterizing lateral tire forces given the added sensing capability of GPS. Two types of estimation approaches are developed: nonlinear regression methods and algebraic methods. The first nonlinear regression method is based on lateral tire force estimates to identify the tire parameters. Although experimental results show that method is accurate, it suffers from the problem of requiring high levels of lateral dynamics (utilization of 80% of the tire's peak lateral force) before friction estimation can be reliably identified in practice. This motivates the development of the second regression approach which is based on total aligning moment (derived from steering torque measurements) and GPS. Using the early friction information contained in total aligning moment, this second method enables identification of the friction limits as early when the tires have utilized only 50% of the peak lateral force. This is the first known demonstration of utilizing total aligning moment for early friction detection. However, as with all underdeterminate problems, both of the regression techniques require persistent excitation to achieve accurate results. To resolve the need for persistent excitation, two algebraic model-based methods are developed. The first solves for the closed-form solution of the peak friction limit from the total aligning moment measurements, and the second computes the estimate from pneumatic trail information.

Chapter 4: Lateral Limit Estimation Without Reliance on GPS develops a model-based estimation method that utilizes pneumatic trail information in steering torque, rather than GPS, to identify a vehicle's lateral handling limits. The method uses sensors readily available on production vehicles. It is based on simple

models. This chapter demonstrates this method's ability to provide accurate slip angle estimates in simulation and on an experimental research vehicle using a variety of maneuvers on two different road surfaces. Finally, the chapter analyzes the stability properties of the observer in the presence of estimation error and presents a mathematical proof of stability to guarantee convergence.

Chapter 5: Envelope Control using Front Steering introduces a simple envelope control strategy that is inspired by a desirable driver response using steering to control front and rear cornering forces. The chapter develops the control algorithm aimed to keep the tires within their lateral force limits using front steering actuation. The controller is combined with the pneumatic-trail based observer developed in Chapter 4 and demonstrated to stabilize the vehicle motion for a variety of maneuvers in simulation. A comparison is given between steering-actuated envelope control and brake-actuated ESC systems. Finally, the chapter presents experimental results of the overall system implemented onboard a steer-by-wire research vehicle driven on a moderate-friction gravel surface. The results demonstrate that the combined envelope controller and observer system is able to keep tire forces within their limits and keep the vehicle within a safe operating envelope.

Chapter 2

Lateral Limit Estimation from Steering Torque

In Chapter 1, we motivated why knowledge of the vehicle's lateral handling limits is vital for active safety systems and introduced the idea that steering torque has the potential to provide this key information without requiring additional sensors. In this chapter, we give a broad overview of how torques generated in a vehicle's steering system can be used to provide valuable information about the tire's handling limits.

This chapter is organized into three parts. In the first part, we describe the key components that are important to consider and the simplifying assumptions that can be made when using steering system torques for this estimation problem. The second portion of the chapter provides an overview of the estimation methods developed in the thesis and outline the benefits and drawbacks of each method. Finally, in the third section of the chapter, we delve into the details of how to extract the useful contribution of torque from the overall steering torque measurement for estimation purposes. We also present the models for the forces and moments in the steering system which are used in the estimation methods designed in subsequent chapters.

2.1 Estimation Considerations using Steering Torque

As introduced in Section 1.2, lateral force can be characterized by three fundamental parameters: tire slip angle, cornering stiffness and peak lateral force (which is the product of the available tire-road friction and normal force). Our overall goal is to use steering torque measurements and other available sensors to identify these three tire properties. However, in order to do this, let us first develop an understanding for how steering torque is generated.

Maneuvering a vehicle around a turn requires lateral tire forces, while accelerating or braking requires longitudinal tire forces. These forces, which are generated between the tire and the road, are transmitted through the vehicle's steering system. Longitudinal, lateral, and even vertical tire forces all may contribute to the torque in the steering system. Beyond these reactive moments produced by tire forces, the driver steering effort transmitted through the steering column also adds a torque. Furthermore, in many modern steering systems which append the driver's steering effort with an electric motor (such as production EPS or Active Steering systems), the motor provides an additional source of torque in the steering system. We refer to the *total* moment produced about the steering axis, which includes those generated by tire forces, the driver and actuators, as the steering torque. It is from this quantity – steering torque – that we wish to extract the lateral force moment contribution in order to identify the lateral tire force parameters.

In a given estimation problem, it is neither practical nor desirable to take into account every contributing factor given constraints on sensor availability, modeling accuracy and computational complexity. Below, we highlight which factors are important to consider and what simplifying assumptions can be made (and what the consequences of making those assumptions are) when utilizing steering torque for lateral tire characterization:

1. **A good measurement of the torque generated by lateral tire forces in the steering system is required**

   As we demonstrate later this chapter, knowledge of the torque produced by lateral forces in the steering system enables early detection of the tire's handling

limits (even more so than knowing the lateral force itself). This requirement is important; since this torque contribution is the central piece of information used as the basis for estimation, we cannot perform accurate estimation without a good quality signal. This, in turn, motivates the need for proper modeling of the various contributions of torque in the steering system. Since we only wish to use the torque generated by lateral tire forces, we must be able to separate out this quantity out from the overall steering torque measurement. The final sections of this chapter cover the steering system torque and force models which we use to tease out the lateral force contribution of torque in the steering system.

2. **GPS is highly beneficial**

   As described previously in Section 1.3, GPS provides direct measurements of tire slip angle, which simplifies the lateral limit estimation problem considerably. Given GPS-based slip angle measurements, tire cornering stiffness can be determined using linear observer techniques [7, 8]. Then, various methods which use steering torque to estimate the peak lateral force limit (or tire-road friction, if normal force is known) can be applied. These methods are developed in Chapter 3.

   While access to GPS is invaluable, it requires satellite visibility, which may be lost periodically in urban and forested driving environments. Without access to GPS, this becomes a more difficult identification problem. During periods of signal loss, we can make the reasonable assumption that cornering stiffness is constant and turn our focus to estimating tire slip angle and peak lateral force (or friction). Because tire slip angle measurements are no longer available, we must estimate it. We may do this by using the vehicle's equations of motion and measurements from readily available inertial sensors. Combined with steering torque measurements, we can then design methods to estimate peak lateral force (or friction). However, errors in either the slip angle or peak force estimates can cause the estimation scheme to be unstable, so proper observer design is required for convergence. These types of observers are described in Chapter 4, along with a stability proof that demonstrates estimation convergence.

If no GPS sensing is available whatsoever, there exist various methods in publication that attempt to estimate cornering stiffness using inertial vehicle sensors [55, 56]. These methods may be employed, although the reliability and accuracy of their combination with the slip angle and friction limit estimation methods have yet to be determined and are not covered in this thesis.

3. **Knowledge of forces of individual tires is desirable, though if unavailable, we instead estimate axle forces**

   Knowledge of individual tires forces in each direction (lateral, longitudinal and vertical) would offer stability control systems with the most information for maximizing the vehicle's handling capability and maintaining vehicle stability in a given maneuver. However, in practice, we cannot expect that all forces are known for each tire. Thus, the question arises as to which forces are most important to consider for which tires:

   (a) **Lateral forces**

   For lateral forces, at a bare minimum, we must estimate both front and rear *axle* lateral forces. Axle lateral forces govern the vehicle's lateral motion, and knowledge of how close either axle is near the limits of adhesion is crucial for ensuring vehicle stability. Ideally, steering torque measurements would be available for both the front and rear axles. However, in the absence of rear steering sensors (which is the case for front steering EPS, Active Steering and steer-by-wire systems, as well as for our research vehicle P1), we rely on models of the rear axle load dynamics and assumptions of the homogeneity of the available road friction to indirectly determine the rear axle lateral forces.

   If individual tire sensing capability is available, lateral force characterization of each tire is beneficial. Knowledge of individual lateral tire properties enables accurate limit identification on split-μ roads. Furthermore, during a turn, because the inside tire's normal force decreases, it tends to reach the limits of tire adhesion faster. This provides earlier indication of the road friction coefficient when compared to just considering the axle lateral

forces alone. However, considering the left and right tire forces separately requires an understanding of the individual tire's steering geometry and knowledge of the tire normal forces as the vehicle maneuvers. If this information is unavailable or is only approximately known, the lumped axle lateral force properties must instead be considered.

(b) **Longitudinal forces**

Longitudinal forces should be taken into account to enable accurate lateral limit estimation during vehicle braking or acceleration for three primary reasons. First, longitudinal forces produce traction torque about the steer axis, which must be accounted for in the steering torque model. Second, due to the limited friction availability between the tire and the road, longitudinal force generation reduces the amount of lateral force available to the tires. Finally, longitudinal forces also introduce longitudinal dynamics, which can cause weight transfer between the front and the rear axles. This change in the normal load distribution of the tires also affects the amount of friction force available.

While considering the effect of longitudinal forces is certainly important, its inclusion makes solving the lateral estimation problem considerably more complex. Thus, it may be desirable to solve the lateral estimation problem in the absence of longitudinal forces first and include them in later studies. This can be done by focusing on solving the estimation problem when the vehicle is driven at roughly constant speeds or using the steering torque signals from the non-driven (non-braked) wheels. This is the approach taken throughout this thesis, and we leave the inclusion of longitudinal forces into the estimation problem for future work.

(c) **Vertical (normal) forces**

Tire normal force directly influences how much lateral or longitudinal forces can be generated through tire adhesion. If only axle forces are being estimated, we only require knowledge of the axle normal forces. In this

simplified scenario, we may ignore lateral weight shift (which does not affect axle loads) and only must consider the effects of longitudinal weight transfer (if longitudinal dynamics are included in the estimation problem). As mentioned before, if individual tire forces are being estimated, individual normal forces must be either measured or modeled. Although measurements of normal force are preferred, models may be used to approximate the normal load dynamics of the vehicle based on measurable signals such as lateral and longitudinal acceleration, and estimated vehicle states such as roll angle.

To summarize, this estimation problem requires a good measurement of the torque contribution from lateral tire forces, which must be extracted from the overall steering torque measurement. When GPS is available, we can utilize any of the various methods designed in Chapter 3 to determine the lateral force parameters. During periods of signal loss (or when GPS hardware is entirely unavailable, assuming that cornering stiffness can be accurately estimated), the observer described in Chapter 4 may be employed to characterize the lateral forces. Design decisions should be made regarding whether axle or individual tire forces are being estimated. Considering axle forces reduces the complexity of the estimation problem, but ignores some of the valuable information that is available from individual tire sensing.

2.1.1 Identifying Lateral Limits of Adhesion

This section focuses on developing an understanding of how lateral force generated at the tire produces a torque in the steering system, and how that can be used for identifying the lateral tire characteristics. Figure 2.1 illustrates how lateral force is generated from tire deformation, both for a high friction and a low friction surface, assuming a parabolic pressure distribution in the contact patch. The figure depicts the tire traveling towards the right, starting on the left with zero lateral deformation (traveling straight) and ending on the right at the point where the required lateral force exceeds the available friction (skidding out of the page, towards the reader). The angle of tire deformation, or the difference between the tire's heading and velocity, is

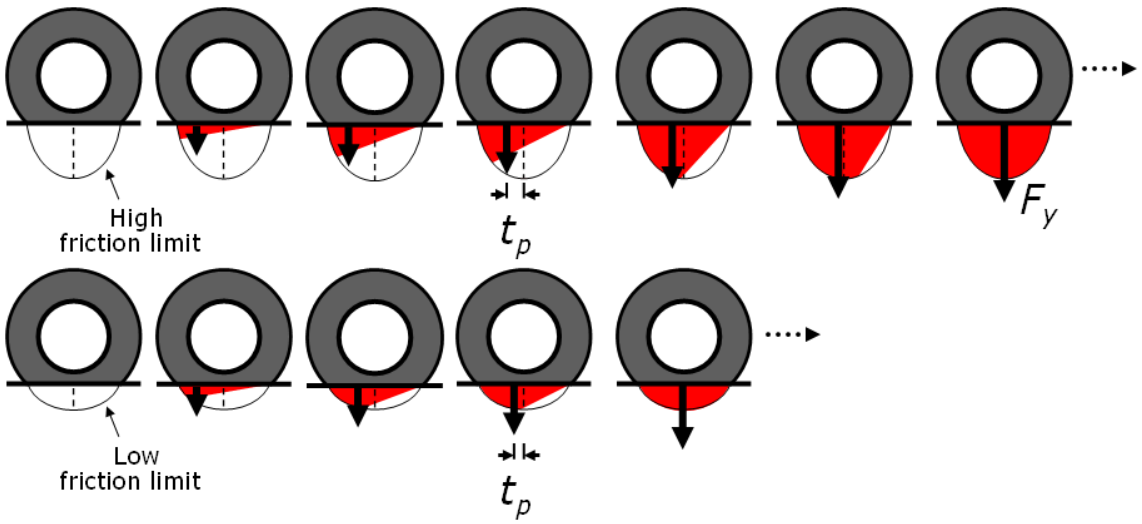

Figure 2.1: Lateral Force F_y Generation as Slip Angle Grows

referred to as slip angle α. As slip angle increases, the lateral force distribution grows in area, which is represented by a shaded triangular area under the tire. However, the lateral force obtained is ultimately limited by the friction limit of the road, which is the product of the tire-road friction coefficient μ and the tire normal force F_z.

Plotting lateral force as a function of slip angle, we arrive at the tire curve presented in Fig. 1.4. Initially, lateral force is unaffected by the friction limits and grows linearly according to the slope determined by cornering stiffness C_α. Ultimately, the force levels off due to the limit of tire adhesion μF_z.

Returning our attention to Fig. 2.1, we observe that the effective lateral force F_y does not act directly at the center of the contact patch. Rather, F_y acts at a distance known as the tire pneumatic trail t_p, which generates a moment about the steer axis (known as self-aligning moment). As slip angle increases, F_y moves toward the center of the patch. This results in t_p vanishing once the force distribution reaches the limit of tire adhesion at a rate which depends on the available peak friction.

In addition to the moment arm provided by pneumatic trail, the steering system geometry also provides an additional lever arm for lateral force. Normally, the steer axis on a vehicle is not vertical, nor is it in line with the point of tire contact with

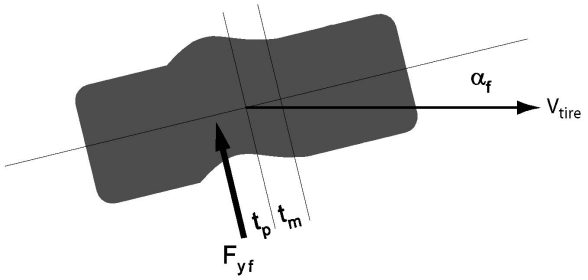

Figure 2.2: Lateral Tire Deformation Generates Lateral Tire Force F_y

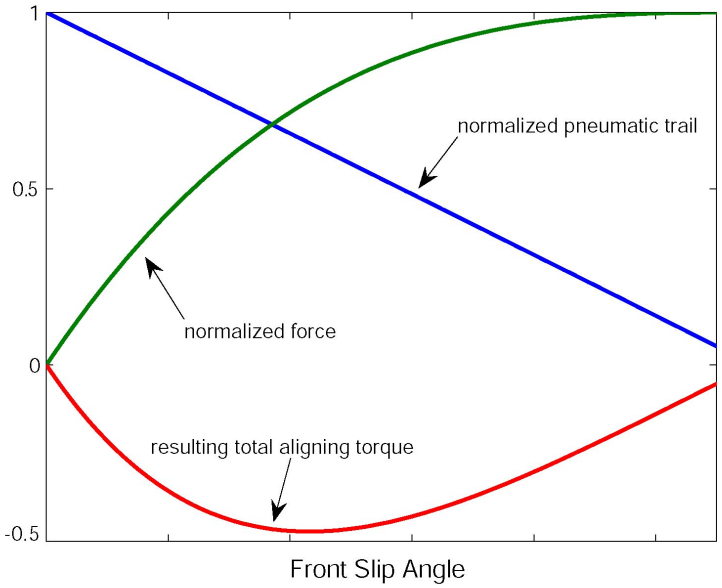

Figure 2.3: Total Aligning Torque Curve (with $t_m = 0$)

the ground (the rationale behind this is explained Section 2.3.1). This provides the lateral force with an additional lever arm called the mechanical (caster) trail, denoted as t_m in Figure 2.2. Whereas pneumatic trail is a function of the tire deformation and road friction, mechanical trail is purely a function of steering geometry and can be determined as a function of steer angle. Thus, the moment produced by lateral force in the steering system, referred to total aligning torque τ_a, is the result of the

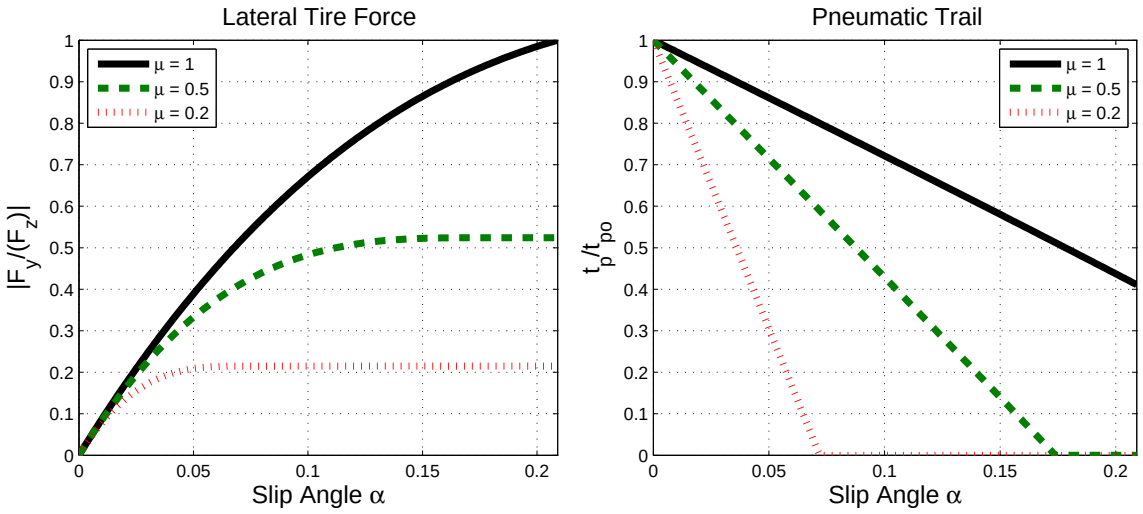

Figure 2.4: Comparison of Lateral Force and Pneumatic Trail

force acting at a distance $(t_p + t_m)$:

$$\tau_a = -(t_m + t_p)F_y. \tag{2.1}$$

Models of lateral force, pneumatic trail, and total aligning torque are normalized and plotted as a function of slip angle in Fig. 2.3 (with $t_m = 0$ for plotting purposes).

2.1.2 Benefits of τ_a and t_p For Estimation

Initially, lateral force is unaffected by the friction limits and grows linearly according to the slope determined by cornering stiffness. Only as the slip angle grows large does the force start to saturate due to limited friction on the road. As demonstrated from Fig. 2.4, which plots lateral force for varying friction coefficients, it is difficult to distinguish between different friction surfaces using lateral force for small slip angles.

While lateral force may not provide sufficient warning of the approaching limits, we may examine other relationships that would serve well for this role. First, we can consider total aligning moment. As seen from Fig. 2.3, as slip angle increases, the total aligning moment increases, then peaks, and finally drops off as the lateral force

generation begins to saturate and the trail continues to decrease. When the total aligning moment begins to drop off, skilled drivers are able to utilize the reduction of steering torque felt through the steering wheel as an indication that the the lateral limits are approaching. This reduction in torque could similarly offer vehicle estimation systems early warning of front tire breakaway [57]. Thus, the characteristic "bowl" shape of total aligning moment may serve as a useful source of early prediction of the friction limits.

Finally, we can consider tire pneumatic trail for estimation. Unlike lateral force or the resulting total aligning moment, pneumatic trail decreases *immediately* as a function of the friction limits μF_z. This decrease occurs even while side force and total aligning moment remain essentially unaffected by the peak force limits. This fact is illustrated in Fig. 2.4, which plots pneumatic trail for varying friction coefficients, and also Fig. 2.1, which shows pneumatic trail's dependency on both slip angle and the friction limits.

This demonstrates why both tire pneumatic trail and total aligning moment are valuable sources of information for early prediction of the handling limits. From this observation, we can now turn our attention to designing estimation methods which utilize total aligning moment (or pneumatic trail, if desired). Using Eq. (2.1), let us rewrite the expression for total aligning moment τ_a explicitly as a function of the tire parameters and steer angle δ:

$$\tau_a = -(t_m(\delta) + t_p(C_\alpha, \mu F_z, \alpha))F_y(C_\alpha, \mu F_z, \alpha)). \tag{2.2}$$

In the above expression, τ_a is a measurement which can be extracted from the steering torque measurements. Mechanical trail t_m can be determined as a function of how the steering geometry changes with steer angle. However, that leaves both pneumatic trail and lateral force as functions of the unknown tire parameters which we wish to estimate. From Eq. (2.2) and a good measurement of total aligning moment, it is possible to design various model-based identification techniques to extract the lateral tire parameters C_α, μF_z and α. The next section provides an introduction to the estimation techniques developed in this thesis.

2.2 Thesis Estimation Approaches

This section is designed to provide the reader with a broad overview of the estimation methods presented in this thesis, explain what assumptions are made, and outline the advantages and disadvantages of each method.

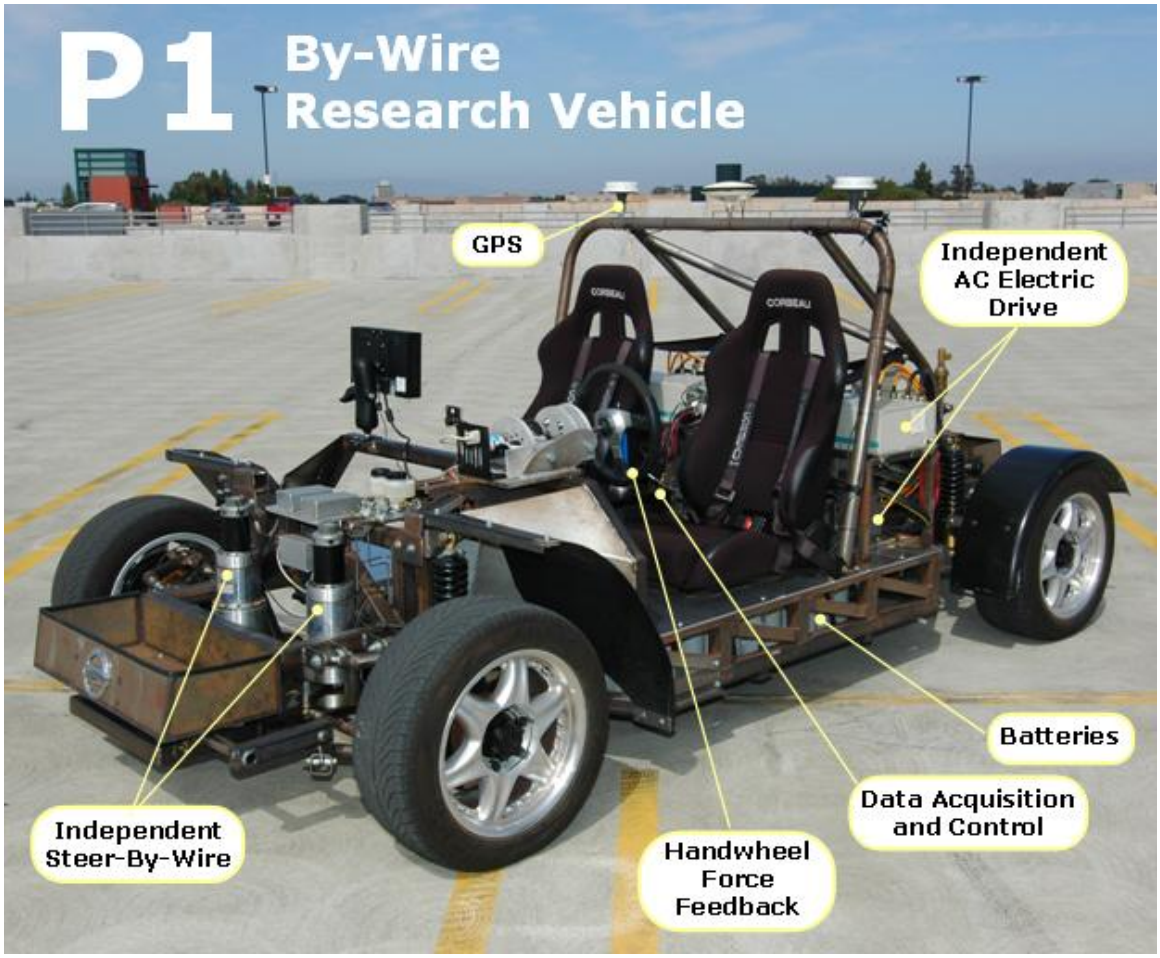

Figure 2.5: Experimental By-wire Research Vehicle P1

The vehicle considered in this work is an experimental steer-by-wire research testbed, P1 (pictured in Fig. 2.5). The vehicle was built in-house at the Dynamic Design Lab and the Product Realization Lab at Stanford University. P1 has independent front steering motors and thus offers front left and right total aligning moment

measurements. P1's sensor suite also includes inertial sensors, steer angle encoders, and GPS.

For all of the estimation algorithms presented in this thesis, longitudinal forces and dynamics are neglected. Additionally, without sensing capability on the rear tires of P1, we focus on characterizing the lateral forces of the front tires only, and make simplifying assumptions to indirectly determine the lateral tire parameters for the rear.

2.2.1 GPS-Based Methods

First, let us consider the case where we have access to GPS measurements, and therefore, have a direct measurement of slip angle. Thus, only two parameters – cornering stiffness C_α and peak lateral force (also referred to as the peak friction limits) μF_z – are left to be estimated.

Force-Slip Regression Method

In the 'Force-Slip Regression Method', we investigate how well we can identify our lateral tire parameters using lateral force information. In order to extract lateral force from total aligning moment measurements using Eq. 2.1, we make two assumptions. First, we assume that for a given surface and a given axle cornering stiffness, we can neglect pneumatic trail's dependence on μF_z and C_α, and create a model for t_p that is only a function of slip angle. The justification here is that we can tune our pneumatic trail model to be representative for a given cornering stiffness and a constant peak friction limit (μ is roughly constant for our testing surface and F_z for the axle is constant due to the lack of longitudinal dynamics). Second, for simplicity, we would like to consider the lumped axle lateral forces only. Because we are considering the axle forces, we make the assumption that there is some effective mechanical trail for the axle which is known and constant.

With this in mind, we can now solve for an estimated lateral force:

$$\widehat{F}_y = -\frac{\tau_a}{t_m + t_p(\alpha)} \tag{2.3}$$

where τ_a, t_m and t_p are all measured or deterministic quantities. Given lateral force estimates, we can gather data points $(\widehat{F}_y, \alpha)$ at each sample time and apply nonlinear regression techniques on the data to estimate μF_z and C_α from a model of lateral force (which are introduced in Section 2.3.3).

The 'Force-Slip Regression Method' is conceptually simple and enables us to see whether the tire properties can be determined for given cornering stiffness and driving surface from lateral force estimates. However, there are clear shortcomings of this method. The most significant drawback of this method is that, by focusing on lateral force to estimate the tire limits of adhesion, the tires must nearly reach the limits before they can be detected. It is only valid for the particular testing surface and cornering stiffness for which the pneumatic trail model was designed. Finally, as an inherently underdeterminate problem, this method also requires persistent lateral excitation to achieve accurate results.

Moment-Slip Regression Method

In the so-called 'Moment-Slip Regression Method', we focus on applying nonlinear regression techniques on directly measurable quantities: total aligning moment and slip angle data pairs (τ_a, α). By dealing with total aligning moment, there is no longer a need to separate out pneumatic trail from lateral force. Now, we can properly account for pneumatic trail's dependence on cornering stiffness and peak friction limits in the model. This extends the validity of this method to a variety of driving surfaces and changing cornering stiffnesses. Most importantly, this method takes advantage of the early friction information encoded in total aligning moment, enabling identification of the friction limits well before tire force saturation.

The 'Moment-Slip Regression Method' can be applied to either the individual front tires or the lumped front axle. Applying it to individual tires makes the estimation scheme more involved; it requires knowledge of mechanical trail (often, mechanical trail vary differently for the left and right tires, see Fig. 2.8) and tire normal force as the vehicle experiences lateral weight transfer.

Two drawbacks remain with this method. It is still an underdeterminate problem in nature and thus requires persistent excitation. Also, given that this method

processes data in batches, we expect a delayed sensitivity to quickly changing road friction properties.

Cubic Moment Method

The basic idea of the 'Cubic Moment Method' is to use a linear observer to estimate cornering stiffness using GPS slip angle measurements, and develop a separate algebraic method for solving for the peak force limits using total aligning moment. Previous literature has established that cornering stiffness can be determined from GPS-based slip angle measurements using various linear observer techniques, such as Luenberger observers or Kalman filters [7, 8]. Thus, all that remains is to estimate μF_z from total aligning moment measurements.

Using a simple representation of total aligning moment (which we develop later in detail in Section 2.3.3), we can model τ_a as a cubic function of the inverse of the peak lateral force, $I_f = \frac{1}{\mu F_z}$:

$$\tau_a = f(I_f, I_f^2, I_f^3). \tag{2.4}$$

Now with only a single unknown in I_f, we can obtain a closed-form solution for the three roots of the above cubic polynomial. This algebraic method does not require persistent excitation, although it is expected to be more sensitive to modeling errors since we are directly solving for I_f rather than applying least squares to minimize the mean-squared error. Another drawback is that logic must be introduced to select which of the three roots corresponds to the physical solution. In the presence of noisy measurements and modeling uncertainty, this task may be not be straightforward.

Linear Pneumatic Trail Method

In the 'Linear Pneumatic Trail Method', we again rely on well-established GPS-based linear observers to estimate cornering stiffness. However, here we focus on estimating μF_z from an estimated pneumatic trail. In our model of pneumatic trail, we approximate t_p to be an affine function of I_f (see Section 2.3.3 for details):

$$t_p = c_1 I_f + c_0 \tag{2.5}$$

Hence, by solving this linear equation, an estimate of t_p provides an estimate of μF_z.

The task, therefore, becomes how we extract t_p from the total aligning moment and slip angle measurements. One way to do this is to solve

$$\widehat{t_p} = -\left(\frac{\tau_a}{\widehat{F_y}} + t_m(\delta)\right) \tag{2.6}$$

where $\widehat{F_y}$ is an estimated lateral force. This equation can be solved using iterative (algebraic loop) techniques, or in a discrete time system, the previous estimate of $\widehat{F_y}$ can be used as a proxy for the current estimate. The advantage of this method is that it removes the need to select among multiple algebraic solutions, as was the case with the 'Cubic Moment Method'. Similarly, it does not suffer from the need of persistent excitation.

A drawback of this method is that it is likely sensitive to modeling errors. Also, we must ensure that obtaining an estimate of pneumatic trail from an estimated lateral force yields a stable, reasonable solution even in the presence of estimation uncertainty.

2.2.2 Methods Without Reliance on GPS

While access to GPS is invaluable, in urban forested environments, satellite visibility is not always available. Cornering stiffness, which changes on a slower time scale as a function of tire wear, pressure and temperature [52], is assumed to be constant during periods of GPS signal loss. However, slip angle changes dynamically with vehicle motion, and peak lateral force can change abruptly with changes in road friction availability and tire normal force. Thus, we would like to devise methods for estimating tire slip angle and peak lateral force (or friction) without reliance on GPS access. In this thesis, we propose two non-GPS based estimation approaches.

Because slip angle measurements are no longer available, we must estimate it. To estimate tire slip angle, we use the vehicle's equations of motion to model how slip angle evolves as a function of the vehicle's lateral tire forces. This slip angle observer updates its estimates based on measurements from readily available inertial sensors,

as well as estimates of the nonlinear front and rear axle forces, $\widehat{F}_{yf}$ and $\widehat{F}_{yr}$. These nonlinear forces are not measured quantities and must be estimated through our tire model based on our best estimates of C_α, μF_z and α (which can be taken as the previous estimate) for the front and rear axles.

Although they use the same approach to estimate slip angle, the two methods proposed in this thesis differ on how they determine μF_z. The lack of GPS slip angle measurements eliminates the possibility of using the regression techniques proposed by the 'Force-Slip Regression' and 'Moment-Slip Regression' methods to identify μF_z. However, the two algebraic approaches used to solve μF_z from total aligning moment in the 'Cubic Moment Method' or pneumatic trail in the 'Linear Pneumatic Trail Method' may still be considered and provide the basis for the non-GPS based estimation approaches described below.

Total Aligning Moment Nonlinear Observer

In 'Total Aligning Moment Nonlinear Observer' method, we apply the same approach that was taken in the 'Cubic Moment Method' to estimate μF_z. That is, from a total aligning moment measurement, we solve the cubic polynomial for I_f (or equivalently μF_z).

This method has similar drawbacks as before: it is likely sensitive to modeling errors and a single solution must be selected from the three cubic roots. However, without a measurement of slip angle, an additional layer of complexity exists when using this method. Errors in either slip angle or peak friction limit estimates can cause the overall observer to become unstable. Thus, any successful application of this method requires first ensuring that the overall system is stable in the presence of estimation errors.

Pneumatic Trail Nonlinear Observer

The final method presented in this thesis is the so-called 'Pneumatic Trail Nonlinear Observer'. Tire slip angle is estimated in an identical fashion using the equations of motion. However, in this method, we solve the affine relationship in Eq. 3.12 between

pneumatic trail and the friction limits to estimate μF_z. By doing so, we remove the need to select among multiple solutions.

The main drawbacks of this method are similar to before. Primarily, we need to show that the observer can converge even in the presence of errors in either slip angle, pneumatic trail or peak force estimates.

All of the estimation methods introduced above are described in further detail in Chapters 3 (for the GPS-based methods) and Chapter 4 (for methods without reliance on GPS). The common thread among all of the estimation algorithms is that they rely on a good measurement of total aligning moment. Motivated by this, we would like to be able to extract total aligning moment information from the overall steering torque in the system. In the final section of this chapter, we take a look at steering system geometry and examine how that influences the torques generated about the steer axis. Then, we develop detailed models for the individual torque and force contributions in a steer-by-wire steering system and construct an observer for extracting total aligning moment.

2.3 Steering System Forces and Moments

2.3.1 Front Steering Geometry

Front steering is achieved by rotation of the wheel about a steer rotation axis, also known as the kingpin axis. Normally, the steer axis is not vertical, nor is it in line with the point of tire contact with the ground (illustrated in Fig. 2.6). The axis is usually tipped outward at the bottom, producing a lateral inclination (kingpin) angle in the range of 0-5° for trucks and 10-15° for passenger cars [20]. The lateral offset distance from the ground intercept to the wheel centerline is called the scrub radius. This offset may be necessary to obtain packaging space for brakes, suspension and steering components. At the same time, it reduces the static steering efforts by allowing the tire to roll around an arc when it is turned.

Caster angle results when the steer rotation axis is inclined in the longitudinal (forward) plane of the tire. Most steering systems utilize a positive caster angle,

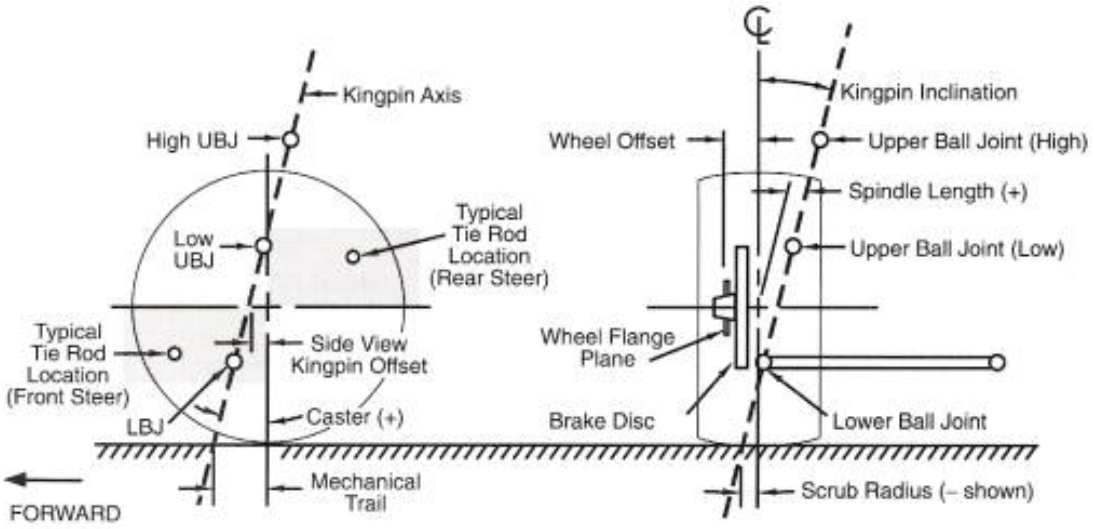

Figure 2.6: Front Steering Geometry [22]

which places the ground intercept of the steer axis ahead of the center of tire contact. Doing so produces a stabilizing restoring moment that attempts to steer the tire out of the turn. Caster angle normally ranges from 0-5° and may vary with suspension deflection and position. The longitudinal offset distance from the ground intercept due to caster angle is referred to as the mechanical (or caster) trail.

2.3.2 P1 Steering System Model

Forces generated at the tire are transmitted through the vehicles steering system and suspension. The steering model developed here is based on the independent front steer-by-wire system of P1. In a steer-by-wire system, the mechanical linkage between the handwheel and road wheels is replaced with an electric motor as shown in Figure 2.7. The model developed here could be extended to systems with a mechanical steering linkage between the front tires. It could also be applied to production EPS and Active Steering systems by including the driver commanded torque contribution, which is an available measurement from the onboard torque sensor on the steering column [2].

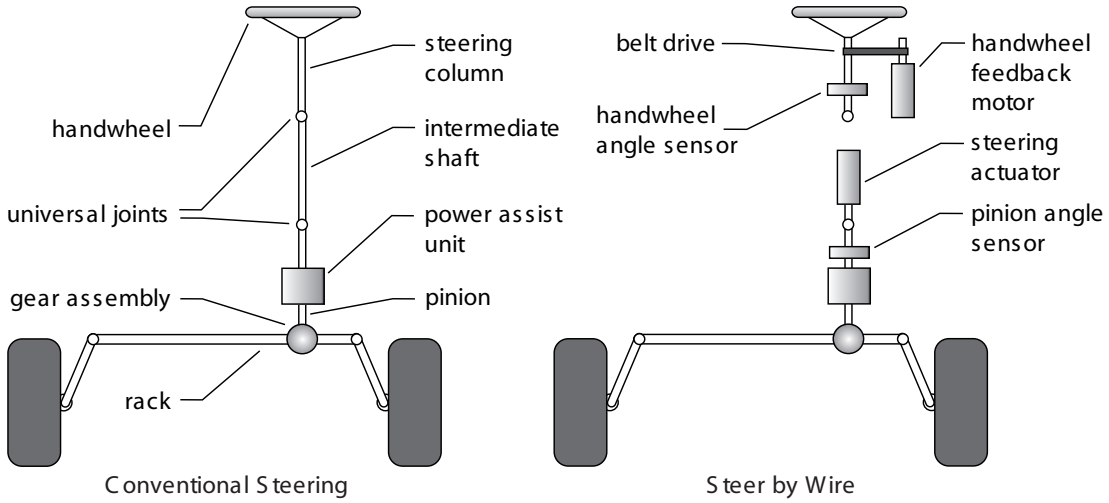

Figure 2.7: Steer-By-Wire Concept [70]

It is our objective is to keep the steering system model as simple as possible while ensuring that it captures the important characteristics of the system. With a steer-by-wire system, the total torque about the steer axis τ is:

$$\tau = \underbrace{\tau_a + \tau_j}_{\tau_d} + \tau_{act}, \tag{2.7}$$

where total aligning moment τ_a is the net torque resulting from lateral tire forces, jacking torque τ_j is the resulting torque from the vertical tire forces, and τ_{act} is the torque generated by the steering motor. We lump the sum of moments generated by the tire forces as τ_d (treated here as a disturbance torque). For simplicity, the torque

generated from longitudinal tire forces acting through the scrub radius is neglected, although the inclusion of longitudinal forces may be considered for future work. Expressions for the total aligning moment τ_a, jacking torque τ_j, and net actuated motor torque τ_{act} are derived below.

2.3.3 Total Aligning Moment τ_a

As described previously, total aligning moment accounts for both the self-aligning torque generated by lateral force acting at a distance called the pneumatic trail and the reaction torque due to the mechanical trail (refer to Eq. 2.1). Since both lateral force and pneumatic trail are functions of the lateral tire parameters, we present models of these below, which are later used in the model-based identification methods developed in Chapters 3 and 4.

Lateral Tire Force Models

The general characteristics of lateral force are that it grows linearly as a function of cornering stiffness for small slip angles and it ultimately levels off due to the limits of tire adhesion, as first introduced in Fig. 1.4. The nonlinear and dynamic properties of tire-road friction are difficult to analytically describe, while most empirical formulas are hard to explain by physical laws. Practical applications require a manageable tire model, in which measurement data could be translated sensibly into tire properties and vice versa [32].

There exist numerous models for lateral tire force, varying from a proportional linear model that only depends on cornering stiffness and slip angle (which is only valid away from the friction limits), to the so-called Magic Formula model which is characterized by multiple empirical parameters [43]. For tire property estimation, there is often a temptation to use complex models to describe the subtleties of the lateral tire curve. But in practice, the exact shape and nuances of the curve are generally unknown. For example, on dry asphalt, there is distinct peak to the tire curve, after which the force decreases slightly (as illustrated in Fig. 1.4) [2]. n dry gravel, experimental results demonstrate that the curve does not reach a distinct peak

and simply levels off [25].

In this thesis, we have chosen two lateral tire models that share a common theme: a nonlinear representation of a lateral tire force with minimal complexity and a qualitative correspondence with experimental tire behavior. We offer two tire models to the reader to demonstrate that the estimation algorithms developed in this thesis are not predicated on a specific tire model. Both formulas are functions of four fundamental physical tire properties: slip angle, cornering stiffness, normal force, and a single tire-road friction coefficient (which we use to represent the ratio between the maximum lateral force to the normal force).

The first model used is the simplified version of the HSRI model [14]:

$$F_y = -C_\alpha \tan\alpha \cdot f(\lambda), \tag{2.8}$$

where

$$\begin{aligned} f(\lambda) &= \begin{cases} (2-\lambda)\lambda & \text{if} \quad \lambda < 1 \\ 1 & \text{else} \end{cases} \\ \lambda &= \frac{1}{2C_\alpha I_f \mid \tan\alpha \mid}. \\ I_f &= \frac{1}{\mu F_z} \end{aligned}$$

where α is the slip angle of a given tire and I_f is referred to as the inverted peak lateral force, which is the inverse of the maximum possible lateral force achievable between the tire and the road, μF_z. This model assumes no longitudinal forces, a *uniform* pressure distribution in the contact patch, a rigid tire carcass, and a constant coefficient of friction of sliding rubber.

The second model used is the brush tire Fiala model [43]. This model assumes no longitudinal forces, a *parabolic* pressure distribution, a rigid tire carcass, and a constant coefficient of friction of sliding rubber:

$$F_y = \begin{cases} -C_\alpha \tan\alpha + \frac{C_\alpha^2}{3}|\tan\alpha|\tan\alpha I_f - \frac{C_\alpha^3}{27}\tan^3\alpha I_f^2 & \text{if} \quad |\alpha| \le \alpha_{sl} \\ -\frac{1}{I_f}\text{sgn}\alpha & \text{else} \end{cases} \tag{2.9}$$

where

$$\alpha_{sl} \;=\; \tan^{-1}\left(\frac{3}{C_\alpha I_f}\right)$$

In the above formulation, α_{sl} is the slip angle at which the tire has lost lateral adhesion. Also, with an estimate of cornering stiffness [7], I_f is the sole parameter to be estimated in this model. Estimation errors resulting from errors in the tire model can be bounded as discussed in Section 4.4.

Both tire models assume that the sliding and adhesion coefficients of friction are equal, and therefore predict that lateral force plateaus at μF_z (as shown in Fig. 2.3), rather than reaching a distinct peak after which the force decreases. Although they are similar at first glance, the Fiala model differs from the HSRI model by one aspect. With its assumption of a parabolic pressure distribution (as one would physically expect given the vertical deformation of a tire on a flat surface without longitudinal forces), the Fiala model provides a more realistic physical representation of tire forces.

Coupled Lateral/Longitudinal Tire Model

If we would like to account for how lateral tire force generation is affected by the presence of longitudinal tire force (from drive or brake forces), we must consider the coupled relationship between the longitudinal and lateral tire forces. This is due to the fact that there is a limited amount of tire force that can be generated in the contact patch. The tire adhesion capability used for generating longitudinal tire force therefore limits how much lateral tire force can be generated in the contact patch, and vice versa. This coupled relationship is often called the "Friction Circle" or the "Friction Ellipse" concept.

In the following formulation of the coupled longitudinal and lateral brushed tire model, we assume a parabolic pressure distribution, a rigid tire carcass, and a constant coefficient of friction of sliding rubber μ. The derivation of this tire model follows the derivation presented in [43]. The coupled tire model for longitudinal force F_x and

lateral force F_y is as follows:

$$F_x = \frac{C_x\left(\frac{\kappa}{1+\kappa}\right)}{f}F \tag{2.10}$$

$$F_y = -\frac{C_\alpha\left(\frac{\tan\alpha}{1+\kappa}\right)}{f}F \tag{2.11}$$

where

$$F = \begin{cases} f - \frac{1}{3\mu F_z}f^2 + \frac{1}{27\mu^2 F_z^2}f^3 & \text{if} \quad f \leq 3\mu F_z \\ \mu F_z & \text{else} \end{cases}$$

$$f = \sqrt{C_x^2\left(\frac{\kappa}{1+\kappa}\right)^2 + C_\alpha^2\left(\frac{\tan\alpha}{1+\kappa}\right)^2}$$

$$\kappa = \frac{R_e\omega - V_{xt}}{V_{xt}}$$

In the above equations, C_x is the tire longitudinal stiffness and κ is the longitudinal slip ratio (which depends on the effective tire radius R_e, the wheel speed ω and the longitudinal tire speed V_{xt}). As expected, this tire model collapses to the Fiala tire model of pure side slip if we neglect longitudinal slip by setting $\kappa = 0$.

Mechanical Trail

Mechanical trail is a function of steering geometry, which can be determined through kinematics [31]. Figure 2.8 illustrates the mechanical trails of the left and right tires as a function of steer angle on P1.

Pneumatic Trail Models

Tire pneumatic trail is a function of the lateral force distribution in the contact patch and, as discussed in Section 2.1.2, is an extremely valuable source of information for estimation of the tire's lateral limits. For a front steering system, pneumatic trail depends on slip angle α, tire cornering stiffness, and peak achievable lateral force. Qualitatively, at zero slip angle, t_p starts at an initial length t_{po} and vanishes to zero

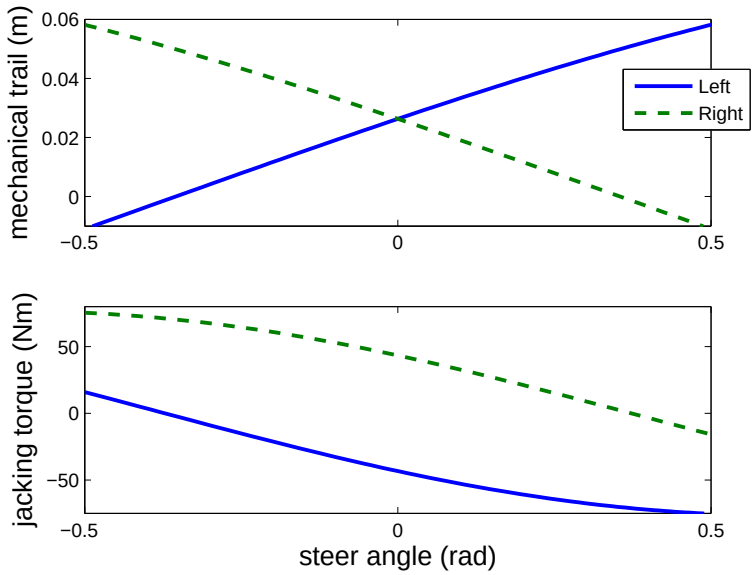

Figure 2.8: Mechanical Trail and Jacking Torque Characteristics on P1

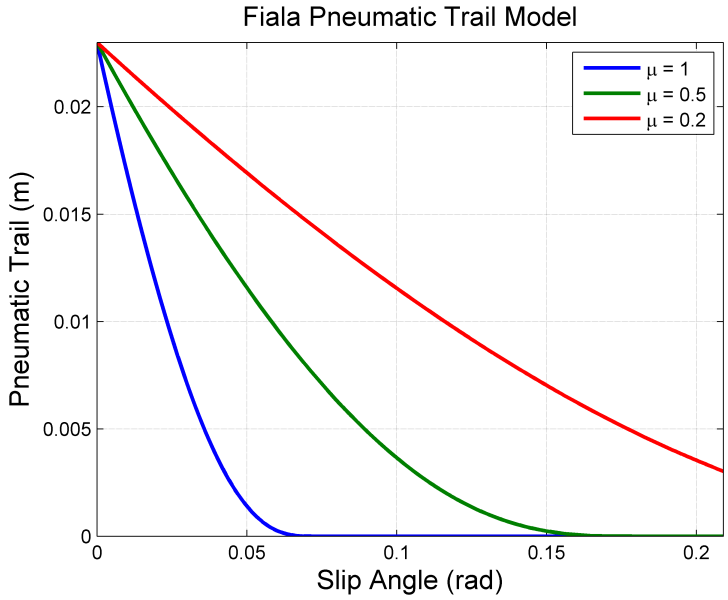

Figure 2.9: Fiala Pneumatic Trail Model for Various Friction Coefficients

once the tire has lost lateral traction.

There are various models for how pneumatic trail depends on slip angle and other tire parameters. We present two models in this work. The first is the pneumatic trail as predicted by a parabolic pressure distribution and a single coefficient of friction, which is the companion of the tire model developed in [43]:

$$t_p = \begin{cases} t_{po}\frac{1-3|\theta_y\sigma_y|+3(\theta_y\sigma_y)^2-|\theta_y\sigma_y|^3}{1-|\theta_y\sigma_y|+\frac{1}{3}(\theta_y\sigma_y)^2} & \text{if} \quad |\alpha| \leq \alpha_{sl} \\ 0 & \text{else} \end{cases} \tag{2.12}$$

where

$$\begin{aligned} \sigma_y &= \tan\alpha \\ \theta_y &= \frac{C_\alpha I_f}{3} \end{aligned}$$

and t_{po} is the initial pneumatic trail. t_{po} is derived to be $\frac{1}{6}l$ where l is the length of the tire contact patch by finding the centroid of the approximate triangular lateral force distribution in Fig. 2.1. Figure 2.9 plots the brushed tire pneumatic trail model for various friction coefficients. Although this pneumatic trail is derived analytically for a parabolic pressure distribution, it is less accurate in practice than the accompanying force model [43].

As with the force model, we choose a simple representation and bound the resulting error in Section 4.4. The model used here is an affine formula that begins at an initial trail length t_{po} and vanishes when the tires have lost lateral adhesion:

$$t_p = \begin{cases} t_{po} - \frac{t_{po}C_\alpha}{3} I_f |\tan\alpha| & \text{if} \quad |\alpha| \leq \alpha_{sl} \\ \\ 0 & \text{else} \end{cases} \tag{2.13}$$

This affine t_p model is plotted for various friction coefficients (normalized by t_{po}) in Fig. 2.4. This is the primary pneumatic trail model used for the remainder of this work.

Combining the Fiala lateral tire force model, mechanical trail and linear pneumatic

trail model in Eq. (2.13) yields the following total aligning moment model before the tires are fully sliding:

$$\begin{aligned}\tau_a &= -\left(t_m + t_{po} - \frac{t_{po}C_\alpha}{3} \mid \tan\alpha \mid I_f\right) \cdot \\ &\quad \left(-C_\alpha \tan\alpha + \frac{C_\alpha^2}{3} \mid \tan\alpha \mid \tan\alpha I_f - \frac{C_\alpha^3}{27}\tan^3\alpha I_f^2\right). \end{aligned} \tag{2.14}$$

After full sliding, total aligning moment reduces to:

$$\tau_a = \frac{t_m}{I_f}\text{sgn}\alpha. \tag{2.15}$$

Although the equations are omitted here, a similar total aligning torque model could be obtained by using the HSRI lateral force model rather than the Fiala model (or for further completeness, the coupled longitudinal/lateral tire model could be used).

2.3.4 Jacking Torque τ_j

While lateral tire force generates total aligning moment, jacking torque is the reaction torque produced from the vertical tire force and suspension travel as a function of steer angle δ. With the goal of lateral tire characterization in mind, total aligning moment provides a useful source of information, while jacking torque represents a disturbance in the steering system.

Jacking torque is a function of suspension geometry and can be modeled as:

$$\tau_j(\delta) = F_z\frac{dh}{d\delta}(\delta), \tag{2.16}$$

where h is the change in suspension height due to steering, which is known from kinematics. Figure 2.8 shows the jacking torque characteristics at nominal vertical load on P1 [31].

The amount of jacking torque depends on the vertical load F_z on the tire. During a maneuver, F_z varies (often significantly) from lateral weight transfer due to vehicle roll and lateral acceleration. The following section explains how load transfer is

Figure 2.10: Lateral Weight Transfer

included in the calculation of jacking torque.

Lateral Load Transfer

As the vehicle begins to roll and lateral acceleration increases, the outside wheel experiences a significant increase in normal load while the inside wheel's load decreases (illustrated in Fig. 2.10). In order to account for the effects of lateral load transfer on the front tires, we use the following steady-state weight transfer model. Summing the moments about the front roll center yields a change in load at the front tires ΔF_z:

$$\Delta F_z = \frac{1}{t_f}\left(K_{\phi f}\phi + h_f a_y \frac{2F_{znom}}{g}\right), \tag{2.17}$$

where t_f is the front vehicle track width, $K_{\phi f}$ is the front roll stiffness, ϕ is the roll angle, h_f is the height of the front roll center, g is the acceleration due to gravity, and a_y is the lateral acceleration. Equation 2.17 assumes that the left and right tires begin with the same nominal load F_{znom}.

From Eq. (2.17), the loads on the front left and right tires, F_{zl} and F_{zr}, are

$$F_{zl} = F_{znom} - \Delta F_z \tag{2.18}$$

$$F_{zr} = F_{znom} + \Delta F_z. \tag{2.19}$$

The following section develops steer-by-wire actuated motor torque, the remaining piece in the overall system model for a steer-by-wire system.

2.3.5 Actuated Motor Torque τ_{act}

The motor torque τ_{act} includes the commanded motor current i, gearbox ratio n_g, motor constant k_m, Coulomb friction in the motor assembly f_m and steering system f_w which are nonlinear functions of the steer angle direction, gearbox efficiency η, and linkage ratio of the steering system n_l [31]:

$$\tau_{act} = (n_g k_m i - f_m(\dot{\delta}))\eta n_l - f_w(\dot{\delta}). \tag{2.20}$$

A complete steering model for a given tire includes the effective damping b_{eff} and inertia J_{eff}, yielding

$$J_{eff}\ddot{\delta} + b_{eff}\dot{\delta} = \tau_a + \tau_j + \tau_{act}. \tag{2.21}$$

2.4 Total Aligning Moment Identification from Steering Torque

Because total aligning torque is useful for lateral tire characterization, this section develops a method to extract it from steering torque measurements in the steer-by-wire system. The other contributions of torque are treated as disturbances.

2.4.1 τ_a Disturbance Observer

In order to estimate the total aligning torque from the steering system model developed previously, a linear disturbance observer structure is formed from the steering dynamics. The estimated aligning torque is then used as a measurement for the lateral limit estimation methods in the chapters that follow. The formation of the disturbance observer follows the design presented by Yih *et al* [71].

To construct the linear disturbance observer, the nonlinear Coulomb friction terms in Eq. (2.20) are included in the observer's input channel. The effective input current

into the steering system is:

$$i_{eff} = i - \frac{f_m(\dot{\delta})}{n_g k_m} - \frac{f_w(\dot{\delta})}{n_g k_m \eta n_l} \tag{2.22}$$

By combining terms, the resulting steering system model is

$$J_{eff}\ddot{\delta} + b_{eff}\dot{\delta} = n_g k_m \eta n_l i_{eff} + \tau_d. \tag{2.23}$$

Rewriting Eq. (2.23) in state-space form, with $x = \left[\delta, \dot{\delta}, \tau_d\right]^T$, the steering system dynamics are given by:

$$\begin{aligned} \dot{x} &= A_{cts}x + B_{cts}i_{eff} \\ A_{cts} &= \begin{bmatrix} 0 & 1 & 0 \\ 0 & -\frac{b_{eff}}{J_{eff}} & \frac{1}{J_{eff}} \\ 0 & 0 & 0 \end{bmatrix} \\ B_{cts} &= \begin{bmatrix} 0 \\ \frac{n_g k_m \eta n_l}{J_{eff}} \\ 0 \end{bmatrix} \end{aligned} \tag{2.24}$$

and the measured output y_m is

$$\begin{aligned} y_m &= C_{cts}x \\ C_{cts} &= \begin{bmatrix} 1 & 0 & 0 \end{bmatrix}. \end{aligned} \tag{2.25}$$

Using the forward-Euler approximation with a sampling time of t_s, the state-space equations are discretized as:

$$\begin{aligned} A &= I + t_s A_{cts} \\ B &= t_s B_{cts} \\ C &= C_{cts}. \end{aligned}$$

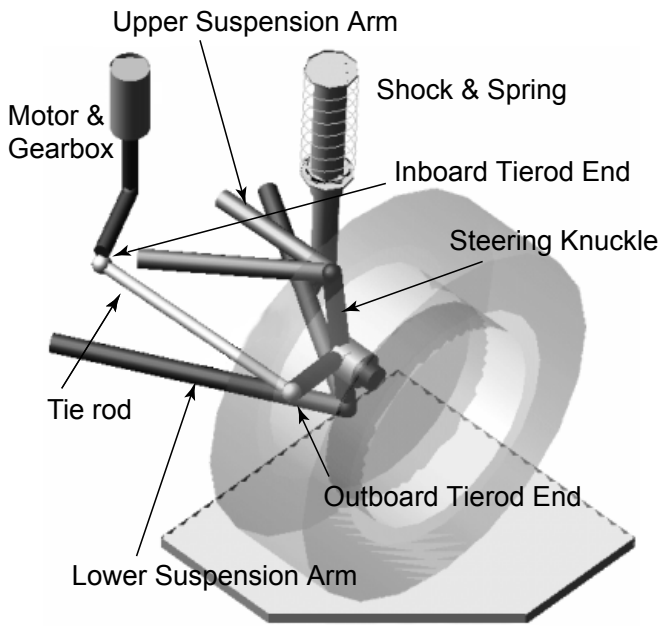

Figure 2.11: P1 Suspension and Steering Systems

Given these state dynamics, it is straightforward to construct a discrete Luenberger observer by calculating the necessary observer gains L to ensure that the error state $e = \widehat{x} - x$ dynamics:

$$e(k+1) = (A - LC)e(k) \tag{2.26}$$

converge to zero, where $\widehat{x}$ is the estimated state vector.

Using Eq. (2.7), the total aligning torque of a given tire is determined by subtracting jacking torque from the resulting τ_d estimates. In summary, the disturbance observer structure takes left and right motor currents as the input, and left and right steer angle measurements from the onboard encoders as the measured output. It returns estimates of the total aligning torque of each front tire.

2.4.2 Disturbance Observer Validation

In order to validate the disturbance observer's total aligning moment estimates, they are compared to the total aligning moment calculated from onboard load-cell sensors.

Mounted on the left and right tierods (pictured in Fig. 2.11) of the research vehicle are load-cells that provide measurements of the force transmitted to each tierod. Using the suspension geometry and the mechanical system simulation software ADAMS, the effective moment arm between the steering motor and the tierod, r_{lc}, is determined as a function of steer angle. Load-cell force measurements F_{lc} can then be used to find the load-cell torque at the tierod τ_{lc}:

$$\tau_{lc} = r_{lc}(\delta)F_{lc}, \tag{2.27}$$

which then can be translated to the total aligning moment $\tau_{a,lc}$ of the tire:

$$\tau_{a,lc} = -\left(\tau_j(\delta) + r_{lc}(\delta)F_{lc}n_l - f_w(\dot{\delta})\right) + J_w\ddot{\delta} + b_w\dot{\delta}, \tag{2.28}$$

where J_w and b_w are the inertia and damping of the wheel and steering knuckle, respectively. The total aligning moment measurements for each tire are summed together to form the front axle total aligning torque $\tau_{af,lc}$. This load-cell based torque measurement is considered truth, against which the disturbance observer is compared.

An experimental maneuver is presented on the research vehicle P1 (pictured in Fig. 2.5) to demonstrate the performance of the disturbance observer. Data were collected on flat pavement at a constant, moderate speed of 10 m/s, or 22 mph. Figure 2.12 displays the resulting front slip angle and lateral acceleration from a right-hand ramp steer maneuver from 0 to -20 degrees at the roadwheels. Figure 2.13 presents the normal loads of the front left and right tires resulting from the lateral weight transfer model developed in Eqs. (2.17)-(2.19).

Figure 2.14 illustrates the comparison between the disturbance observer and load-cell-based front axle aligning moments (the sum of the left and right contributions). Note that at $t = 6.5\,\mathrm{s}$, the vehicle travels over a sizeable grate on the airfield. This extreme event results in a noticeable torque disturbance seen in both measurements. The brief discrepancy between the estimated torques and $\tau_{af,lc}$ at $t = 8\,\mathrm{s}$ is likely due to stiction present in the suspension. This stiction enables a momentary decrease in the required motor torque output to complete the turn. Overall, however, the observer estimates match well with the load-cell based measurements. This completes

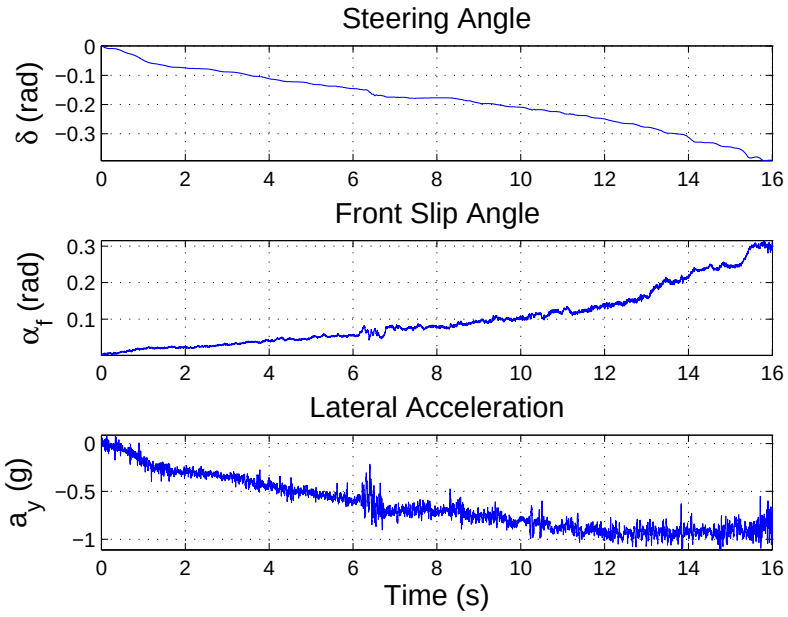

Figure 2.12: Ramp Steer Maneuver on Pavement

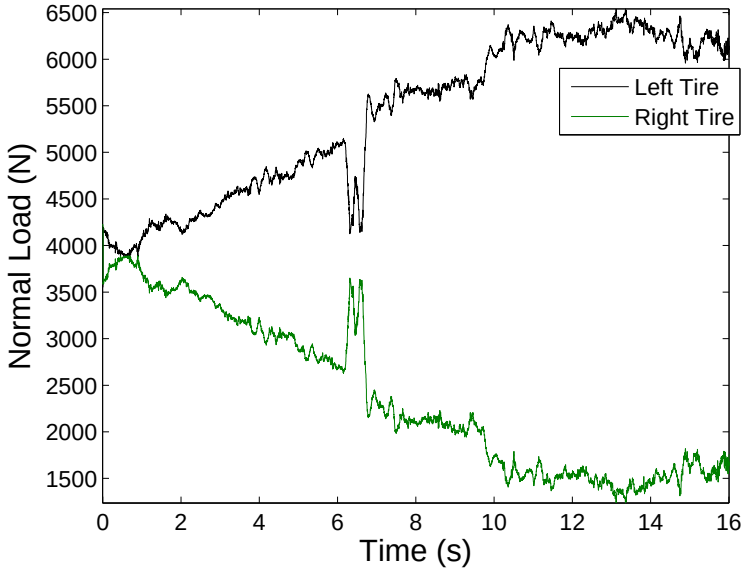

Figure 2.13: Ramp: Front Left/Right Tire Normal Forces

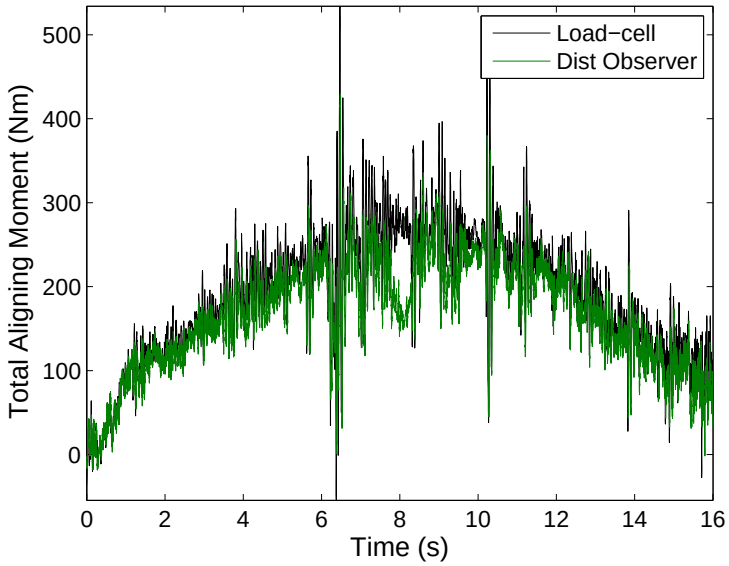

Figure 2.14: Total Aligning Torque Validation

the validation of the approach of estimating total aligning moment with a disturbance observer structure.

2.4.3 Validity of τ_a Model on Banked/Graded Roads

All of the models developed thus far assume that the vehicle is driven on a flat road. For most driving situations, this assumption is quite adequate. However, in the presence of significant road bank or grade, the steering system model must be altered. For example, a more inclusive weight transfer model should be used to account for the affects of gravity on tire normal force and lateral acceleration. The resulting changes in normal load would then affect the jacking torque and total aligning moment generated about the left and right steer axes. Practical implementation of the model would also be more involved as knowledge of road bank and grade angle would be required.

Preliminary experimental studies were performed comparing the accuracy of the total aligning moment model proposed in Eqs. (2.14)-(2.15) with measurement during

test conditions that include flat and banked roads, road grade, and transient maneuvers. The experimental results demonstrate that the models perform well on flat and banked roads and during transient maneuvers, but a more sophisticated load transfer model that incorporates suspension deflection and longitudinal weight transfer is required to capture the effect of road grade. Please refer to Appendix A for details.

2.5 Conclusions

Total aligning moment, the moment generated about the steer axis from lateral forces, is advantageous for several reasons. First, because of its dependence on pneumatic trail, it provides early warning of approaching lateral limits. Second, it can be extracted from steering torque measurements available on production vehicles with EPS or Active Steering, or as shown in this chapter, on research vehicles with steer-by-wire.

This chapter outlined some of the estimation considerations when using steering torque information for determining the lateral limits of tire adhesion. Using total aligning torque measurements from the steering system, the estimation methods developed in this thesis were introduced. This chapter also developed a steering system model and linear disturbance observer in order to extract total aligning moment from steering torque measurements. In the subsequent chapters, we will derive the estimation algorithms in detail and apply them to experimental data for validation.

Chapter 3

Lateral Limit Estimation Using GPS

3.1 Introduction

In the previous chapter, we motivated how useful the total aligning moment information contained in the steering system can be for lateral force characterization. We also developed a linear disturbance observer that enabled us to extract total aligning torque from steering torque measurements.

In this chapter, we investigate methods for estimating the lateral force parameters (tire slip angle, cornering stiffness and peak lateral force) using steering torque measurements from a steer-by-wire system and the added sensor capability of GPS. GPS is a network of 29 satellites in orbit around the earth, each sending out a coded message [37]. Using triangulation, the position and velocity of the GPS receiver can be determined, or with a pair of receivers the heading of the receivers can be determined. When combined with inertial sensors from an INS system, GPS can provide direct, continual measurements of vehicle sideslip angle, which through kinematics can be translated to the slip angles at each tire [7, 49]. Thus, with GPS access, only two parameters – cornering stiffness and peak lateral force – remain to be identified.

Four GPS-based estimation approaches are developed in this chapter. The first is

the so-called 'Force-Slip Regression Method', which makes several assumptions in order to develop a very simple way to identify the tire parameters based on lateral force information. It considers the lumped axle lateral forces only and models mechanical trail as a known constant. Additionally, in order to extract lateral force estimates from total aligning moment, we utilize a simplistic model of pneumatic trail that is representative of a narrow range of road and tire properties. The main drawback of this method is that it relies on lateral force for tire property estimation. Experimental results demonstrate that this method is only able to identify the tire-road coefficient friction when the tires have utilized 80% of their peak force.

The second estimation approach is the 'Moment-Slip Regression Method', where we focus on applying nonlinear regression techniques on directly measurable quantities: total aligning moment and slip angle data. By dealing with total aligning moment, there is no longer a need to separate out pneumatic trail from lateral force. This method properly accounts for pneumatic trail's dependence on cornering stiffness and peak friction limits and extends the its applicability to a variety of driving surfaces and changing cornering stiffnesses. Most importantly, this method takes advantage of the early friction information encoded in total aligning moment. Experimental work demonstrates this method is able to identify the friction limits at only 50% of the peak force utilization. However, as an inherent underdeterminate problem, persistent excitation is required for accurate results.

The final two estimation approaches introduced in this chapter offer optional refinements to how the peak friction limits are estimated. By solving for the friction limits algebraically, these methods address the drawback of requiring persistent excitation. In the so-called 'Cubic Moment Method', we solve the cubic polynomial model of total aligning moment to obtain a closed-form solution of the peak friction limits, although logic must be introduced to select which of the three roots corresponds to the physical solution. The final method presented is the so-called 'Linear Pneumatic Trail Method', in which peak lateral force is algebraically determined from an estimate of pneumatic trail, rather than total aligning moment.

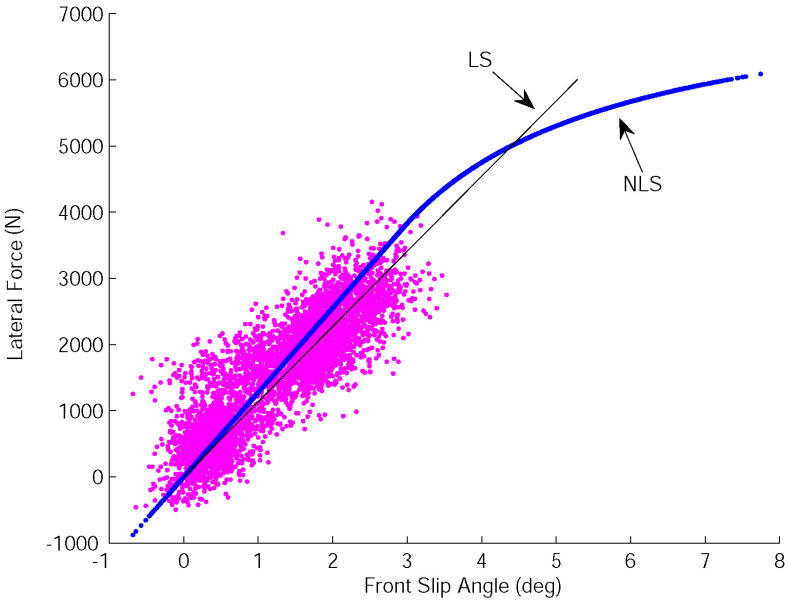

Figure 3.1: LS and NLLS Data Fits

3.2 Force-Slip Regression Method

Cornering stiffness can easily be identified in the linear region of handling using GPS-based slip angle measurements [7]. However, in the presence of noisy measurements and tire property variations, the main challenge of identifying μ is that it cannot be estimated from lateral force measurements until the limits are approached. This is because for small slip angles, as illustrated in Fig. 2.4, lateral force is unaffected by the friction limits. Only when the tire forces near saturation can we confidently identify the friction limits. The following method addresses this issue by quantifying when the tire forces have entered the nonlinear handling region before μ estimation begins.

This estimation algorithm returns two estimates, $\widehat{C}_{\alpha f}$ and $\widehat{\mu}$. For $\widehat{C}_{\alpha f}$, nonlinear least squares (NLLS) is used. NLLS is an iterative technique that best fits data to a nonlinear model. In this case, groups of (F_{yf}, α_f) data are fitted to the Dugoff model in Eq. (2.8) to provide a continual estimate of $\widehat{C}_{\alpha f}$ given the current estimate of $\widehat{\mu}$

(the Fiala tire model in Eq. (2.9) could also be used).

For $\widehat{\mu}$, the estimation technique is slightly more involved. First, the algorithm must determine whether the tire has entered the saturation region. If the force-slip data suggest that the tire is operating in the linear regime, there is not sufficient information to estimate the friction coefficient and $\widehat{\mu}$ is held at its previous value. Otherwise, if the tire force has begun to saturate, the algorithm applies NLLS to a nonlinear tire model and returns an estimate for $\widehat{\mu}$.

In order to quantify the degree of nonlinearity in the force-slip data, a combination of least squares (LS) and NLLS is utilized. In contrast to NLLS, the method of LS provides a best fit straight line through the origin of the force-slip data. Figure 3.1 illustrates an example of both fits to a batch of force-slip data. The algorithm calculates the amount of error between the data and the LS and NLLS fits. If the lateral force is approximately a linear function of slip angle, the LS fit error will be similar to that of NLLS. However, if there is a significant degree of nonlinearity in the acquired data, the LS fit error will be large compared to that of NLLS. Thus, by comparing how well each method fits the force-slip data, the algorithm can quantify whether the tire has entered the saturation regime and return an estimate for $\widehat{\mu}$.

3.2.1 Real-time Estimation Algorithm

The complete real-time estimation algorithm is outlined below:

1. *Find* α_f: A combination of GPS and INS sensors can accurately estimate sideslip angle β, yaw rate r, and longitudinal speed V_x which are used to calculate the front slip angle α_f using the kinematic relationship below [7]:

$$\alpha_f = \beta + \frac{ar}{V_x} - \delta. \tag{3.1}$$

   a is the distance from CG to front axle.

2. *Find* F_{yf}: Determine t_m from steering geometry and assume it to be approximately constant. If we neglect pneumatic trail's dependence on tire parameters and assume that it is only a function of tire slip angle, we can

calculate t_p using a very simple linear model:

$$t_p = 0.3l\left(-\frac{2}{\pi}\alpha_f + 1\right), \tag{3.2}$$

where l is the static tire contact patch length [13]. Note that this simplification is only representative for a high friction surface and certain range of cornering stiffnesses, and is not made in subsequently developed methods. Using the disturbance observer developed in Section 2.4, total aligning moment can be identified from the steer-by-wire system. Given t_p, t_m and τ_a, F_{yf} can be estimated from the relationship in Eq. (2.1).

3. *Estimate $C_{\alpha f}$ and μ*: Iteratively perform NLLS to the Dugoff model on the batch of force-slip data, starting the estimates at $\widehat{C}_{\alpha f} = C_{\alpha f_o}$ and $\widehat{\mu} = \mu_o$. Once an approximate solution $(C_{\alpha f-nls}, \mu_{f-nls})$ is reached, return $\widehat{C}_{\alpha f} = C_{\alpha f-nls}$. To ensure that there is enough data for the NLLS fit to be meaningful, first initialize the process by placing a slip angle threshold α_{thres}. The slip angle data must exceed α_{thres} before parameter estimation begins.

   The next step is to determine whether the tire force has saturated sufficiently to estimate $\widehat{\mu}$. In parallel to NLLS fit, apply the method of LS to the data points to find the slope of the line through the origin:

$$m = (\alpha_f^T \alpha_f)^{-1} \alpha_f^T F_{yf}. \tag{3.3}$$

   Calculate the incremental mean squared error (MSE) of both fits from the most recent vector of data points $(\widetilde{F}_{yf}, \widetilde{\alpha}_f)$ of length N:

$$e_{nls} = \frac{\|\widetilde{F}_{yf} - F_{nls}\|^2}{N} \tag{3.4}$$

$$e_{ls} = \frac{\|\widetilde{F}_{yf} - m\widetilde{\alpha}_f\|^2}{N} \tag{3.5}$$

   where F_{nls} is calculated from the HSRI Model in Eq. (2.8) using $(C_{\alpha f-nls}, \mu_{f-nls})$. If the force-slip data is sufficiently nonlinear, i.e

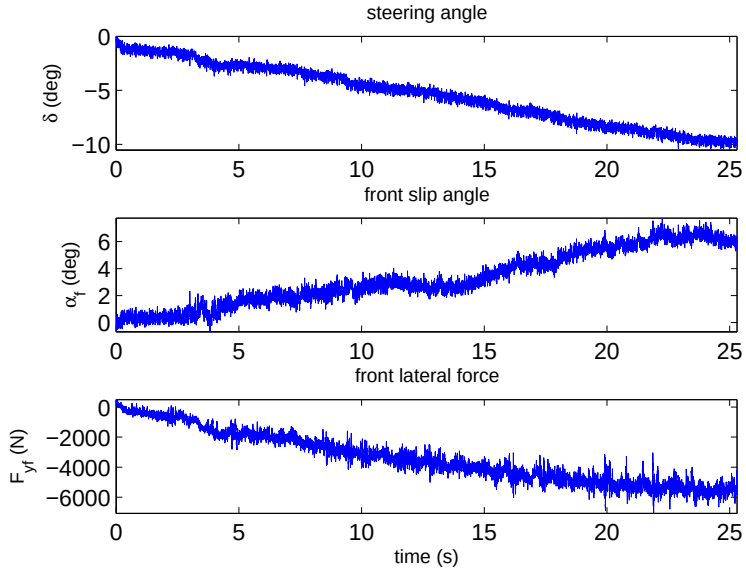

Figure 3.2: Front Lateral Force and Slip Angle

$|e_{ls} - e_{nls}| > e_{thres}$, return $\widehat{\mu} = \mu_{f-nls}$. Otherwise, hold the coefficient of friction estimate at its previous value.

As new data are collected and appended to the existing batch, we repeat the algorithm above. For real-time implementation, certain considerations should be taken to ensure adequate responsiveness to sudden changes in the road surface or driving conditions. The algorithm should be configured to "forget" older data periodically to limit the memory space required and the computation time of the data fits. A proper choice of the frequency that the data fits are applied, such as every 0.05 s, can reduce the computational load while maintaining sensitivity to changing tire parameters.

3.2.2 Experiments

The vehicle considered in this study, P1, is equipped with GPS/INS and sensors in the steer-by-wire system that allow for estimation of vehicle states and front side force. Refer to Section Fig. 2.5 for details.

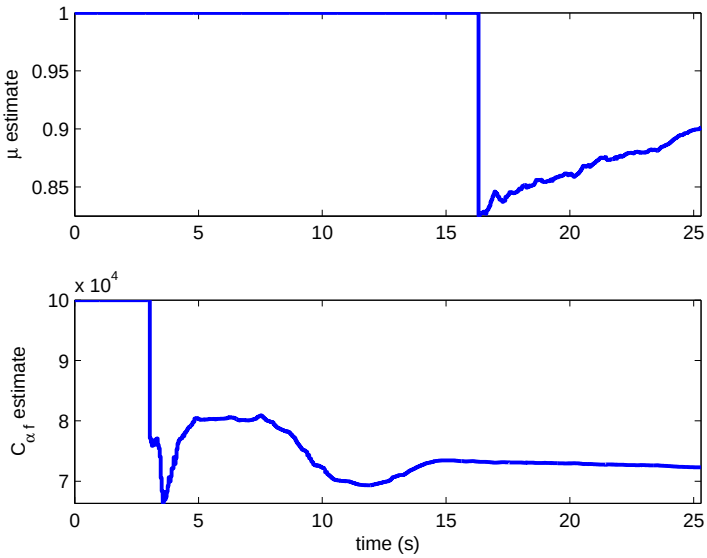

Figure 3.3: Cornering Stiffness and Friction Estimates from (F_y,α_f) Data

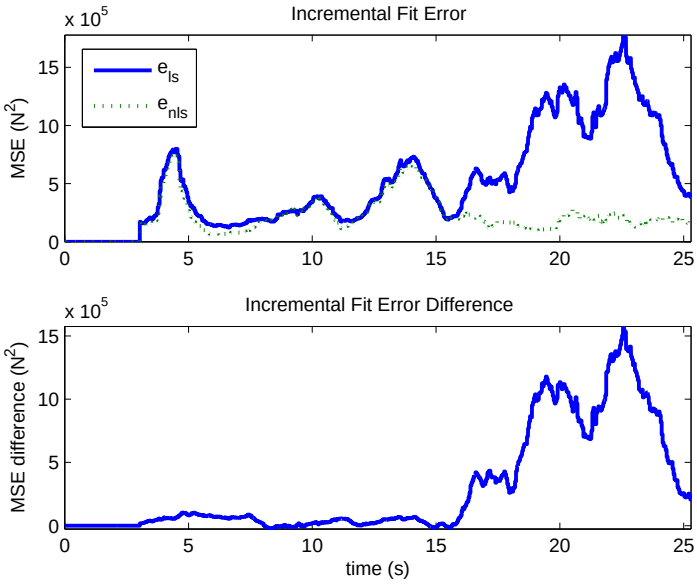

Figure 3.4: Mean Squared Error of Data Fits from (F_y,α_f) Data

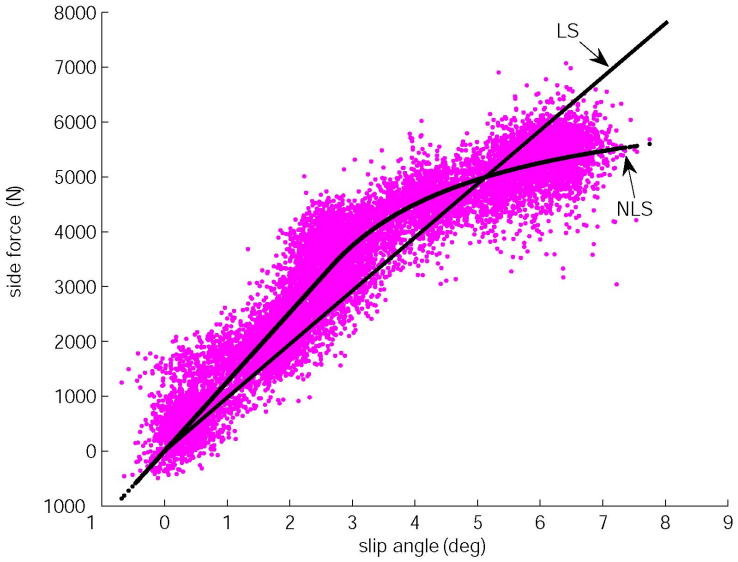

Figure 3.5: Experimental Tire Curve

Experimental data were collected at Moffett Federal Airfield at a constant, moderate speed (13.6 m/s, or 30 mph). Figure 3.2 displays the resulting front lateral force and slip angle from a right-hand ramp steer maneuver from 0 to -10 degrees at the roadwheels. With the quasi-steady state nature of the maneuver, the lateral force measurements were obtained by approximating $F_{yf} \cong F_{nf}\frac{a_y}{g}$, where a_y is the lateral acceleration measurement from an on-board accelerometer and F_{nf} is the front axle static load. Front slip angles were calculated from Eq. 3.1 using measurements from GPS/INS and a steering wheel potentiometer signal.

Using the estimation algorithm described previously with $\alpha_{thres} = 2$ deg, $\mu_o = 1$, $C_{\alpha f_o} = 100,000\,\mathrm{N/rad}$, $e_{thres} = 2x10^5\,\mathrm{N}^2$, and $N = 400$, force and slip angle data are post-processed to yield cornering stiffness and friction coefficient estimates. The MATLAB Optimization Toolbox is used to provide the NLLS fits. Shown in Fig. 3.3, the algorithm waits until the front tire slip angle exceeds α_{thres} at $t = 3\,\mathrm{s}$ before fitting the force-slip data. When $t < 16\,\mathrm{s}$, the vehicle's tires are handling in the linear regime and the incremental fit errors of LS and NLLS are comparable in magnitude (see Fig. 3.4). During this time, the estimation scheme only returns $\widehat{C}_{\alpha f}$ and holds

$\widehat{\mu}$ at the initial guess. Once the front tire forces begin to saturate at $t = 16\,\text{s}$, the incremental least squares MSE diverges from that of nonlinear least squares and the algorithm proceeds to estimate $\widehat{\mu}$.

The slight increase in the friction estimate as the maneuver progresses is expected with this method. Initially in the nonlinear tire regime, the lateral force measurements have yet to reach their peak value and the method estimates a friction value of $\widehat{\mu} = 0.83$. As more lateral force measurements becomes available, the peak force limit is reached and the friction estimate reaches a final estimate of $\widehat{\mu} = 0.9$. Note that although $\widehat{C}_{\alpha f}$ takes some time to settle down to a steady value of $72,000\,\frac{\text{N}}{\text{rad}}$, the algorithm provides relatively smooth estimates that only vary initially by $\pm 10\%$. These results are particularly encouraging given the noisiness of the force-slip data, which is illustrated in Fig. 3.5.

There are two primary shortcomings of the 'Force-Slip Regression Method'. First, in order to extract lateral force from total aligning moment, a model of pneumatic trail was employed that is only applicable to a narrow range of road and tire properties. Second, it relied on lateral force for friction identification. Basing friction estimates on lateral force necessitates waiting until the the vehicle enters the nonlinear region of handling before friction can be estimated. In the case of this experimental data set, friction is identified at approximately $0.8\,\text{g}$ of lateral acceleration, which on dry asphalt corresponds to 80% of the peak lateral force limits.

To be of greatest use to stability control systems, an estimation method needs to offer earlier knowledge of the limits and be applicable to changing road friction and tire properties. The following section addresses this issue by developing a method that is based off total aligning moment directly, rather than estimates of lateral force, as the source of information for early friction detection.

3.3 Moment-Slip Regression Method

The goal of the 'Moment-Slip Regression Method' is to utilize the early friction information contained in total aligning moment to identify cornering stiffness and friction coefficient in real-time. Just as a skilled driver senses tire grip through the feel of

the steering wheel torque, this algorithm identifies tire parameters by the shape of the aligning moment. By considering total aligning moment, rather than attempting to separate lateral force from pneumatic trail, this method overcomes the hurdles described previously arising from the 'Force-Slip Regression Method'. This method applies a combination of linear and nonlinear least squares to provide effective and continual estimates of both tire parameters. As an added advantage, the algorithm provides knowledge of μ at relatively modest lateral accelerations.

3.3.1 Real-Time Estimation Algorithm

During a maneuver, total aligning moment can be calculated in a steer-by-wire system using the linear disturbance observer developed in Section 2.4. A combination of GPS and INS to accurately determine front slip angle from Eq. (3.1). With both the aligning moment and slip angle of the front axle known, moment-slip data can be fitted to the simple aligning moment model introduced in Eqs. (2.14-2.15) to identify $C_{\alpha f}$ and μ. For $C_{\alpha f}$ estimates, moment-slip data are fitted to the τ_a model using NLLS to provide a continual estimate of $C_{\alpha f}$ given the current estimate of μ.

For identifying μ, the estimation technique is slightly more involved. First, the algorithm must determine whether the the tire forces have entered the nonlinear region before meaningful estimates of μ can be taken. In order to do this, the estimator simultaneously applies two fits to the moment-slip data: (1) LS to a linear moment model that does not include μ and (2) NLLS to the nonlinear τ_a model. The algorithm calculates the residuals of the LS and NLLS fits. If there is a significant degree of nonlinearity in the acquired data, the LS residual is large compared to that of NLLS and the method returns an estimate for μ. Otherwise, there is not sufficient information to estimate the friction coefficient and the estimate of μ is held at its previous value. As new data are collected and appended to the existing batch, the algorithm repeats this process.

The complete real-time estimation algorithm is outlined below:

1. *Find* α_f: GPS/INS measures β, r, and V_x, while a steering wheel encoder determines δ. Calculate α_f using Eq. 3.1.

2. *Find* τ_a: Determine the total aligning moment at the front tires from the linear disturbance observer in Section 2.4.

3. *Estimate* $C_{\alpha f}$ *and* μ: Iteratively perform NLLS to the τ_a model (Eqs. (2.14)-(2.15)) on the batch of moment-slip data. Start the estimates at $\widehat{C}_{\alpha f} = C_{\alpha f_o}$ and $\widehat{\mu} = \mu_o$. Once an approximate solution $(C_{\alpha f-nls}, \mu_{nls})$ is reached, return $\widehat{C}_{\alpha f} = C_{\alpha f-nls}$. To ensure that there is enough data for the NLLS fit to be meaningful, begin parameter estimation after $\alpha > \alpha_{thres}$.

   The next step is to determine whether the tire force has saturated sufficiently to estimate μ. In parallel to NLLS fit, apply the method of LS to the data points to find the slope of the line through the origin:

$$m = (\alpha_f^T \alpha_f)^{-1} \alpha_f^T \tau_a. \tag{3.6}$$

   Calculate the incremental mean squared error (MSE) of both fits from the most recent vector of data points. If the moment-slip data are sufficiently nonlinear, i.e the LS fit error exceeds the NLLS fit error above a given threshold, e_{thres}, return $\widehat{\mu} = \mu_{nls}$. Otherwise, hold the μ estimate at its previous value.

As with the previous method, certain considerations should be taken to ensure adequate responsiveness to sudden changes in the road surface or driving conditions for real-time implementation. For example, the algorithm should be configured to "forget" older data periodically to limit the memory space required and the computation time of the data fits.

The 'Moment-Slip Regression Method' can be applied to either the individual front tires or the lumped front axle. Applying it to individual tires makes the estimation scheme more involved; it requires accurate knowledge of mechanical trail and tire normal force as the vehicle experiences lateral weight transfer. In the following experimental implementation, only the front axle properties are considered for simplicity.

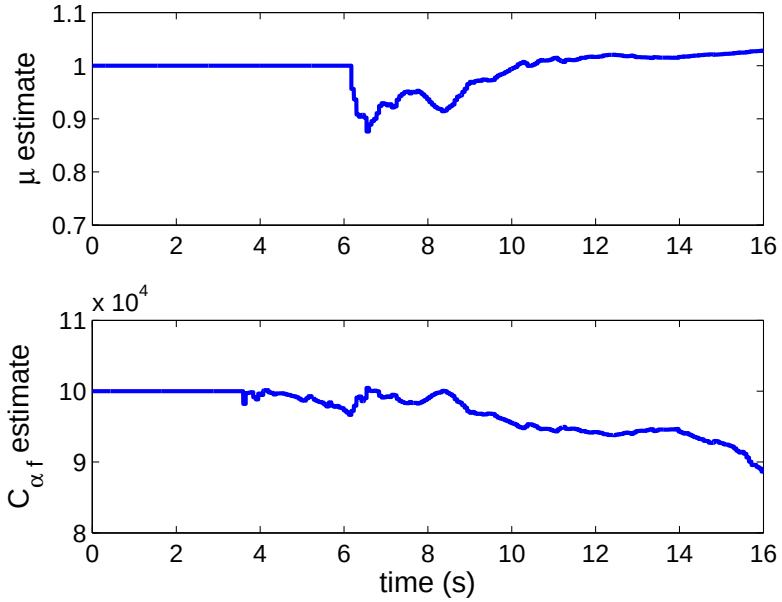

Figure 3.6: Cornering Stiffness and Friction Coefficient Estimates from (τ_a,α_f) Data

3.3.2 Experiments

The estimation algorithm is applied to the right-hand ramp steer data set in Fig. 2.12. For this right-hand maneuver, at high lateral accelerations, the mechanical trail of the outside (left) tire dominates the effect of t_m due to load transfer. Thus, the effective front mechanical trail t_m used here is taken as the left mechanical trail only. Because the front load on the axle is relatively constant during the maneuver, the front jacking torque τ_j is the lumped sum of the left and right jacking torques. With $\mu_o = 1$, $C_{\alpha f_o} = 100,000$ N/rad, and $e_{thres} = 500$ $(\text{Nm})^2$, total aligning moment and slip angle data were post-processed to yield cornering stiffness and friction coefficient estimates.

Shown in Fig. 3.6, the algorithm waits until there is sufficient data at $t = 3.8\,\text{s}$ before returning an estimate. When $t < 6\,\text{s}$, the vehicle's tires are in the linear region and the incremental fit errors of LS and NLLS are comparable in magnitude (shown in Fig. 3.7). During this time, the estimation scheme only returns an estimate for

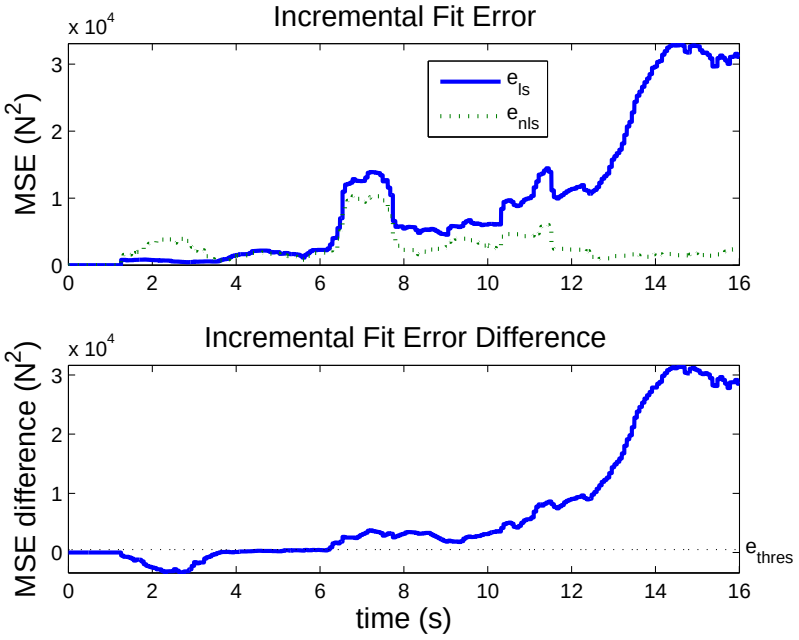

Figure 3.7: Mean Squared Error of Data Fits from (τ_a,α_f) Data

$C_{\alpha f}$ and holds μ at the initial guess. Once the front tire forces begin to deviate from linearity at $t = 6\,\text{s}$, the incremental least squares MSE diverges from that of nonlinear least squares (illustrated in Fig. 3.7) and the algorithm proceeds to estimate μ (as F_z is known from the static front axle load). Figure 3.8 illustrates the resulting NLLS fit to the total aligning moment data.

The algorithm provides an average estimate of $C_{\alpha f} = 95,000\,\frac{\text{N}}{\text{rad}}$, which is a reasonable cornering stiffness estimate of the front axle. Moreover, the estimates only vary by $\pm 5\%$. Using the simple aligning moment model, the NLLS solution converges in only 3 iterations per time step, yielding an efficient computation time.

The resulting μ estimates in Fig. 3.6 are relatively steady around $\mu = 0.95$, which agrees with skidpad testing. Even more intriguing, the algorithm is able to identify μ before the tire completely enters the nonlinear region. A steady estimate of μ is returned starting at $t = 6\,\text{s}$ (corresponding to about $0.5\,\text{g}$ of lateral acceleration, or 50% of the peak lateral force) on dry pavement.

The ability to know μ at modest accelerations is a significant result and warrants

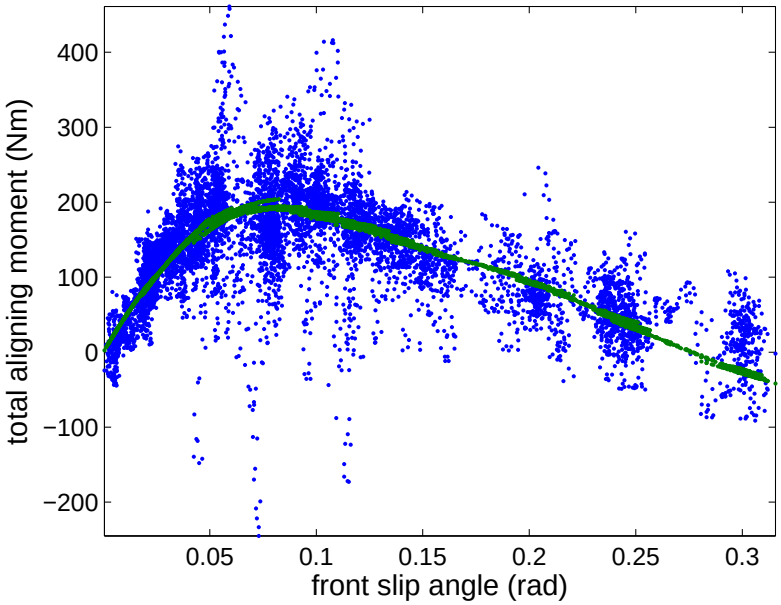

Figure 3.8: Resulting NLLS Fit to τ_a Data

further explanation. Figure 2.3 illustrates the characteristic shape of τ_a. Because pneumatic trail decreases as a function of μ even as lateral force grows linearly with slip angle, the point at which μ can be accurately identified occurs before F_{yf} completely becomes nonlinear (see Fig. 2.4). Therefore, by fitting total aligning moment data, rather than considering just lateral force alone, this technique has the added benefit of knowing the coefficient of friction *earlier*–before the tire forces reach their maximum grip on the road.

3.4 Optional Refinements

The previous regression-based methods both have the drawback of relying on persistent excitation for accurate results. In the following section, we propose two additional methods which offer some refinements that address this issue. In both methods, we separate the estimation problem into two parts: slip angle estimation and peak

friction limit estimation. To determine slip angle, both approaches rely on previously published linear observers to estimate cornering stiffness from GPS slip angle measurements. Previous literature has established that cornering stiffness can be determined from GPS-based slip angle measurements using various linear observer techniques, such as Luenberger observers or Kalman filters [7, 8]. Estimating the peak friction limits is where the two estimation methods differ. In the 'Cubic Moment Method', μF_z is solved directly from total aligning moment measurements. In the 'Linear Pneumatic Trail Method', μF_z is the determined from pneumatic trail estimates. Both methods are outlined briefly below.

3.4.1 Cubic Moment Method

In the 'Cubic Moment Method', we do not use underdeterminate techniques to identify the tire parameters, which have the drawback of requiring persistent excitation. Instead, we rely on previously published linear observers to estimate cornering stiffness from GPS slip angle measurements, and focus on developing a separate algebraic method for solving for the peak force limits using total aligning moment measurements. Thus, all that remains is to estimate μF_z.

In this approach, the peak force limits are directly solved from the simple representation of total aligning moment (which was developed in Eq. (2.14), assuming the tires have not lost lateral traction), which is a cubic function of the inverse of the peak lateral force, $I_f = \frac{1}{\mu F_z}$:

$$\begin{aligned} \tau_a \;=\; & -\left(t_m(\delta) + c_0 + c_1 \mid \tan\alpha_f \mid I_f\right) \cdot \\ & \left(c_2 \tan\alpha_f + c_3 \mid \tan\alpha_f \mid \tan\alpha_f I_f \right. \\ & \left. + c_4 \tan^3\alpha_f I_f^2\right) \end{aligned} \tag{3.7}$$

where mechanical trail t_m is a known function of steer angle δ, and the following are

known constants:

$$\begin{aligned} c_0 &= t_{p0} \\ c_1 &= -\frac{t_{p0}C_{\alpha f}}{3} \\ c_2 &= -C_{\alpha f} \\ c_3 &= \frac{C_{\alpha f}^2}{3} \\ c_4 &= -\frac{C_{\alpha f}^3}{27} \end{aligned}$$

where $C_{\alpha f}$ is the front cornering stiffness estimate and $t_{p0} = \frac{1}{6}l$ is the initial pneumatic trail where l is the contact patch length. Now with only a single unknown in I_f in the above formula, we can obtain a closed-form solution for the roots of the cubic polynomial. The remaining task is to decide how to select among the three roots as the physical peak force limits.

In general, a cubic function $f(x) = ax^3 + bx^2 + cx + d$ can have three distinct real roots, one real and a pair of complex conjugate roots, or repetitive real roots (where two roots coincide and there is a distinct third root, or there is a triple root). To distinguish among these cases, we can calculate the discriminant of the cubic, defined as

$$\Delta = -4b^3d + b^2c^2 - 4ac^3 + 18abcd - 27a^2d^2 \tag{3.8}$$

It can be shown that for the typical range of values for $C_{\alpha f}$, t_{p0}, and α_f, the discriminant for the total aligning moment function is negative. This corresponds to a single real root, which should be the physical solution of interest, and a pair of complex conjugate roots, which can be discarded.

Thus, we design the following logic for selecting the desired solution of the cubic. After we calculate the cubic roots from the closed-form solution, we select the real, positive root to be the candidate inverted peak force. Additional safeguards should be put in place when identifying μF_z given the presence of measurement noise and modeling uncertainty. First, we check that the computed peak force falls below a maximum bound defined by $\mu_{max}F_{zmax}$, where μ_{max} can be set to 1 and F_{zmax} can

correspond to a measured or modeled tire normal load (or axle normal load if only axle forces are being considered). Finally, we check to see whether the current GPS measured front slip angle exceeds the slip angle corresponding to full slip α_{sl}, which is calculated from the computed I_f solution:

$$\alpha_{sl} = \tan^{-1}\left(\frac{3}{C_{\alpha f} I_f}\right) \tag{3.9}$$

This step is added because when the tires have completely lost traction, pneumatic trail is modeled to vanish and the total aligning moment model is solely a function of mechanical trail and peak force (see Eq. (2.15)). Thus, if the tires are determined to be fulling sliding ($\alpha_f > \alpha_{sl}$), then the peak lateral force solution is calculated from Eq. (2.15):

$$I_f = \frac{t_m}{\tau_a}\text{sgn}\alpha_f \tag{3.10}$$

Otherwise, the computed I_f solution from the cubic function is used.

The advantages of this algebraic method are that it does not require persistent excitation, it can quickly react to changes in tire-road friction, and it utilizes the early friction information in total aligning moment. A drawback is that it is more sensitive to modeling errors than the previous regression methods since we are directly solving for I_f rather than applying least squares to minimize the mean-squared error.

3.5 Linear Pneumatic Trail Method

The final estimation approach presented in this chapter is the so-called 'Linear Pneumatic Trail Method'. Similar to the previous method, we rely on well-established GPS-based linear observers to estimate cornering stiffness. However, here we focus on estimating μF_z from an estimated pneumatic trail. In our model of pneumatic trail, we approximate t_p to have a linear relationships with I_f (see Eq. (2.13) for details). Thus, from an estimate of t_p, we can solve this linear model to obtain an estimate of I_f, or equivalently μF_z. Before full sliding ($\alpha_f < \alpha_{sl}$, where α_{sl} is calculated

from our previous estimate if I_f):

$$I_f = \frac{3(t_{po} - \widehat{t}_p)}{t_{po} C_{\alpha f} |\tan \alpha_f|} \tag{3.11}$$

If $\alpha_f > \alpha_{sl}$, we may utilize Eq. 3.10 to obtain the peak force estimate.

The task, therefore, becomes how we extract $\widehat{t}_p$ from the total aligning moment and slip angle measurements. One way to do this is to solve:

$$\widehat{t}_p = -\left(\frac{\tau_a}{\widehat{F}_y} + t_m(\delta)\right). \tag{3.12}$$

where $\widehat{F}_y$ is an estimated lateral force and mechanical trail t_m is determined kinematically as a function of the measured steer angle δ. This equation can be solved using iterative (algebraic loop) techniques. Or, in a discrete time estimator, the previous estimate of $\widehat{F}_y = \text{Fiala}\left(\alpha_f, \widehat{I}_{fprev}\right)$ using Eq. 2.9 can be used as a proxy for the current estimate.

The advantages of this method is that it removes the need to select among multiple algebraic solutions, as was the case with the 'Cubic Moment Method', it does not suffer from the need of persistent excitation, and directly utilizes the early friction information contained in pneumatic trail for friction limit estimation. A drawback is that it is expected to be sensitive to modeling errors. Also, care must be taken to ensure that obtaining an estimate of pneumatic trail from an estimated lateral force yields a stable, reasonable solution even in the presence of estimation uncertainty.

Due to the similarity of their performances with the approach presented in Section 4.5.3 of Chapter 4, experimental results for both the 'Cubic Moment Method' and 'Linear Pneumatic Trail Method' are not presented in this thesis. However, the reader may refer to Section 4.5.3 to view the peak force estimates obtained via algebraic methods.

3.6 Conclusions

This chapter introduced effective algorithms to estimate cornering stiffness and friction coefficient from available steering torque information in a steer-by-wire system. The first method, the so-called 'Force-Slip Regression Method' relied on lateral force and GPS measurements, applying a combination of LS and NLLS to identify the tire parameters. Although cornering stiffness and friction were accurately identified using this algorithm in experiment, lateral-force based friction estimation required high levels of lateral excitation. Moreover, the simplified representation of pneumatic trail limited the applicability of this method to different road and tire properties. Experimental results showed that the front tires needed to achieve 80% of the peak lateral force capability before friction could be confidently identified.

By contrast, the second estimation approach, referred to as the 'Moment-Slip Regression Method', identified the same tire parameters using total aligning moment and GPS-based slip angle measurements. An important benefit of this approach was an earlier knowledge of the coefficient of friction, with accurate friction estimates when the tires achieved only 50% of the peak available tire force, which corresponds to the border of linear tire handling.

Finally, two algebraic methods were introduced. Both relied on linear observers presented in previous literature to obtain cornering stiffness estimates from GPS slip angle measurements. To determine the peak force limits, the methods inverted the algebraic models for total aligning moment and pneumatic trail to directly compute μF_z. These methods still utilize the early friction information in total aligning moment and pneumatic trail, and do not require persistent excitation for accurate results. However, as algebraic methods, they rely more heavily on accurate models and require safeguards to ensure peak force estimates are within physical bounds.

In the next chapter, we remove the assumption that GPS is continually available and design methods to characterize lateral tire force without the need for costly sensors.

Chapter 4

Lateral Limit Estimation Without Reliance on GPS

4.1 Introduction

Demonstrated in the previous chapter, knowledge of total aligning moment (from the steering system) and slip angle (from GPS) enables accurate estimation of a tire's lateral properties. Although the results from the previous chapter are promising, they rely on the availability of GPS for slip angle measurements. Unfortunately, GPS technology requires satellite visibility, which may be lost periodically in urban and forested driving environments. Cornering stiffness changes on a slower time scale as a function of tire wear, pressure and temperature [52]. Since it is reasonable to assume that noticeable cornering stiffness variation occurs relatively slowly, intermittent access to GPS does not affect availability of cornering stiffness estimates. However, both peak lateral force limits (determined by tire-road friction coefficient and tire normal force) and slip angle can change rapidly with road surface conditions or during emergency maneuvers. Therefore, during periods of GPS signal loss, it is important to be able to estimate these two quantities, tire slip angle α and the peak friction limit μF_z, *without* reliance on GPS.

The lack of GPS slip angle measurements eliminates the possibility of using the

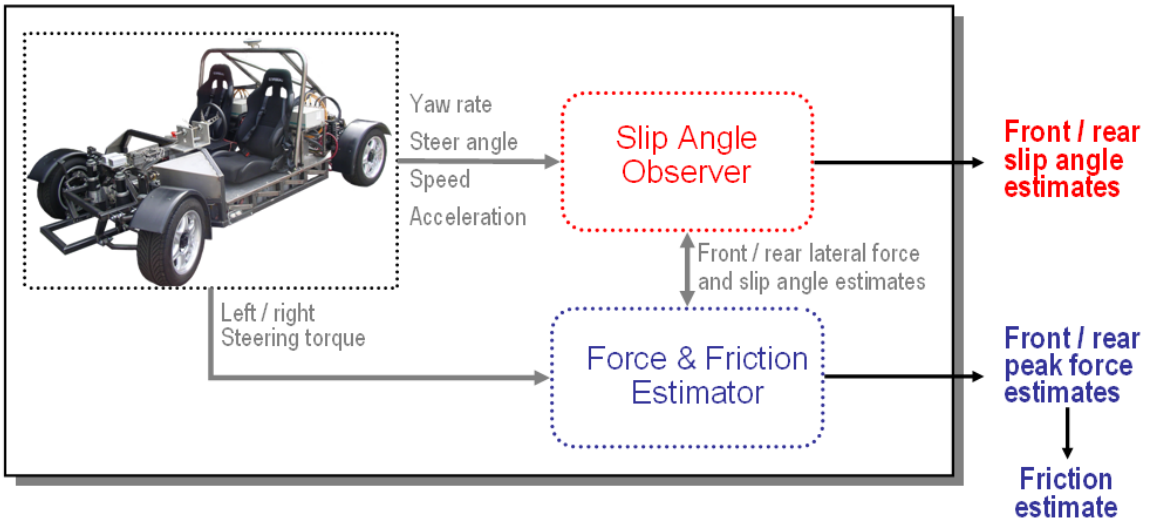

Figure 4.1: Observer Block Diagram

regression techniques proposed by the 'Force-Slip Regression' and 'Moment-Slip Regression' methods from the previous chapter. However, the algebraic approaches taken to solve for the peak friction limit from total aligning moment in the 'Cubic Moment Method' or pneumatic trail in the 'Linear Pneumatic Trail Method' may still be considered. This chapter devises and investigates two methods that incorporate these algebraic estimation approaches with a new, nonlinear slip angle observer, which provides estimates of tire slip angle.

Both estimation methods discussed in this chapter share a common structure, illustrated in Fig. 4.1. From onboard automotive-grade sensors, the slip angle observer receives measurements of vehicle yaw rate, lateral acceleration, steer angle and longitudinal speed, and outputs estimates of front and rear axle slip angles. The friction and force estimator block receives measurements of steering torque (recall that our research vehicle P1 has separate left/right steering capability), which in combination with the slip angle estimates outputted from the slip angle observer, computes estimates of front and rear lateral force and the peak friction limits. If desired, the peak friction limits can be used to provide estimates of the tire-road friction coefficient using measured or modeled normal force information.

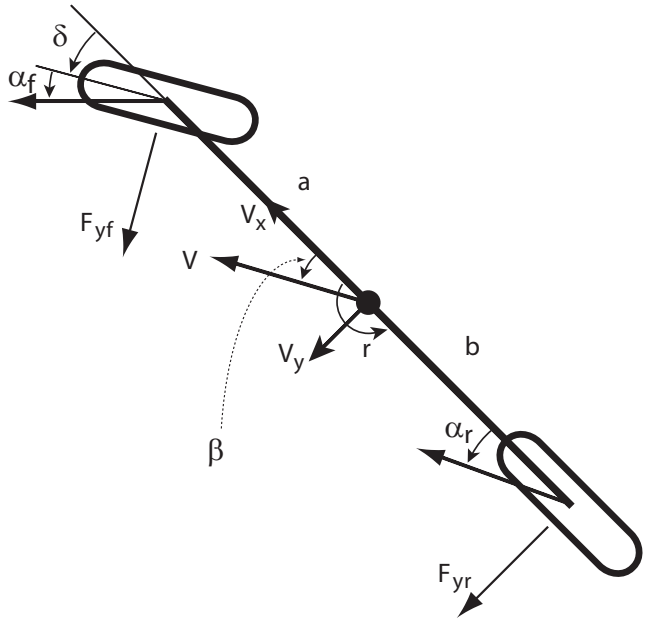

Figure 4.2: Bicycle Model

As shown in the block diagram, both estimation blocks rely on each other's estimates to output their own estimates. Due its highly coupled nature, a central issue investigated in this chapter is the stability of the overall estimation scheme. Care must be taken to ensure that errors in either α or μF_z estimates do not cause the entire observer to grow unstable.

4.2 Slip Angle Observer Block

Because GPS slip angle measurements are no longer available, we must estimate it. To estimate tire slip angle, we use the vehicle's equations of motion to model how slip angle evolves as a function of the vehicle's lateral tire forces. The vehicle model used is a two-wheel planar bicycle model (shown in Fig. 4.2) with nonlinear front and

rear tire forces, F_{yf} and F_{yr} respectively:

$$\dot{\beta} = \frac{1}{mV_x}(F_{yf} + F_{yr}) - r \tag{4.1}$$

$$\dot{r} = \frac{1}{I_z}(aF_{yf} - bF_{yr}), \tag{4.2}$$

where a and b are the distances of the front and rear axles from the CG, sideslip angle β is the angle between the vehicle's heading and the direction of its velocity, r is the yaw rate, I_z is the moment of inertia, and m is the vehicle mass. It is assumed that the longitudinal vehicle speed V_x is constant. From kinematics, the front and rear axle slip angles α_f and α_r, respectively, are linearized to be:

$$\alpha_f = \beta + \frac{ar}{V_x} - \delta \tag{4.3}$$

$$\alpha_r = \beta - \frac{br}{V_x} \tag{4.4}$$

where δ is the steer angle at the tire.

To update our estimate of slip angle, we can derive the feedforward term of the update equation by taking the derivative Eq. (4.3) and substituting in Eqs. (4.1) and (4.2):

$$\dot{\alpha}_f = \left(\frac{1}{mV_x} + \frac{a^2}{I_z V_x}\right) F_{yf} + \left(\frac{1}{mV_x} - \frac{ab}{I_z V_x}\right) F_{yr} - r - \dot{\delta}. \tag{4.5}$$

The estimate of slip angle depends on the estimated front and rear axle lateral forces, F_{yf} and F_{yr}, respectively, which are outputted from the force and friction estimation block. From the introduction of the algebraic estimation methods in Chapter 3, we have two possible ways of determining μF_z from total aligning moment measurements (which can be used to compute F_{yf} and F_{yr}): solving the cubic aligning moment relationship or solving the affine pneumatic trail model. The algorithms and stability of both approaches are discussed below.

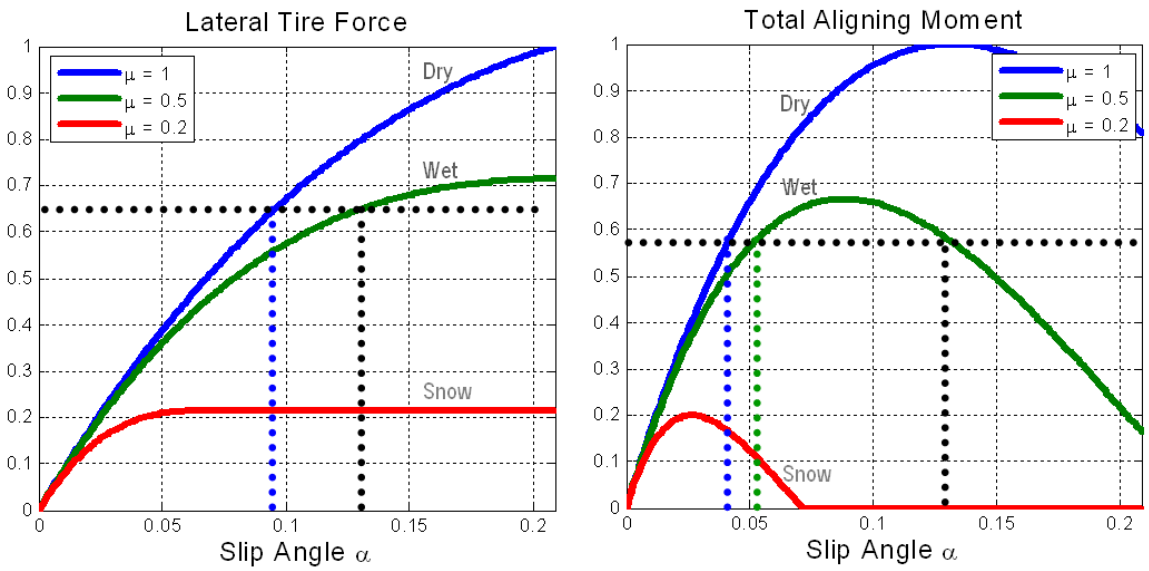

Figure 4.3: Decoding α and μF_z from F_y and τ_a

4.3 Force and Friction Estimator Block

Although both of the estimation approaches described below share the same slip angle observer block to estimate tire slip angles, they differ in how to compute the peak friction limits.

4.3.1 Total Aligning Moment Nonlinear Observer

The concept of the 'Total Aligning Moment Nonlinear Observer' method is to use a combination of lateral force and total aligning moment to decode tire slip angle and the peak friction limit. Figure 4.3 illustrates how this is achieved. The figure plots the normalized lateral force and total aligning moment (with mechanical trail $t_m = 0$ for illustration purposes) for three different tire-road coefficients of friction corresponding to dry, wet, and snowy roads. In this example, if only an estimate of lateral force were available, the tire could be on a dry road at a lower slip angle, or a wet road at a higher slip angle. However, with the added measurement of total aligning moment, we know that the tire must be deformed at the same slip angle and

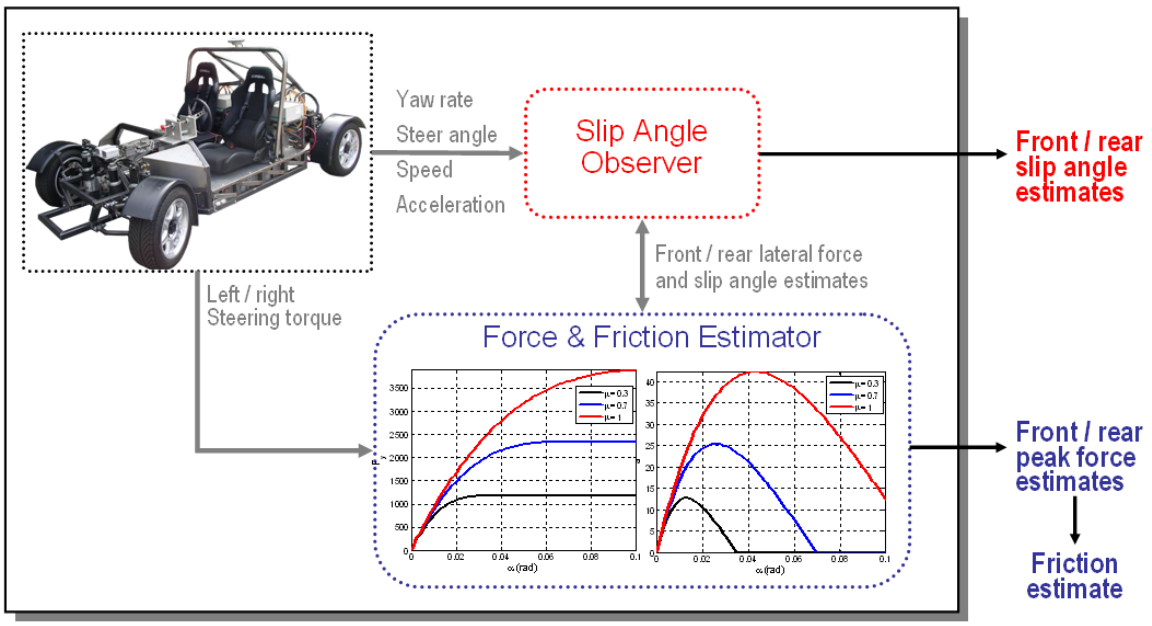

Figure 4.4: Total Aligning Moment Nonlinear Observer Block Diagram

traveling on the same friction surface, which allows us to determine that $\alpha = 0.13\,\text{rad}$ and $\mu = 0.5$.

The block diagram for this approach is shown in Fig. 4.4. The next section provides this method's real-time estimation algorithm.

Real-time Estimation Algorithm

Prior to beginning estimation, the initial front axle slip angle $\widehat{\alpha}_{fo}$ is set to zero (i.e. the vehicle is driving straight) and inverted front peak lateral force $\widehat{I}_{fo}$ is set to

$$I_{fnom} = \frac{1}{\mu_{nom} F_{zfnom}} \tag{4.6}$$

where the nominal friction coefficient $\mu_{nom} = 1$, and F_{zfnom} is the nominal front axle load. Given that P1 only has sensing capability on the front tires, we use kinematics to calculate the rear slip angle estimate $\widehat{\alpha}_r$ from $\widehat{\alpha}_f$ using Eq. 4.4. We also can obtain the estimated inverted rear peak force $\widehat{I}_r$ from $\widehat{I}_f$ by neglecting longitudinal weight

transfer.

Now, at every time step, the outline for the algorithm is as follows:

1. Calculate the front/rear lateral force estimates $\widehat{F}_{yf}$ and $\widehat{F}_{yr}$ from the current estimates of $\widehat{\alpha}_f$, $\widehat{\alpha}_r$, $\widehat{I}_f$ and $\widehat{I}_r$ using the Fiala tire model in Eq. (2.9).

2. Update the estimates of front/rear slip angles $\widehat{\alpha}_f$ from $\widehat{\alpha}_r$ using Eq. (4.12).

3. Update the estimates of front/rear (inverted) peak friction limits $\widehat{I}_f$ and $\widehat{I}_r$ from the total aligning moment measurement.

Because the first two steps of the above algorithm are identical to those presented later in Section 4.3.2, we refer the reader to that section for details. We include the details of the third step below.

To identify the peak force limits (as before with the 'Cubic Moment Method'), we directly solve it from the model of total aligning moment in Eqs. (2.14)-(2.15). This model is a cubic function of the inverse of the peak lateral force I_f and now also dependent on the *estimated* front slip angle $\widehat{\alpha}_f$:

$$\begin{aligned} \tau_a &= -\left(t_m(\delta) + c_0 + c_1 \mid \tan\widehat{\alpha}_f \mid I_f\right) \cdot \\ &\quad \left(c_2 \tan\widehat{\alpha}_f + c_3 \mid \tan\widehat{\alpha}_f \mid \tan\widehat{\alpha}_f I_f \right. \\ &\quad \left. + c_4 \tan^3\widehat{\alpha}_f I_f^2\right) \end{aligned} \tag{4.7}$$

where mechanical trail t_m is a known function of steer angle δ, and the following are known constants:

$$\begin{aligned} c_0 &= t_{p0} \\ c_1 &= -\frac{t_{p0} C_{\alpha f}}{3} \\ c_2 &= -C_{\alpha f} \\ c_3 &= \frac{C_{\alpha f}^2}{3} \\ c_4 &= -\frac{C_{\alpha f}^3}{27} \end{aligned}$$

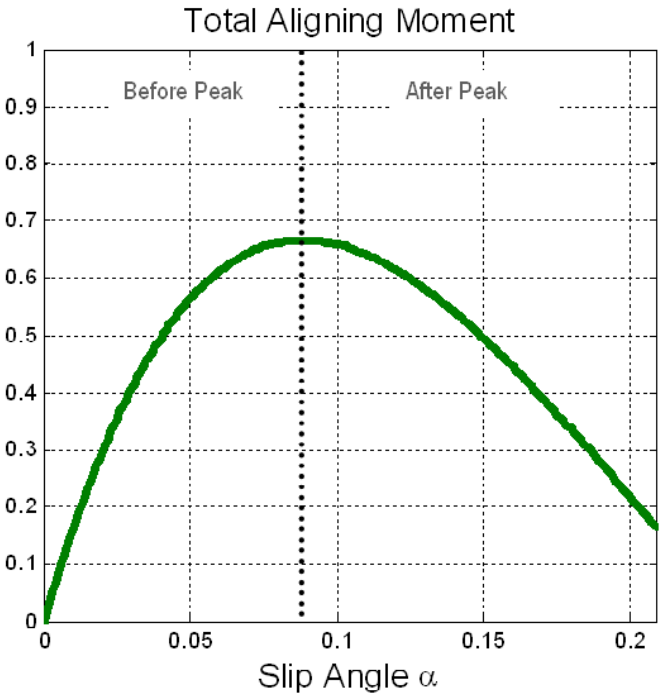

Figure 4.5: Total Aligning Moment Operating Regions

where $C_{\alpha f}$ is the front cornering stiffness estimate and $t_{p0} = \frac{1}{6}l$ is the initial pneumatic trail where l is the contact patch length. Now with only a single unknown in I_f in the above formula, we can obtain a closed-form solution for the roots of the cubic polynomial. To decide which of the three roots corresponds to the physical peak force limits, we employ identical logic introduced in Section 3.4.1.

Stability

In the 'Total Aligning Moment Nonlinear Observer' method, errors in either the slip angle estimate affects the peak friction limit estimate, and vice versa. Therefore, it is important that we check the stability of this coupled estimation scheme to ensure that there is convergence even in the presence of estimation error.

Without loss of generality, let us assume that $\widehat{\alpha}_f > 0$. There are two possible cases:

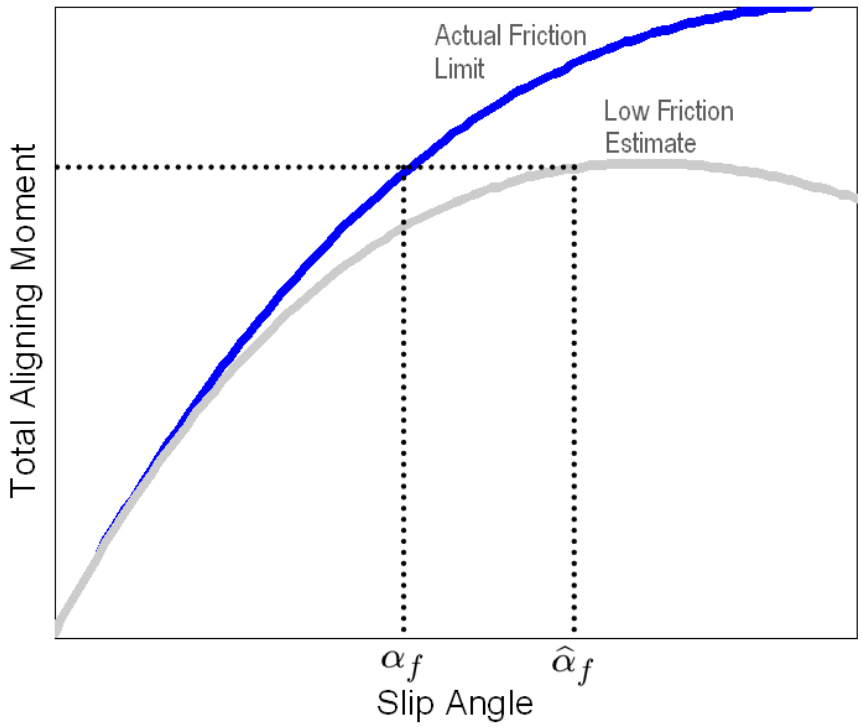

Figure 4.6: Friction limit estimate is low due to $\widehat{\alpha}_f \geq \alpha_f$

Case 1: Slip angle estimate is greater or equal than actual ($\widehat{\alpha}_f \geq \alpha_f$)

Case 2: Slip angle estimate is less than actual ($\widehat{\alpha}_f < \alpha_f$)

Within each case, there are two different scenarios: the tire can be (a) operating before the total aligning moment peak or (b) operating after the peak (as shown in Fig. 4.5). Thus, in total, there are four possible cases to consider.

First, let us consider the Case 1(a) where $\widehat{\alpha}_f \geq \alpha_f$ and the tire is operating before the peak of the curve. Because the slip angle estimate is too large, the resulting friction limit estimate is lower than the actual value. To demonstrate this, Fig. 4.6 plots the total aligning moment curve corresponding to the actual friction limits, and the resulting curve corresponding to a low friction estimate due to the fact that the slip angle estimate is too large. As a result, the slip angle observer is given a friction limit estimate that is too low and incorrectly believes that the tire is traveling on a lower friction surface. As evident from Fig. 4.4, for a given amount of lateral force, a

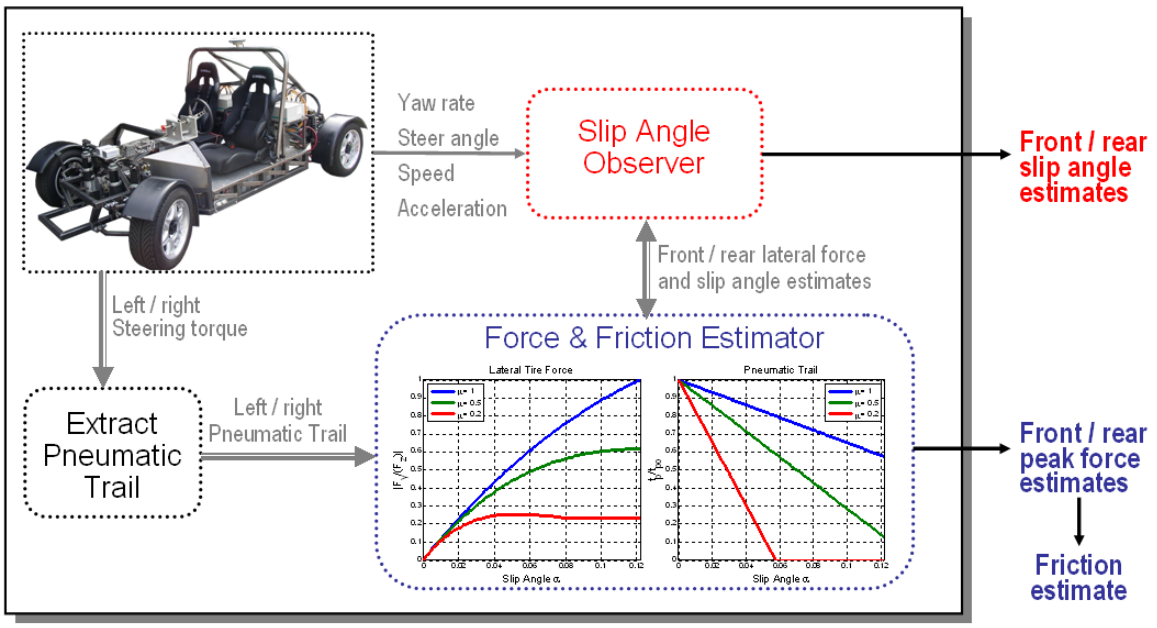

Figure 4.7: Pneumatic Trail Nonlinear Observer Block Diagram

low friction estimate results in the observer further *increasing* the slip angle estimate. Recalling that the slip angle estimate was too large to begin with, this scenario quickly results in instability of the overall observer.

It is possible to show that the remaining three cases – when the slip angle estimate is too small (before the peak) or when the tire is operating after the total aligning moment peak – produce stable convergence. However, uncovering a scenario where the observer is unstable eliminates the possibility of using this estimation technique. In the next section, we show that the algebraic method of solving the affine model of pneumatic trail for the peak friction limits does not suffer from the same problem.

4.3.2 Pneumatic Trail Nonlinear Observer

In the 'Pneumatic Trail Nonlinear Observer', we apply an alternative way of determining the peak friction limits is applying the method introduced in 'Linear Pneumatic Trail Method'. That is, we use the affine model of pneumatic trail as a function of the peak friction limits to extract μF_z. Figure 4.7 presents the block diagram for

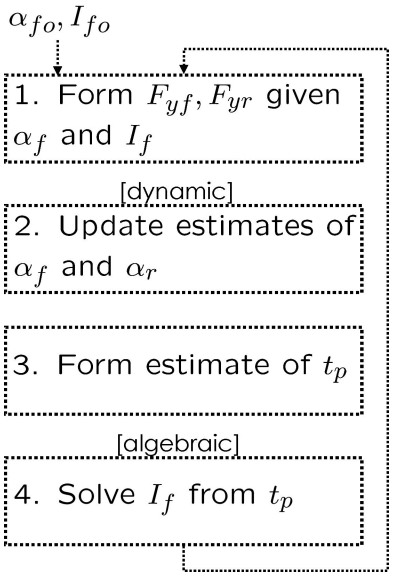

Figure 4.8: Estimation Algorithm

this method in which the force and friction estimation block uses pneumatic trail and lateral force information to decode μF_z.

Real-Time Estimation Algorithm

Prior to beginning estimation, the initial front axle slip angle $\widehat{\alpha}_{fo}$ is set to zero (i.e. the vehicle is driving straight) and inverted front peak lateral force $\widehat{I}_{fo}$ is set to

$$I_{fnom} = \frac{1}{\mu_{nom} F_{zfnom}} \tag{4.8}$$

where the nominal friction coefficient $\mu_{nom} = 1$, and F_{zfnom} is the nominal front axle load. Outlined in Fig. 4.8, the estimation algorithm is as follows:

1. **Form estimates of lateral force.**

   With an estimate of front slip angle, the rear slip angle estimate is obtained by combining Eqs. (4.3) and (4.4):

$$\widehat{\alpha}_r = \widehat{\alpha}_f + \delta - \frac{(a+b)r}{V_x} \tag{4.9}$$

where δ is measured from onboard steering encoders, r is measured from onboard INS, and V_x is determined by wheel speed sensors.

Assuming that the vehicle is traveling on an even road surface, the friction coefficients for the front and rear axles are be assumed to be equal. Neglecting the effects longitudinal weight transfer, the inverted rear axle peak force is

$$\widehat{I}_r = \frac{\widehat{I}_f F_{zfnom}}{F_{zrnom}}, \tag{4.10}$$

where F_{zrnom} is the nominal rear axle load and $\widehat{I}_f$ is the inverted front axle peak force estimate. Using the Fiala tire force model in Eq. (2.9), the rear axle force $\widehat{F}_{yr}$ is calculated based on the current estimates $\widehat{I}_r$ and $\widehat{\alpha}_r$. For the front lateral force $\widehat{F}_{yf}$, we treat the left and right tires separately and sum their lateral force contributions:

$$\widehat{F}_{yf} \;=\; \widehat{F}_{yfl} + \widehat{F}_{yfr}. \tag{4.11}$$

where $\widehat{F}_{yfl}$ and $\widehat{F}_{yfr}$ are calculated using Eq. 2.9 based on $\widehat{\alpha}_f$ and their respective friction limit estimates.

2. **Update estimates of front/rear slip angle.**

The update equation for the front slip angle is derived by taking the derivative of Eq. (4.3) and substituting in Eqs. (4.1)-(4.2):

$$\dot{\alpha}_f \;=\; \left(\frac{1}{mV_x} + \frac{a^2}{I_z V_x}\right) F_{yf} + \left(\frac{1}{mV_x} - \frac{ab}{I_z V_x}\right) F_{yr} - r - \dot{\delta}. \tag{4.12}$$

Thus, to update $\widehat{\alpha}_f$, we may integrate the following observer update law:

$$\begin{aligned} \dot{\widehat{\alpha}}_f \;=\; & \left(\frac{1}{mV_x} + \frac{a^2}{I_z V_x}\right) \widehat{F}_{yf} + \left(\frac{1}{mV_x} - \frac{ab}{I_z V_x}\right) \widehat{F}_{yr} - r - \dot{\delta} \\ & + K(\widehat{F}_{yf} + \widehat{F}_{yr} - ma_y) \end{aligned} \tag{4.13}$$

where K is the observer feedback gain and a_y is the lateral acceleration measurement. However, to avoid having to take the derivative of the measured steer angle signal δ, we rearrange the update the equation as

$$\begin{aligned}\dot{\widehat{\alpha}}_f + \dot{\delta} &= \left(\frac{1}{mV_x} + \frac{a^2}{I_z V_x}\right)\widehat{F}_{yf} + \left(\frac{1}{mV_x} - \frac{ab}{I_z V_x}\right)\widehat{F}_{yr} - r \\ &\quad + K(\widehat{F}_{yf} + \widehat{F}_{yr} - ma_y). \end{aligned} \tag{4.14}$$

We may integrate this update equation instead and subtract away δ after integration. Once $\widehat{\alpha}_f$ is updated, it is straightforward to update the rear slip estimate $\widehat{\alpha}_r$ from the kinematic relationship described in Eq. (4.9).

3. **Form pneumatic trail estimate.**

   In this step, we consider the front tires separately. To construct an estimated left pneumatic trail $\widehat{t}_{pl}$ for the left tire, we use the measured total aligning moment for the left tire τ_{al} extracted from the disturbance observer designed in [26] and lateral force estimate $\widehat{F}_{yfl}$:

$$\widehat{t}_{pl} = -\left(\frac{\tau_{al}}{\widehat{F}_{yfl}} + t_{ml}\right) \tag{4.15}$$

   where the left mechanical trail t_{ml} is determined kinematically as a function of the measured steer angle [31]. For the right tire, we perform an analogous calculation to construct an estimated right pneumatic trail $\widehat{t}_{pr}$.

   A three-point moving average filter is included in the calculations of $\widehat{t}_{pl}$ and $\widehat{t}_{pr}$ to prevent the dynamics of the estimates from changing faster than the physical system. (The length of the filter can be adjusted according to the system's sampling rate and level of sensor measurement noise.)

4. **Use pneumatic trail to solve for peak lateral force.**

   From the pneumatic trails, the linear model in Eq. (2.13) is used to solve for the estimated inverted peak lateral force of the left and right tires, $\widehat{I}_{fl}$ and $\widehat{I}_{fr}$,

respectively. Before full sliding ($\widehat{\alpha}_f < \widehat{\alpha}_{fsl}$), the estimates are:

$$\widehat{I}_{fl} = \frac{3(t_{po} - \widehat{t}_{pl})}{t_{po} C_{\alpha fl} |\tan \widehat{\alpha}_f|} \tag{4.16}$$

$$\widehat{I}_{fr} = \frac{3(t_{po} - \widehat{t}_{pr})}{t_{po} C_{\alpha fr} |\tan \widehat{\alpha}_f|} \tag{4.17}$$

where t_{po} is the initial pneumatic trail length and $C_{\alpha fl}$ and $C_{\alpha fr}$ are the front left and right tire cornering stiffnesses, respectively. After full sliding, the inverted peak force estimates are:

$$\widehat{I}_{fl} = \frac{t_{ml}}{\tau_{al}} \text{sgn} \widehat{\alpha}_f \tag{4.18}$$

$$\widehat{I}_{fr} = \frac{t_{mr}}{\tau_{ar}} \text{sgn} \widehat{\alpha}_f \tag{4.19}$$

Finally, we may lump the left/right peak forces to find the front axle peak force estimate, $\frac{1}{\widehat{I}_f}$:

$$\frac{1}{\widehat{I}_f} = \frac{1}{\widehat{I}_{fl}} + \frac{1}{\widehat{I}_{fr}}. \tag{4.20}$$

We highlight that the strength of this estimation method lies in the fact that pneumatic trail provides sufficiently early information of the limits of tire adhesion *before* they affect lateral tire force generation (and therefore would alter our estimate of slip angles). While initially operating in the linear region of handling, slip angle is only proportional to cornering stiffness and unaffected by the friction limit. This enables accurate tracking of slip angle even when we have insufficient knowledge of the limits of tire adhesion. However, pneumatic trail conveniently provides knowledge of the friction limit before the tires exit the linear region of handling, and we are able to continue accurate slip angle tracking up the limits of handling.

4.3.3 Experimental Implementation Considerations

To interpret the performance of the observer, it may be desirable to know the tire-road coefficient of friction estimate $\widehat{\mu}$, rather than peak lateral force. This can easily be

calculated. Given the prior assumption that longitudinal weight transfer is negligible and the vehicle is traveling on an even surface, $\widehat{\mu}$ is derived directly from the peak force estimate of the front axle:

$$\widehat{\mu} = \frac{1}{\widehat{I}_f F_{zfnom}}. \tag{4.21}$$

The final friction coefficient estimate may be put through a 100-point moving average filter to obtain smoother estimates, which for a 500 Hz sampling rate translates to the assumption that the road friction can change as quickly as every 0.2 s.

For onboard implementation, we must remember that when the vehicle is traveling straight or nearly straight, lateral limit estimation is imprecise given the lack of lateral dynamics. During these situations, we must suspend peak force (friction) estimation, holding it at its latest known or nominal value. Quantitatively, this translates to waiting to observe a decrease in pneumatic trail from its initial value ($\widehat{t_p} < t_{po}$) and a slip angle bounded away from zero ($|\widehat{\alpha}_f| > \alpha_{thres}$) before the peak force estimation can be meaningful.

Some additional considerations should be taken to ensure the algorithm outputs physically reasonable estimates. Because the slip angle is expected to change at a frequency of 1-5 Hz, the total aligning moment measurement should be low-pass filtered at the tire hop frequency (f = 10-15 Hz) to prevent the high frequency road disturbances from being propagated to the slip angle estimate. For a 500 Hz sampling rate, this amounts to a moving average filter of 38-50 sample times. For consistency, the slip angle estimates should be low-pass filtered at the same frequency. Other signals such as yaw rate and lateral acceleration should be similarly conditioned prior to using them in the algorithm.

Finally, due to expected pneumatic trail modeling errors and noisy measurements, some simple logic can be included in Step 4 of the algorithm to protect the peak force estimate from exceeding a nominal peak force value. This nominal value can correspond to a high-friction surface and tire normal load as determined by the static

weight transfer model in Eqs. (2.17-2.19):

$$\frac{1}{\widehat{I}_{fl}} = \min\left\{\frac{1}{\widehat{I}_{fl}}, \mu_{nom}F_{zfl}\right\} \tag{4.22}$$

$$\frac{1}{\widehat{I}_{fr}} = \min\left\{\frac{1}{\widehat{I}_{fr}}, \mu_{nom}F_{zfr}\right\}. \tag{4.23}$$

In the absence of normal load measurements, a load transfer model can be used, which requires knowledge of roll angle. For convenience, roll angle measurements and roll stiffness are obtained through a combination of onboard GPS and INS measurements [49]. However, in the absence of GPS, Tseng has shown that one can separate lateral dynamics from road disturbances to obtain accurate roll angle measurements in dynamic maneuvers [61].

4.4 Pneumatic Trail Nonlinear Observer Stability Proof

Consider a front slip angle error defined as

$$e_\alpha = \widehat{\alpha}_f - \alpha_f \tag{4.24}$$

where α_f is the actual (unknown) front slip angle.

Suppose the following three conditions hold:

1. The error due to lateral force modeling errors and parameter uncertainty is bounded by a maximum force error ΔF_y.

2. The local cornering stiffnesses of the front and rear axles, $\widetilde{C}_{\alpha f}$ and $\widetilde{C}_{\alpha r}$, are not both zero (meaning the vehicle is not in a full lateral skid) and the observer feedback gain K is chosen such that

$$K > \left|\frac{1}{mV_x} - \frac{ab}{I_zV_x}\right|. \tag{4.25}$$

3. Let us define the nonlinear handling region as

$$|F_{yf} - F_{yflin}| \geq \Delta F_y \tag{4.26}$$
$$|F_{yr} - F_{yrlin}| \geq \Delta F_y \tag{4.27}$$

where the linear forces are approximated by

$$F_{yflin} = -C_{\alpha f}\alpha_f \tag{4.28}$$
$$F_{yrlin} = -C_{\alpha r}\alpha_r. \tag{4.29}$$

When the tires are operating in this region, the error in the estimated pneumatic trail $\widehat{t_p}$ (for both the front left and right tires) is bounded by

$$\left|\widehat{t_p} - t_p\right| < \frac{t_{po}C_{\alpha f}I_f}{3}\frac{K\Delta F_y}{\gamma}. \tag{4.30}$$

where t_p is the actual (unknown) pneumatic trail and

$$\begin{aligned} \gamma &= K_f\widetilde{C}_{\alpha f} + (K_r + K)\widetilde{C}_{\alpha r} \\ K_f &= \frac{1}{mV_x} + \frac{a^2}{I_zV_x} \\ K_r &= \frac{1}{mV_x} - \frac{ab}{I_zV_x}. \end{aligned}$$

Then, as the following proof shows, the slip angle estimation error is stable and bounded by

$$|e_\alpha| \leq \frac{K\Delta F_y}{\gamma} = \frac{K\Delta F_y}{K_f\widetilde{C}_{\alpha f} + (K_r + K)\widetilde{C}_{\alpha r}}. \tag{4.31}$$

In the special case where we have perfect knowledge of lateral force ($\Delta F_y = 0$), then asymptotic stability of the slip angle estimation error is guaranteed, i.e. $\widehat{\alpha}_f \to \alpha_f$ and $\widehat{\alpha}_r \to \alpha_r$ as $t \to \infty$.

4.4.1 Proof

For asymptotic stability [53], we would like to show a positive real γ exists such that:

$$\dot{e}_\alpha \leq -\gamma e_\alpha. \tag{4.32}$$

By taking the derivative of Eq. (4.24) and substituting in the front slip angle update law from the nonlinear observer, the slip angle estimation error dynamics are

$$\begin{aligned} \dot{e}_\alpha &= \dot{\widehat{\alpha}}_f - \dot{\alpha}_f & (4.33)\\ &= \underbrace{\left(\frac{1}{mV_x} + \frac{a^2}{I_z V_x}\right)}_{K_f}\left(\widehat{F}_{yf} - F_{yf}\right) + \underbrace{\left(\frac{1}{mV_x} - \frac{ab}{I_z V_x}\right)}_{K_r}\left(\widehat{F}_{yr} - F_{yr}\right) \\ &\quad + K\left(\widehat{F}_{yf} + \widehat{F}_{yr} - ma_y\right). & (4.34) \end{aligned}$$

As the lateral force estimation error is bounded by ΔF_y (Condition 1), we may rewrite the feedback term in Eq. 4.34 as:

$$K\left(\widehat{F}_{yf} + \widehat{F}_{yr} - ma_y\right) = K\left(\widehat{F}_{yr} - F_{yrmeas}\right) \tag{4.35}$$

where

$$\begin{aligned} F_{yrmeas} &= ma_y - \widehat{F}_{yf} & (4.36)\\ |F_{yrmeas} - F_{yr}| &\leq \Delta F_y. & (4.37) \end{aligned}$$

Now Eq. (4.34) can be rewritten as

$$\dot{e}_\alpha \leq K_f\left(\widehat{F}_{yf} - F_{yf}\right) + (K_r + K)\left(\widehat{F}_{yr} - F_{yr}\right) + K\Delta F_y \tag{4.38}$$

Without loss of generality, assume that $\widehat{\alpha}_f > 0$. Then, let us consider two possible cases of estimation error:

Case 1: Slip angle estimate is greater or equal than actual

Case 2: Slip angle estimate is less than actual

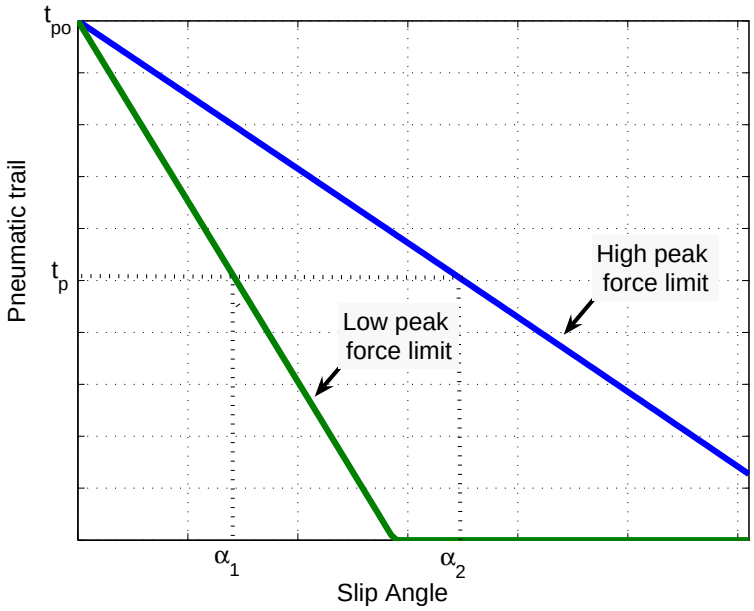

Figure 4.9: Calculating Force Limit from Pneumatic Trail

In keeping with the original goal stated in Eq. (4.32), we would like to show that for both cases, the force errors $(\widehat{F}_{yf} - F_{yf})$ and $(\widehat{F}_{yr} - F_{yr})$ in Eq. (4.38) can be bounded by the slip angle estimation error.

Case 1:

Consider the first case in which the estimation error is nonnegative, i.e. $\widehat{\alpha}_f \geq \alpha_f$. Given the pneumatic trail estimates for the front left and right tires, $\widehat{t}_{pl}$ and $\widehat{t}_{pr}$, respectively, the algorithm algebraically solves for estimated friction limits $\frac{1}{\widehat{I}_{fl}}$ and $\frac{1}{\widehat{I}_{fr}}$ using the current estimate of front slip angle. With $\widehat{\alpha}_f \geq \alpha_f$ and Condition 3 satisfied, we see that for the front left tire

$$\frac{1}{\widehat{I}_{fl}} = \frac{t_{po} C_{\alpha fl} \left|\tan \widehat{\alpha}_f\right|}{3(t_{po} - \widehat{t}_{pl})} \tag{4.39}$$

$$\geq \frac{t_{po} C_{\alpha fl} \left|\tan \alpha_f\right|}{3(t_{po} - t_{pl})} = \frac{1}{I_{fl}}. \tag{4.40}$$

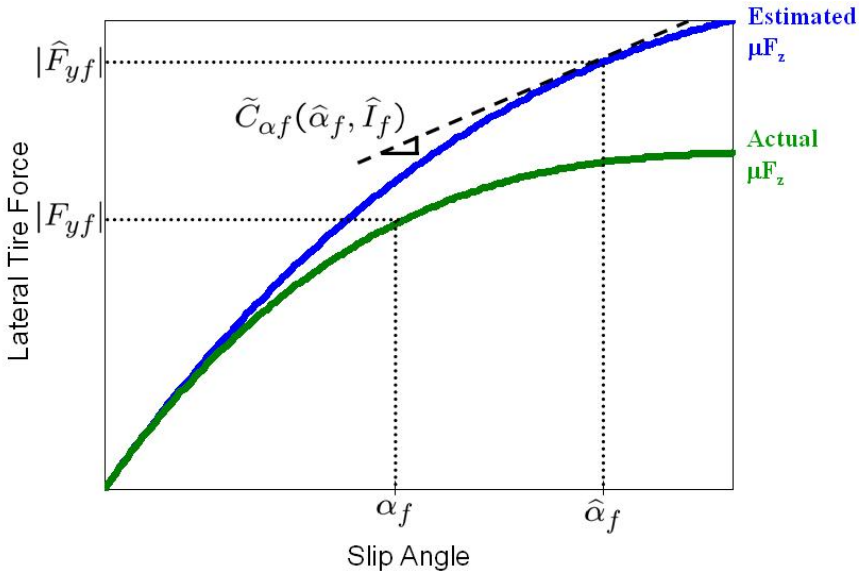

Figure 4.10: Bounding lateral force error when $\widehat{\alpha}_f \geq \alpha_f$

That is, an overestimated slip angle yields an overestimated friction limit. This effect is illustrated graphically in Fig. 4.9 with $\alpha_f = \alpha_1$ and $\widehat{\alpha}_f = \alpha_2$ (and $\widehat{t}_p = t_p$ for illustration purposes). Similarly, the friction limit is overestimated for the front right tire. This results in a lateral axle force estimate $\widehat{F}_{yf}$ which is negative and larger in magnitude than the actual force (recalling that positive slip angle produces negative lateral force).

Now, the error in Eq. 4.38 can be bounded by

$$\begin{aligned} \dot{e}_\alpha \quad \leq \quad & -K_f \widetilde{C}_{\alpha f}(\widehat{\alpha}_f, \widehat{I}_f)(\widehat{\alpha}_f - \alpha_f) - (K_r + K)\widetilde{C}_{\alpha r}(\widehat{\alpha}_r, \widehat{I}_r)(\widehat{\alpha}_r - \alpha_r) \\ & + K\Delta F_y. \end{aligned} \tag{4.41}$$

The upper bound in Eq. (4.41) follows from nature of Fiala tire model. The modeled tire curve to be not only Lipshitz continuous, but as slip angle increases, the magnitude of the local first derivative (e.g. local cornering stiffness) also decreases. Because $\widehat{\alpha}_f \geq \alpha_f$, extrapolating the local stiffness at $\widehat{\alpha}_f$ for the front axle provides a bound for the error in the force estimate (the magnitude of the estimated force error

is always less than $\widetilde{C}_{\alpha f}$ multiplied by the slip angle error). This bound is admittedly conservative, yet can be easily understood from Fig. 4.10. A similar bound is derived for the rear axle lateral force error using the rear local cornering stiffness $\widetilde{C}_{\alpha r}$.

Recalling that the rear slip angle is kinematically linked to the front slip angle by Eq. (4.4), we see that rear slip angle error is in fact equivalent to front slip angle error

$$\widehat{\alpha}_r - \alpha_r = \widehat{\alpha}_f - \alpha_f \tag{4.42}$$

and Eq. (4.41) can be further simplified to be

$$\dot{e}_\alpha \;\leq\; -\left[K_f \widetilde{C}_{\alpha f}(\widehat{\alpha}_f, \widehat{I}_f) + (K_r + K)\widetilde{C}_{\alpha r}(\widehat{\alpha}_r, \widehat{I}_r)\right] e_\alpha + K\Delta F_y. \tag{4.43}$$

Case 2:

The second case considers a negative estimation error. Now with $\widehat{\alpha}_f < \alpha_f$, the observer *underestimates* the friction limit for the front left and right tires using Eq. (4.17), an effect shown in Fig. 4.9 (here, $\widehat{\alpha}_f = \alpha_1$ and $\alpha_f = \alpha_2$). This produces a lateral axle force estimate $\widehat{F}_{yf}$ which smaller in magnitude than the actual force, illustrated in Fig. 4.11. Now, the error dynamics are:

$$\dot{e}_\alpha \;\leq\; -\left[K_f \widetilde{C}_{\alpha f}(\alpha_f, \widehat{I}_f) + (K_r + K)\widetilde{C}_{\alpha r}(\alpha_r, \widehat{I}_r)\right] e_\alpha + K\Delta F_y \tag{4.44}$$

Note that in order to use the local stiffness to bound the force residual for either case, we must use the smaller local stiffnesses $\widetilde{C}_{\alpha f}(\alpha_f, \widehat{I}_f)$ and $\widetilde{C}_{\alpha r}(\alpha_r, \widehat{I}_r)$ corresponding to the larger slip angle.

Putting the two cases together, we have nearly satisfied the desired error dynamics for stability. The slip angle error dynamics are:

$$\dot{e}_\alpha \;\leq\; -\gamma e_\alpha + K\Delta F_y \tag{4.45}$$

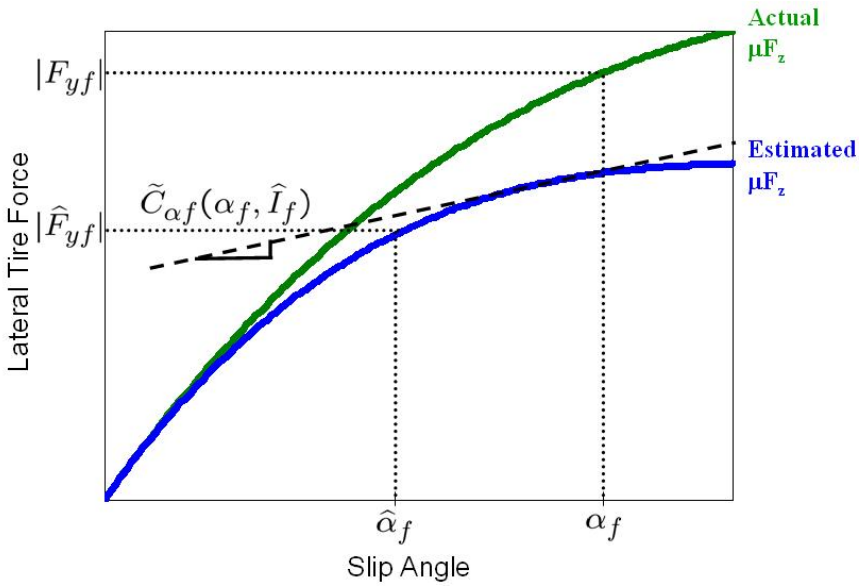

Figure 4.11: Bounding lateral force error when $\widehat{\alpha}_f < \alpha_f$

where

$$\begin{aligned} \gamma &= K_f \widetilde{C}_{\alpha f} + (K_r + K)\widetilde{C}_{\alpha r} \\ \widetilde{C}_{\alpha f} &= -\frac{dF_{yf}}{d\alpha_f}\bigg|_{(\max\{\alpha_f, \widehat{\alpha}_f\}, \widehat{I}_f)} \\ \widetilde{C}_{\alpha r} &= -\frac{dF_{yr}}{d\alpha_r}\bigg|_{(\max\{\alpha_r, \widehat{\alpha}_r\}, \widehat{I}_r)} \end{aligned}$$

Now, because Condition 2 ensures that γ is a real, positive number, the slip angle estimation error is simply bounded by the the uncertainty in lateral force ΔF_y from the error dynamics equation in Eq. (4.45):

$$|e_\alpha| \leq \frac{K\Delta F_y}{\gamma} = \frac{K\Delta F_y}{K_f \widetilde{C}_{\alpha f} + (K_r + K)\widetilde{C}_{\alpha r}} \tag{4.46}$$

In the special case where we have perfect knowledge of lateral force ($\Delta F_y = 0$), asymptotic stability of the observer can be guaranteed. To prove this, let $V(e_\alpha) = \frac{1}{2}e_\alpha^2$

be a candidate Lyapunov function. Then,

$$\dot{V}(e_\alpha) = e_\alpha \dot{e}_\alpha \tag{4.47}$$

$$\leq -\gamma e_\alpha^2 \tag{4.48}$$

So $-\dot{V}(e_\alpha)$ is greater than a positive definite function, which implies asymptotic stability and guarantees $\widehat{\alpha}_f \to \alpha_f$ (and $\widehat{\alpha}_r \to \alpha_r$) as $t \to \infty$.

4.4.2 Stability Proof Remarks

Remarks on Condition 2

Condition 2 arises from the fact that we require that $\gamma > 0$ in Eq. (4.45) in order to ensure that the slip angle error is bounded. The first implication of this condition is that the observer is stable if either the front *or* rear axle forces have reached their peaks, but not both. From an estimation standpoint, this fundamentally makes sense. For example, one could imagine that immediately after the vehicle loses lateral traction, sideslip angle grows from a relatively small angle to a larger angle corresponding to a full skid, all of which occurs under saturated front and rear lateral forces.

Although the slip angles are unobservable during situations of complete loss of lateral traction, the larger aim of this work is to incorporate the nonlinear observer into a stability control scheme. Fortunately, once the vehicle is in a full sideways skid, regardless of the magnitude of the tire slip angles, the control aim is unambiguous – the controller should utilize available actuators to reduce slip angle and counteract the skid.

Condition 2 conveniently provides a minimum value for the observer feedback gain as a function of vehicle speed. Furthermore, Eq. (4.45) suggests that the effect of gain K on the estimation convergence rate is most dominant when the front tires have saturated, and is least significant when the front tires retain lateral traction, an effect that has been confirmed experimentally.

Remarks on Condition 3

In the linear handling region (when the lateral force can be well approximated by $F_y = -C_\alpha \alpha$), it can be shown that the observer is stable regardless of the accuracy of pneumatic trail. Once the actual lateral forces enter the nonlinear region, we may derive the required accuracy of our knowledge of pneumatic trail, which is stated in Condition 3. In the discussion that follows, we consider the linear and nonlinear regimes separately. We also assume $\widehat{\alpha}_f > \alpha_f$, yet a similar argument can be made when $\widehat{\alpha}_f < \alpha_f$.

Linear Handling Region

If the estimated lateral forces $\widehat{F}_{yf}$ and $\widehat{F}_{yr}$ are well approximated by a linear tire model (they also satisfy Eqs. (4.26)-(4.27)), then we can write the slip angle error dynamics from Eq. (4.38) as

$$\dot{e}_\alpha = -\left[K_f C_{\alpha f} + (K_r + K) C_{\alpha r}\right] e_\alpha + K \Delta F_y \tag{4.49}$$

where the lateral force residuals are bounded by their linear cornering stiffnesses, which are indeed independent from the pneumatic trail estimate.

Even when $\widehat{F}_{yf}$ and $\widehat{F}_{yr}$ are nonlinear, the observer is guaranteed stable even with an imperfect pneumatic trail measurement. In this situation, which is illustrated in Fig. 4.12, we can use the local cornering stiffnesses to arrive at the same bound as before in Eq. (4.45). Naturally, the observer obtains faster estimation convergence with a more accurate estimate of the friction limits. However, regardless of the accuracy of pneumatic trail, the observer is always stable and the error is bounded when the actual lateral forces are in the linear region.

Nonlinear Handling Region

If the actual lateral forces generated at the tires are in the nonlinear region of operation, then we require a certain level of accuracy of our pneumatic trail information for observer stability. In order to use the local cornering stiffness as a valid bound on the slip angle estimation error, an overestimated (underestimated) slip angle must

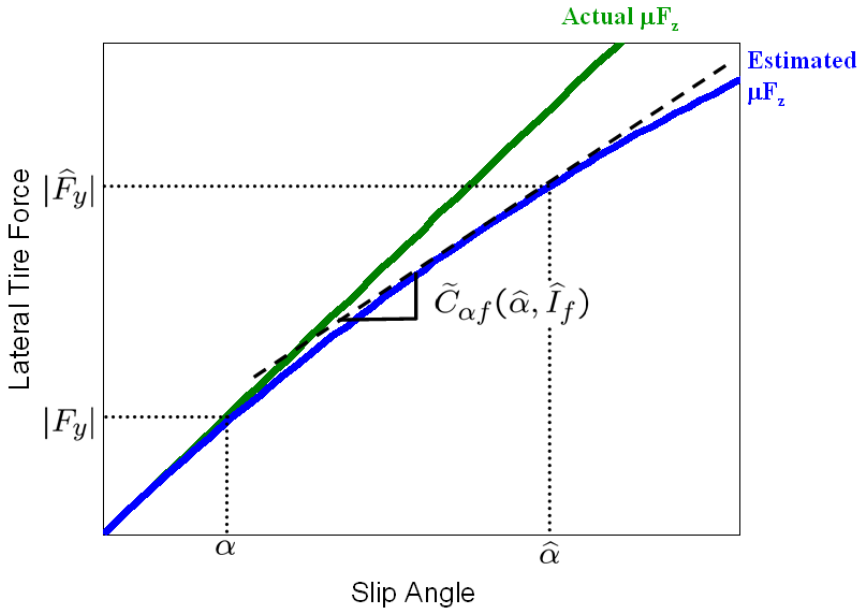

Figure 4.12: Bounding lateral force error when only F_y is in linear region of handling

produce an overestimated (underestimated) friction limit, shown in Fig. 4.9. Thus, for either tire, the slip angle error dynamics are stable and bounded if

$$\left|\widehat{t}_p - t_p\right| \;<\; \frac{t_{po} C_{\alpha f} I_f}{3} \left|\tan \widehat{\alpha}_f - \tan \alpha_f\right|. \tag{4.50}$$

Approximating for small angles and substituting the error bound from Eq. (4.45), we have:

$$\left|\widehat{t}_p - t_p\right| \;<\; \frac{t_{po} C_{\alpha f} I_f}{3} \frac{K \Delta F_y}{\gamma}. \tag{4.51}$$

Conceptually, this condition states that the observer requires pneumatic trail information that is more accurate than its estimate of front slip angle. This is reasonable since pneumatic trail is a measurement to adjust the tire curve properties used to update the front slip angle estimate. Moreover, the bounds on the accuracy of pneumatic trail for the stability of the observer confirms what we know physically to be true. When the vehicle is turning, the observer has more accurate knowledge of pneumatic

trail and peak force, enabling it to dynamically adjust its slip angle based on the estimated limits of tire adhesion. However, when the vehicle is driven nearly straight, the observer's knowledge of pneumatic trail is expected to be imprecise. During this region of handling, the observer algorithm's estimate of slip angle only depends on the tire cornering stiffness and is unaffected by the friction limits.

The most stringent condition on our accuracy of pneumatic trail information is when both tires have just exited the linear region on a high friction surface. As the local cornering stiffnesses decrease (as forces transition to saturation region), or as the friction coefficient or tire normal load decreases, the allowable error for stability increases. Thus, the observer requires less precise knowledge of pneumatic trail when the vehicle is driving on a slippery surface, or on the inside tire during a turn, both of which are important situations that require tire parameter knowledge.

4.5 Validation of Pneumatic Trail Nonlinear Observer

4.5.1 Simulation

In order to validate the observer algorithm, this section applies the estimation technique to a simulated vehicle. The simulation model encompasses the following:

- The vehicle is represented by a single-track, 2-state planar model with a constant longitudinal speed and no longitudinal forces, a model commonly known as the bicycle model (see Fig. 4.2). Equations (4.1)-(4.2) give the equations of motion for the system. The bicycle model parameters are chosen to emulate the handling characteristics of P1, the steer-by-wire experimental testbed pictured in Fig. 2.5.

- A 5 Hz low-pass filter is applied to the actuated steer angle to approximate the bandwidth of P1's steering system.

- Front and rear tire lateral tire forces are represented by the nonlinear Fiala tire model in Eq. (2.9). The tires forces are calculated individually first, and

then the left/right tires are summed together to form the axle tire forces in the equations of motion.

- The effects of lateral weight transfer are included using the model introduced in Section 2.3.4.

Although the simulation assumes perfect measurements are available to the observer, the tire normal loads resulting from the lateral weight transfer dynamics are unknown to the estimation process. The simulation is coded in MATLAB, and the observer outputs real-time estimates of the lateral peak force limits (and therefore the tire-road friction) and front and rear slip angles.

The maneuver presented here is a simulated 0.5 Hz slalom, driven at a constant speed of 10 m/s on a moderate-friction surface. The time history of the maneuver is presented in Fig. 4.13(a). The tire-road friction coefficient is set to be $\mu = 0.5$, which represents a surface similar to wet pavement. A slalom maneuver is chosen to demonstrate the speed of the observer's response during a rapidly changing steering command. As shown in the Fig. 4.13(b), the resulting front axle tire forces enter into the nonlinear handling regime.

Figure 4.14(a) illustrates the accuracy of the friction estimate and the slip angle results for the front and rear axles. The friction coefficient of $\mu = 0.5$ is properly identified and the slip angle estimates match well with truth. The pneumatic-trail based observer is able to identify the friction at 0.2g of lateral acceleration, or 40% of the peak achievable force on this low friction surface.

The slight, but noticeable variation of the friction estimate is worth further explanation. The deviation from $\mu = 0.5$ is due to the fact that as the steering torque (and therefore total aligning moment) of the front axle approaches zero during the slalom, the estimated pneumatic trail approaches zero. However, because the slip angle estimate slightly lags the actual slip angle, the slip angle estimation error is as high as 0.1° for this particular maneuver, shown in Fig. 4.14(b). From Eq. (4.17), we see that when the front slip angle magnitude is near zero, any slip angle error has a greater effect on the peak force estimate (and therefore the friction estimate). This mathematical observation agrees with our physical intuition. When the vehicle is

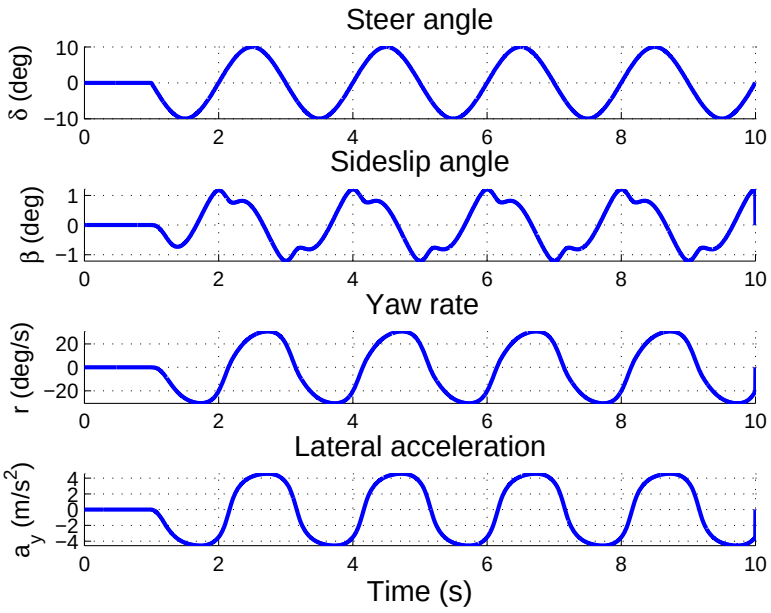

(a) Maneuver Time History

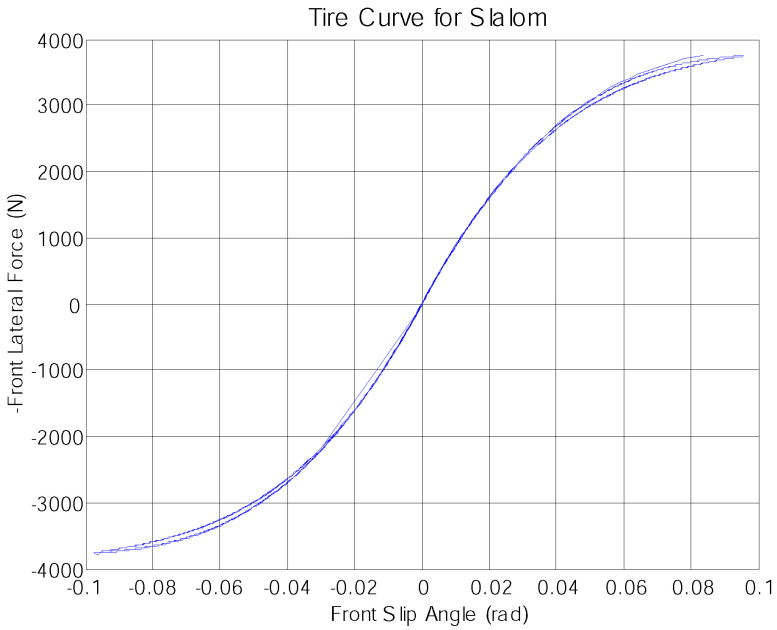

(b) Front Axle Tire Curve

Figure 4.13: Simulated Slalom at 10 m/s on $\mu = 0.5$ Road

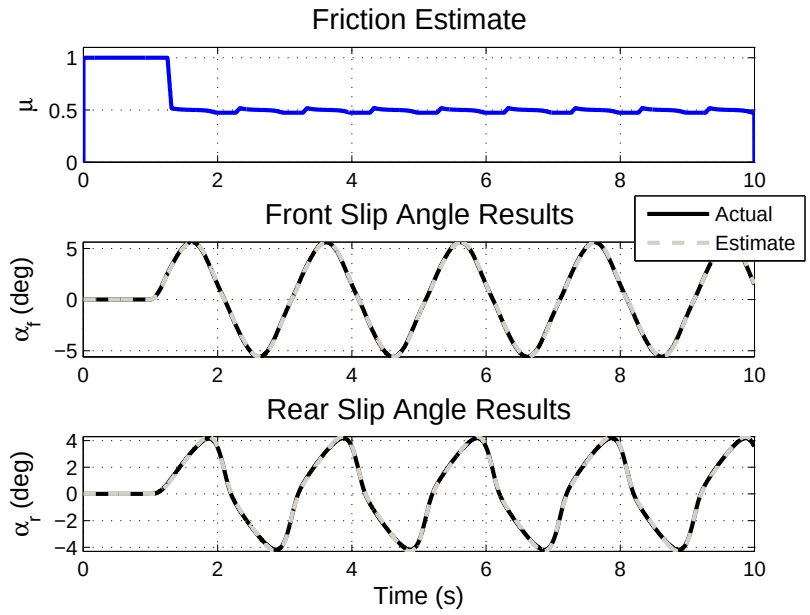

(a) Slip Angle and Friction Estimates

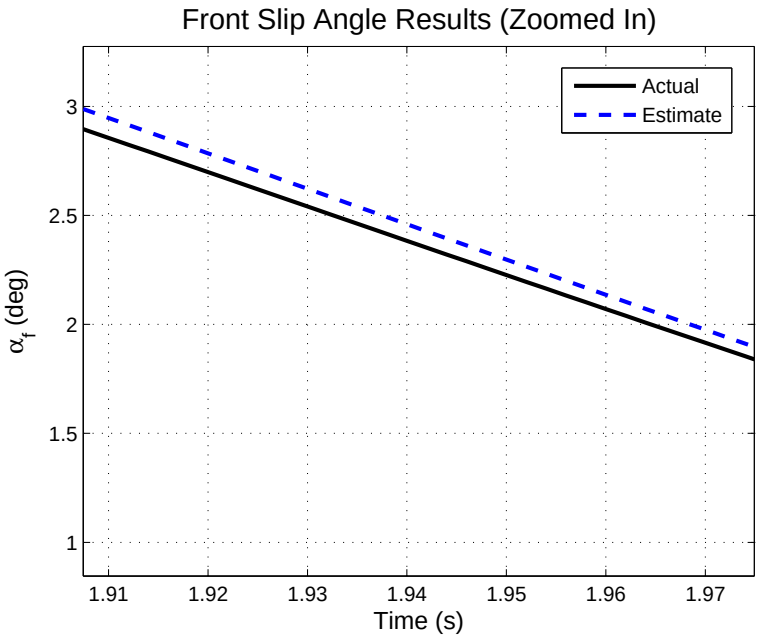

(b) Front Slip Angle Results (Zoomed In)

Figure 4.14: Simulated Slalom Estimation Results

traveling nearly straight, friction cannot be identified confidently. Furthermore, this observation gives insight to how the observer is expected to perform in experiment, where estimation and modeling errors are expected.

4.5.2 Linear Sideslip Observer

For a basis of comparison for the experimental performance of the observer presented in the next section, its slip angle estimates are compared with a purely linear observer which assumes a linear tire model ($F_y = -C_\alpha \alpha$). The following feedback observer follows the formulation proposed by Rock et al [48].

Using the bicycle model in Fig. 4.2, we assume here that the front and rear lateral forces are linear functions of slip angle (i.e. $F_{yf} = -C_{\alpha f}\alpha_f$ and $F_{yr} = -C_{\alpha r}\alpha_r$). Assuming small angle approximations, the equations of motion for the vehicle become linear functions of the states and can be written in state space form as:

$$\dot{x} = Ax + B\delta \tag{4.52}$$

where

$$x = \begin{bmatrix} \beta \\ r \end{bmatrix} \quad A = \begin{bmatrix} -\frac{c_o}{mV_x} & -(\frac{c_1}{mV_x{}^2} + 1) \\ -\frac{c_1}{I_z} & -\frac{c_2}{I_z V_x} \end{bmatrix} \quad B = \begin{bmatrix} \frac{C_{\alpha f}}{mV_x} \\ \frac{aC_{\alpha f}}{I_z} \end{bmatrix}$$

and

$$\begin{aligned} c_o &= C_{\alpha f} + C_{\alpha r} \\ c_1 &= aC_{\alpha f} - bC_{\alpha r} \\ c_2 &= a^2 C_{\alpha f} + b^2 C_{\alpha r}. \end{aligned}$$

The vehicle's onboard INS unit provides the feedback measurements of yaw rate r and the lateral acceleration a_y. Assuming knowledge of the longitudinal velocity, the relation:

$$a_y = V_x(\dot{\beta} + r) \tag{4.53}$$

allows the measurements from the system, y, to be expressed as a linear combination

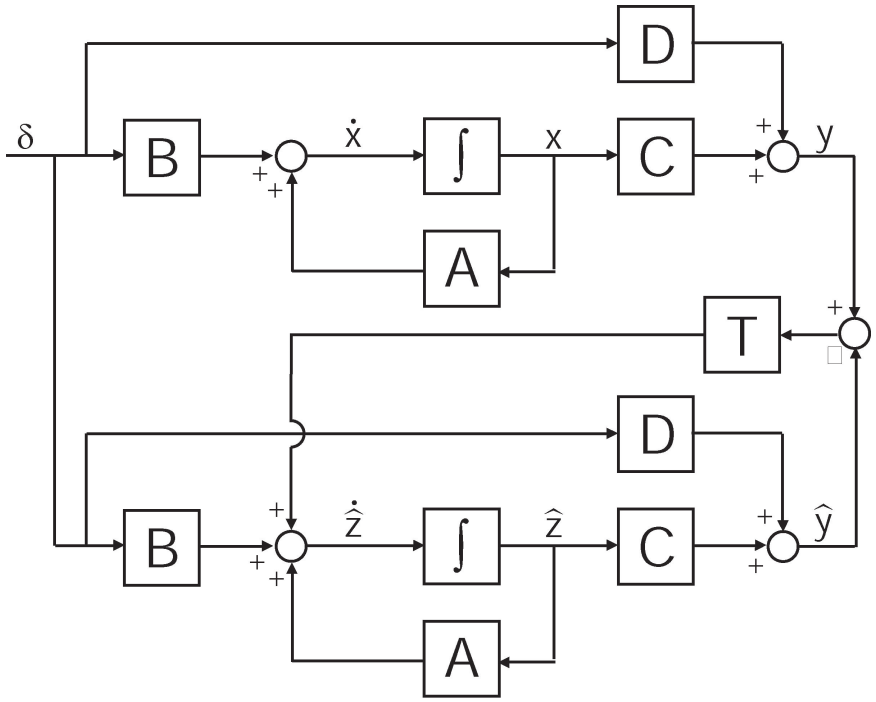

Figure 4.15: Linear Sideslip Feedback Observer Structure

of the vehicle states, x, and the input, δ:

$$y = Cx + D\delta \tag{4.54}$$

where

$$y = \begin{bmatrix} a_y \\ r \end{bmatrix} \quad C = \begin{bmatrix} -\frac{c_o}{m} & -\frac{c_1}{mV_x} \\ 0 & 1 \end{bmatrix} \quad D = \begin{bmatrix} \frac{C_{\alpha f}}{m} \\ 0 \end{bmatrix}$$

In general, the sideslip angle β in the system described by Eq. (4.52) is unobservable when the yaw rate, r, is the only measurement and the vehicle approaches neutral steering. By adding the measurement of lateral acceleration, a_y, the sideslip angle becomes observable.

Linear Observer Design

An observer to estimate sideslip from the available measurements of yaw rate and lateral acceleration can now be constructed. To do this, a simple linear observer is used in the form of Fig. 4.15 where

$$\dot{\hat{z}} = A\hat{z} + B\delta + T(y - \hat{y}) \tag{4.55}$$

$$\hat{y} = C\hat{z} + D\delta \tag{4.56}$$

where $\hat{z}$ is the estimate of the unknown states, x, and $\hat{y}$ is the estimate of the measurement vector, y. The observer feedback matrix, T, is computed such that the error dynamics, $\dot{\hat{z}} - \dot{x}$, are stable. Equation (4.55) can be written more compactly as:

$$\dot{\hat{z}} = A_{obs}\hat{z} + B_{obs}u \tag{4.57}$$

where

$$A_{obs} = [A - TC] \quad B_{obs} = \begin{bmatrix} B - TD & T \end{bmatrix} \quad u = \begin{bmatrix} \delta \\ y \end{bmatrix}$$

The standard bicycle model assumes a constant velocity in the longitudinal direction, which is not a valid assumption in general. Hence, the observer feedback matrix, T, is computed for an approximate speed, and the matrices A_{obs} and B_{obs} are computed at each time step with the current velocity information. This velocity information would normally come from GPS, which is assumed to be unavailable. However, there are other sources of approximate velocity information. For instance, this information could be used from the vehicle's CAN system. While this information is not as accurate as the velocity information received from GPS, it is generally close enough to use for the purpose of generating the observer matrices, A_{obs} and B_{obs}.

Table 4.1: Experimental Observer Test Matrix

Experimental Test	**Test Surface**	**Purpose**
1. Slalom	Dry pavement ($\mu = 1$)	Investigate the lag involved with the observer
2. Ramp	Dry pavement ($\mu = 1$)	Determine the response of the observer during tire force saturation
3. Sharp transient turns	Loose gravel on asphalt ($\mu = 0.5-0.7$)	Investigate sensitivity to unmodeled effects and a moderate-friction surface
4. Ramp	Loose gravel on asphalt ($\mu = 0.5-0.7$)	Validate the early friction detection capability of observer on moderate-friction surface

4.5.3 Experiments

To validate the 'Pneumatic Trail Nonlinear Observer' in experiment, a set of test maneuvers were performed on the research vehicle P1 (see Section 3.2.2). Four representative maneuvers are selected to demonstrate the observer's performance during a variety of maneuvers and driving conditions. Table 4.1 describes the testing conditions and the investigative purpose of each maneuver. As the table illustrates, vehicle test runs were conducted on two types of surfaces: dry pavement and loose gravel on asphalt. On pavement, the tires achieve a friction coefficient of about $\mu = 1$. By comparison, due to its uneven gravel distribution, loose gravel has a friction value ranging from $\mu = 0.5$ to 0.7. Both testing surfaces are flat. Moffett Federal Airfield, a local site for dry pavement testing, is pictured in Fig. 4.16(a), while the Shoreline gravel testing lot is shown in Fig. 4.16(b).

(a) Pavement Surface (Moffett Federal Airfield)

(b) Gravel Surface (Shoreline Testing Lot)

Figure 4.16: Experimental Proving Grounds

Pavement Experimental Results

Ramp Steer

First, a quasi-steady-state ramp steer is performed on P1, a maneuver first introduced in Fig. 2.12 in Section 2.4.2. Driven at a constant speed of 10 m/s, this maneuver achieves full lateral force saturation of the front tires (see Fig. 4.17(a)). Using the estimation algorithm outlined in this chapter, the resulting friction and slip angle estimates are shown in Fig. 4.17(b). The friction estimate holds steadily at $\mu = 1$, which agrees with skidpad testing. At $t = 6.5\,\text{s}$, the vehicle travels over a slippery metal grate, which prompts the friction estimate to correctly decrease. Note that that the tire-road friction is predicted when vehicle has achieved only 50% of its peak lateral force.

The front and rear slip angle estimates are compared with GPS-based measurements, which are taken as truth [49], and with the linear slip angle feedback observer which assumes $F_y = -C_\alpha \alpha$ and uses lateral acceleration and yaw rate as measurements [48]. In the linear region of handling, as expected, both observers match well with GPS-based measurements. However, after the vehicle enters nonlinear region of handling (after $t = 6\,\text{s}$), the limitations of a linear sideslip estimator are clearly evident as large errors begin to develop. Meanwhile, the slip angle estimates for the pneumatic trail-based estimator are comparable to those from GPS well into the nonlinear region of handling. This demonstrates that the simple total aligning moment model proposed in this work has reasonable correspondence to experiment. After $t = 12\,\text{s}$, the front lateral tire force has fully saturated. However, the estimate is still able to track GPS-based measurements reasonably well since the rear tire forces have yet to reach full saturation (from Condition 2 in Section 4.4).

Slalom

The second maneuver presented is a slalom at a constant speed of 15 m/s which intermittently enters the nonlinear operating region of the tires (Fig. 4.18(a)). The slalom is performed via an automated steering system on P1. The slip angle estimates for this maneuver are shown in Fig. 4.18(b). Again, as expected, both estimators match well with GPS-based measurements in the linear handling region. However,

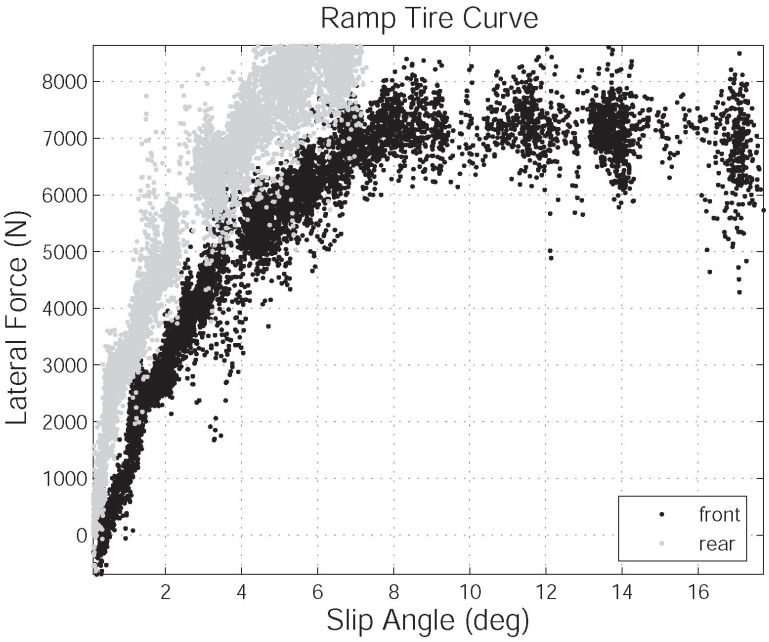

(a) Tire Curve

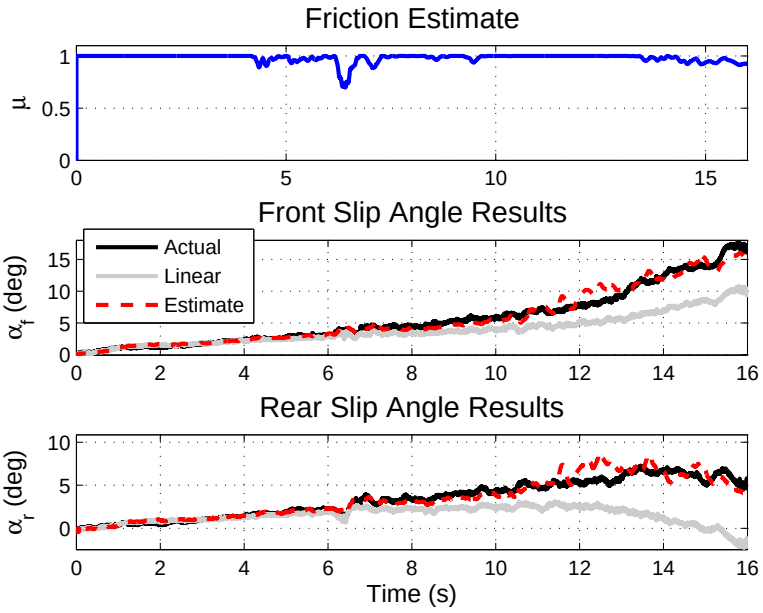

(b) Estimation Results

Figure 4.17: Experimental Ramp Steer (Pavement)

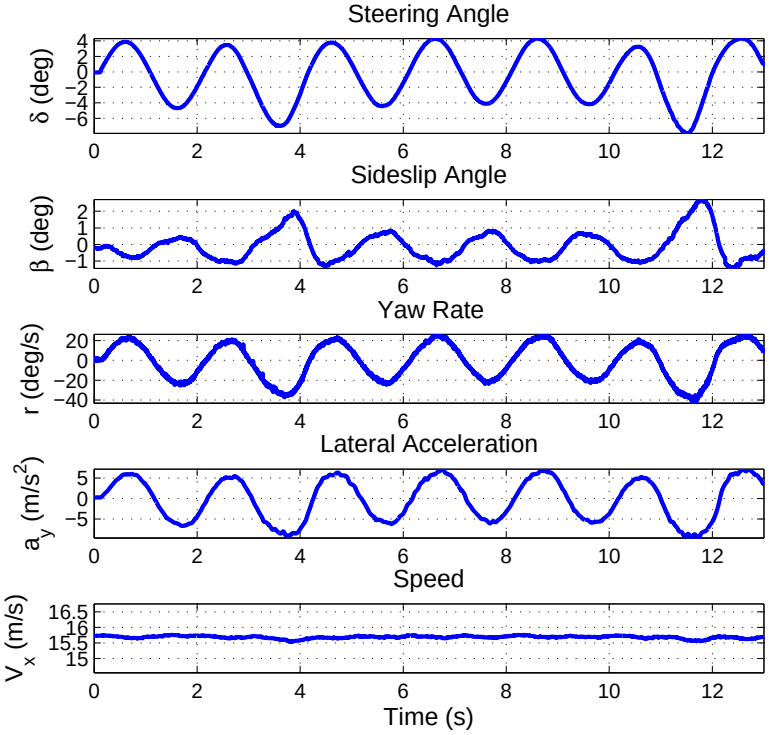

(a) Maneuver Time History

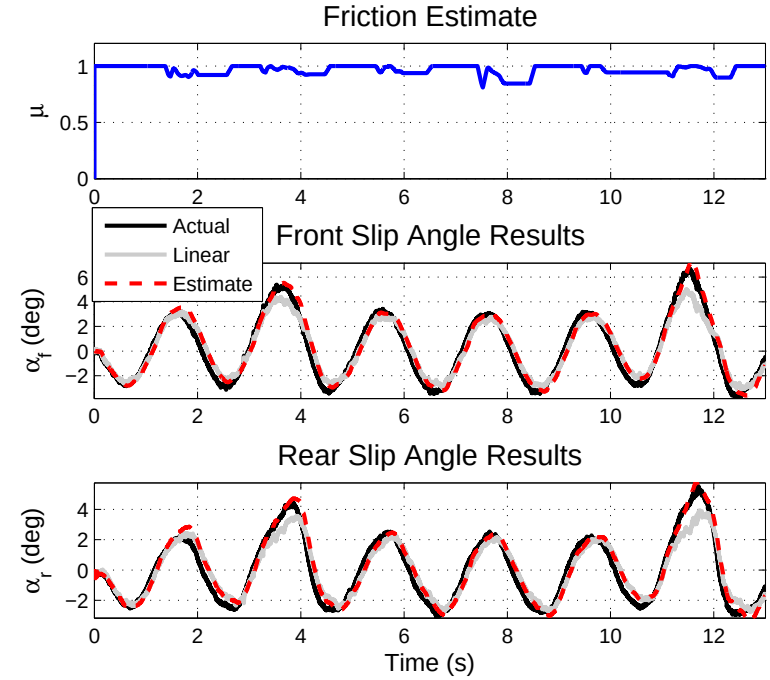

(b) Estimation Results

Figure 4.18: Experimental Slalom (Pavement)

when the vehicle enters the nonlinear handling region (near $t = 4$s and 12s), the benefit of the pneumatic trail-based estimation approach over the linear estimator is evident. The former tracks the actual slip angle better and is within the accuracy of the GPS measurement.

The friction estimate hovers around the correct value of $\mu = 1$ during the majority of the maneuver. As was seen (to a lesser degree) in the simulated slalom presented in Section 4.5.1, the slight deviation in the friction estimate during this quickly changing steering command is a function of slip angle estimation error propagating to the peak force estimate when the magnitude of front slip angle is small. Given sufficient lateral dynamics, however, the friction estimate matches well with truth.

This experimental slalom maneuver demonstrates that the speed of the observer response is adequate for accurate tire characterization during fast steering maneuvers.

Gravel Experimental Results

Sharp Transient Turns

Shown in Fig. 4.19(a), the third maneuver presented is a series of sharp transient turns performed on a loose gravel course. The steer angle commands were controlled by a lanekeeping system designed to keep the vehicle on a GPS coordinate map (see Fig. 4.20), correcting for vehicle lateral error and heading using front steering actuation [25]. It is for this reason that the steer angle command reaches the 22° steering limit. Driven at an average speed of 9 m/s, this maneuver pushes the front tires well into the saturation region.

Figure 4.19(b) illustrates the observer performance. The friction estimates hold at the nominal value of $\mu = 1$ during periods of insufficient lateral excitation, and reach a value of $\mu = 0.5$ to 0.6 when the vehicle is turning. This friction coefficient estimate on this gravel surface is quite reasonable given that the front tires are almost completely skidding.

The slip angle estimates are compared to a linear estimator. With this maneuver achieving high slip angles of up to 20° in the front tires, the nonlinear observer tracks the actual slip angle much better than the linear estimator. The variation seen in its rear slip angle estimate is likely due to the simple assumptions that available

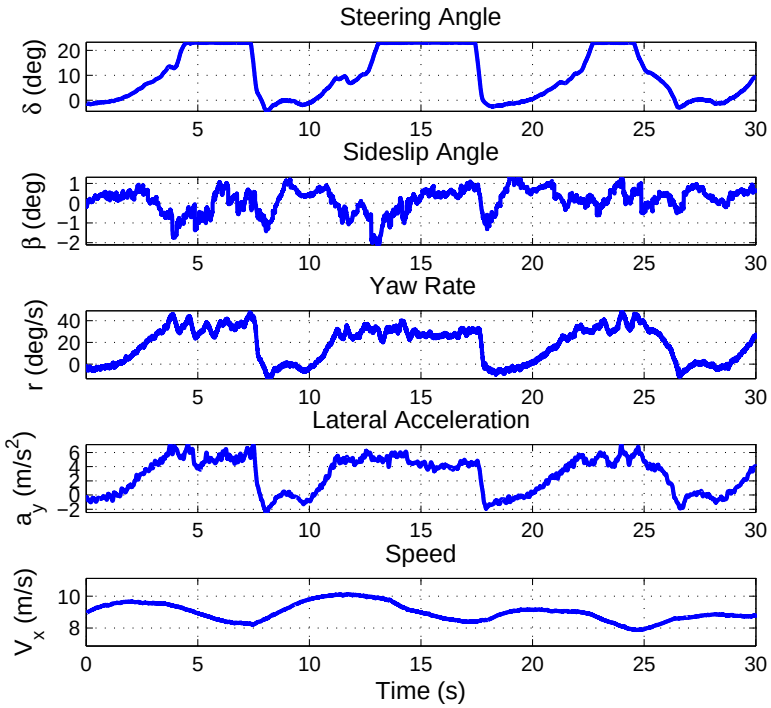

(a) Maneuver Time History

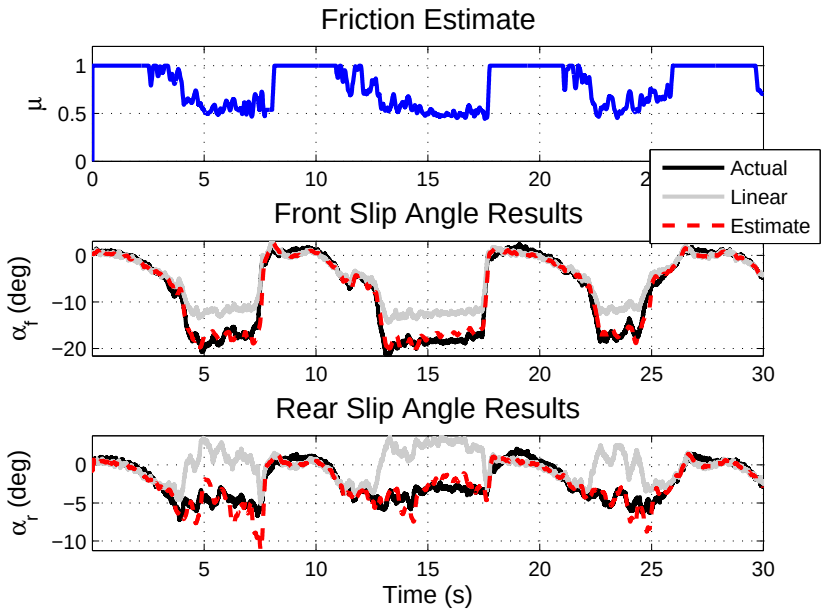

(b) Estimation Results

Figure 4.19: Experimental Transient Turns (Gravel)

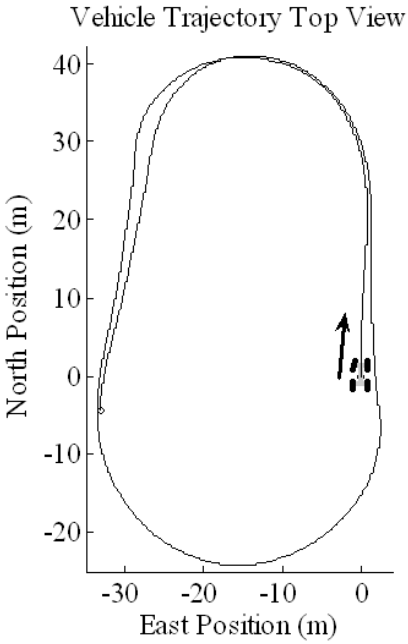

Figure 4.20: Automated Lanekeeping Path

friction on the front and rear axles are equal and that longitudinal weight transfer is negligible. In actuality, the vehicle is traveling over an unevenly distributed gravel surface with changing friction properties. The vehicle also experiences some longitudinal dynamics as the speed undulates during the maneuver. Even so, under these challenging testing conditions, the observer is able to exhibit the robustness of its slip angle and friction estimates.

Ramp Steer

The final maneuver presented is a quasi-steady state ramp steer commanded by the automatic steering system. The time history of the maneuver is shown in Fig. 4.21(a). Driven at a constant speed of 8 m/s with negligible longitudinal dynamics on loose gravel, this maneuver is ideal for exploring the early friction sensing ability of the observer on a moderate-friction surface. As illustrated in Fig. 4.21(b), estimation process is able to correctly detect friction at 0.3g of lateral acceleration, which on this surface corresponds to roughly 50% of the peak lateral force, exhibiting the predictive

properties of tire pneumatic trail for friction estimation.

Remarks on Experimental Results

We note that there is a tradeoff between early friction detection and ensuring the friction estimate is protected against slip angle estimation errors when the front slip angle magnitude is small (as exhibited by slalom maneuver in Section 4.5.3). The desire for early friction estimation would motivate setting the slip angle threshold for friction estimation low, while error in the friction estimates at small slip angles would reason to set it to be high. A compromise was found for these experimental maneuvers by setting the slip angle threshold for friction detection to be 2.5°.

All of these experimental results were obtained without relying on an accurate knowledge of vertical tire force dynamics in the estimation process, which simplifies the sensor hardware required. From successful experimental results, this method is a promising way to predict the friction limits and provide accurate estimates of slip angle up to the limits in real-time using measurements available on production vehicles.

4.6 Conclusions

This chapter presented two potential methods for obtaining the parameters sufficient to characterize lateral tire forces with only intermittent access to GPS (or without GPS entirely assuming cornering stiffness information is available). Both methods utilized a nonlinear slip angle observer to obtain estimates of tire slip angle in the absence of GPS-based measurements. To estimate the peak friction limits, the first method solved the cubic model of total aligning moment. However, due to unstable error properties when using total aligning moment in the overall observer, it was shown that errors in slip angle can result in estimation divergence.

The second method, referred to as 'Pneumatic Trail Nonlinear Observer', used pneumatic trail estimates to determine the friction limits. Not only is pneumatic trail is a valuable source of information for lateral tire characterization by enabling early detection of the limits before they are reached, it has stable error properties

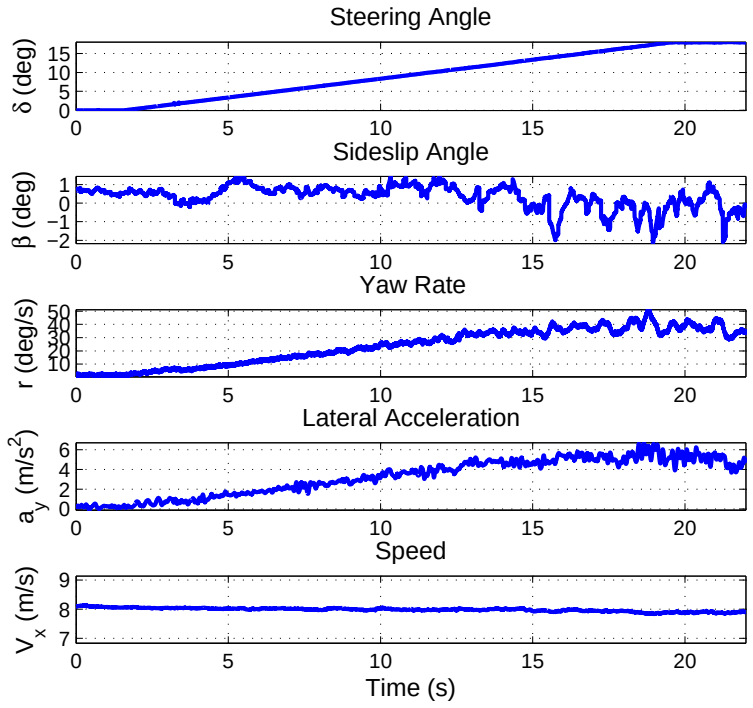

(a) Maneuver Time History

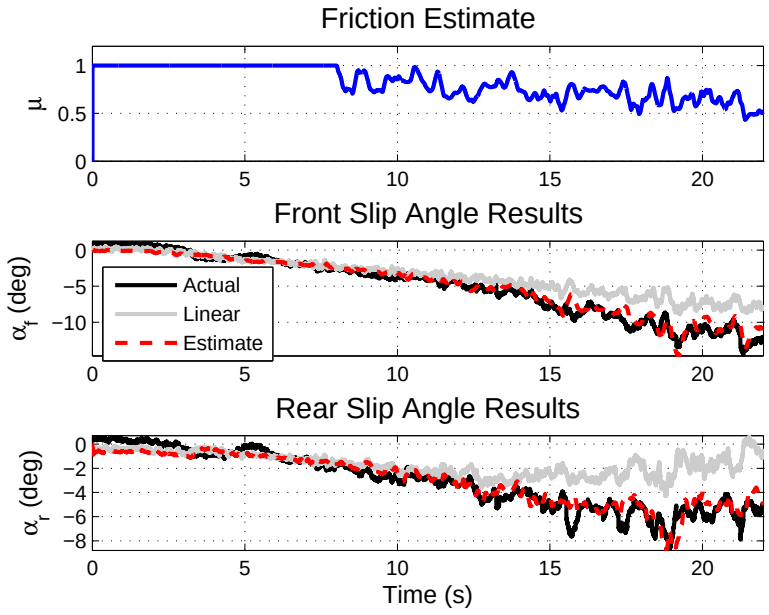

(b) Estimation Results

Figure 4.21: Experimental Ramp (Gravel)

when combined with the nonlinear slip angle observer. Experimental results on two friction surfaces demonstrated that the limits of handling can be predicted once the tires have utilized only 50% of their maximum lateral force. In other words, this method has shown that friction limit detection is possible before the tires have exited the linear handling regime.

In addition, the 'Pneumatic Trail Nonlinear Observer' could be integrated into a GPS-equipped vehicle in which GPS-based estimation algorithms are used when a signal is available, such as the ones introduced in Chapter 3. During periods of signal loss, the 'Pneumatic Trail Nonlinear Observer' enables accurate tire force characterization up to the limits of handling.

Finally, this chapter demonstrated the potential of actuators being used as virtual sensors. Given the front steering actuation system of the steer-by-wire vehicle considered in this study, direct estimation of the front tire peak force is attainable from steering torque measurements. For future work, the overall observer performance could be improved on P1 with the installation of rear axle load-cell sensors, which would enable direct sensing of the rear tire friction limits. Future work on P1 could also incorporate longitudinal tire forces and dynamics in the estimation models to enable accurate estimation when the car is braking or accelerating. Finally, a four wheel steering vehicle could provide the information necessary to directly determine the peak force of each individual tire (removing the need to model or estimate normal load dynamics).

Chapter 5

Envelope Control using Front Steering

5.1 Introduction

Envelope protection is a control strategy in aviation that aims to prevent the aircraft from entering state or control regions outside of the safe flight regime. Limitations are often imposed on an aircraft's state, such as angle of attack, airspeed, bank angle and altitude. While envelope protection is well-known in aviation and in fact are on many modern military and commercial aircraft [65], previous work on applying this control strategy to production passenger vehicles is somewhat limited.

Current applications of envelope control on vehicles are reactive: they can only intervene after the limits have been exceeded. Applications of longitudinal envelope control include ABS and TCS, which attempt to keep the vehicle's tires within their longitudinal limits of adhesion to avoid wheel lock and wheel spinout after drastic changes in wheel speed are detected. Lateral envelope control systems such as ESC place limits on deviations from the driver's intended yaw rate command. They operate with incomplete information of the vehicle's state and lateral force limits [34, 63]. As a result, they can only control quantities that are be directly measured or estimated reliably, such as yaw rate and sideslip rate (not sideslip angle), and do not have early knowledge of tire-road friction coefficient.

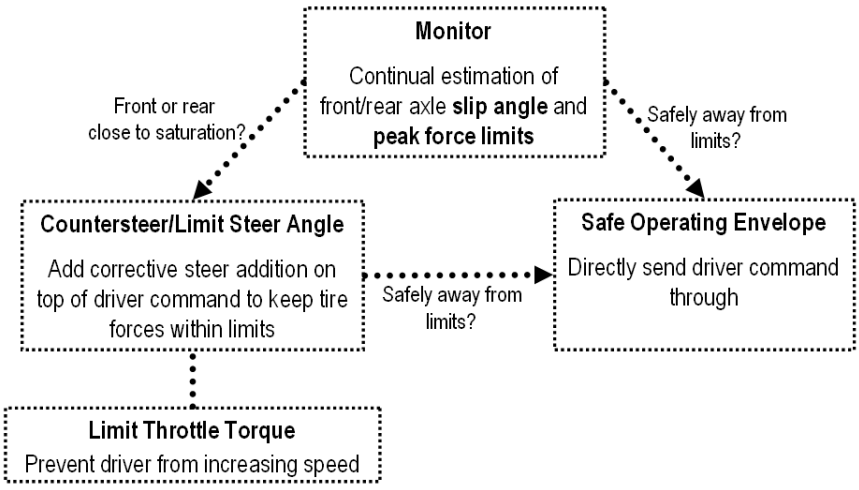

Figure 5.1: Envelope Control Strategy

Chapter 4 introduced a method for predicting the vehicle's lateral handling capability using sensors available on production vehicles. The method is based on tire pneumatic trail, the distance between the effective lateral force vector and the center of the contact patch (see Fig. 2.1). Using pneumatic trail for lateral limit estimation is advantageous for two reasons. First, it provides early warning of approaching lateral force limits even before lateral forces saturate (Fig. 2.4). Second, it can be extracted from steering torque measurements which are available on vehicles with steer-by-wire, EPS, or Active Steering systems. Utilizing pneumatic trail, we constructed a nonlinear observer for estimating tire slip angle and the peak lateral force limits (and the tire-road coefficient of friction if normal force is known). This observer is mathematically guaranteed to converge in the presence of estimation error and has been validated experimentally.

This chapter introduces a simple envelope control strategy that is inspired by a desirable driver response using steering to control front and rear cornering forces. The controller utilizes the early information of a vehicle's lateral limits provided by the nonlinear observer developed in Chapter 4. As shown in Fig. 5.1, during normal driving, the driver is able to freely maneuver the vehicle. However, if there is danger of crossing the limits, a feedback controller engages, assisting the driver with staying

within the lateral bounds using front steering actuation. The control strategy prioritizes rear tire saturation over front saturation for driver safety and vehicle stability. Moreover, the combined observer and controller system is demonstrated to stabilize the vehicle motion for a variety of maneuvers in simulation and experiment.

5.2 Envelope Control Design

During everyday driving situations, normal drivers usually operate the vehicle well within the physical limit of adhesion of the tires. Thus, their driving experience is usually limited to situations where the vehicle responds predictably to the driver's steering command. However, as the vehicle approaches its handling limits, for example during an evasive emergency maneuver or when driving on slick roads, the vehicle tends to respond less predictably to the driver's inputs. If the front tires saturate first, the vehicle is said to limit understeer and may plow out of the curve. This case is illustrated in Fig. 5.2 where the vehicle is represented with the left and right tires lumped together. If the rear tires saturate first, the vehicle limit oversteers and may spin out (shown in Fig. 5.3). Particularly from the perspective of safety, limit oversteering can present the driver with a very dangerous loss of control situation, as statistics compiled by the German Association of Insurance Companies show that severe accidents typically arise from spin outs [29].

Because the average driver is not accustomed to operating near the limits of adhesion, both limit understeering and oversteering responses are potentially quite dangerous. In fact, Förster has analyzed driver's reactions to these situations and came to two important conclusions [17]. First, the average driver is unable to judge the coefficient of friction between the tires and the road and has little knowledge of the grip reserve of the tires. Second, if the limits of tire grip are reached, the driver is usually caught by surprise and very often panics and reacts in the wrong way by steering too much. As a result, a well thought out reaction of the driver cannot be expected. Actively compensating for these effects can enable the driver to maneuver up to the handling limits safely without loss of control.

In the case of front tire saturation, a desirable steering response is to limit the

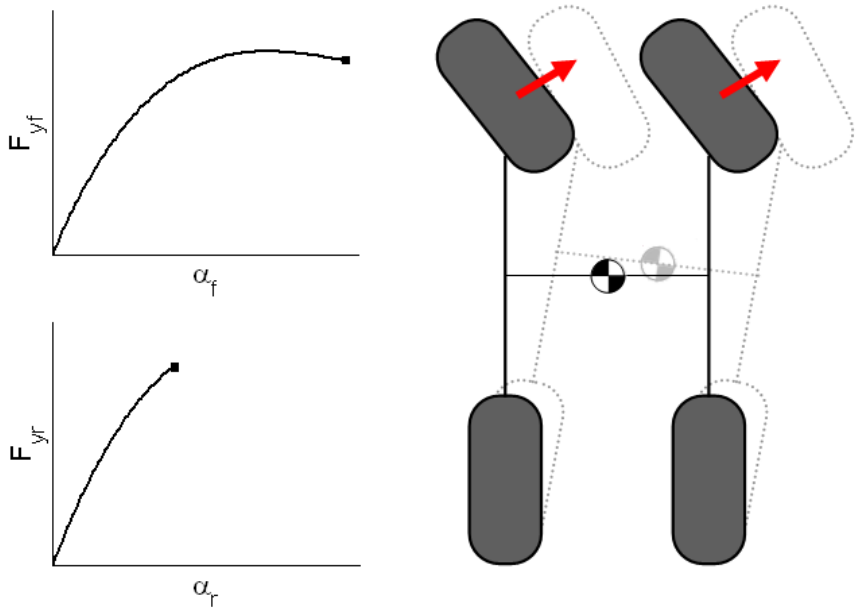

Figure 5.2: Limit Understeering: Front Axle Saturation

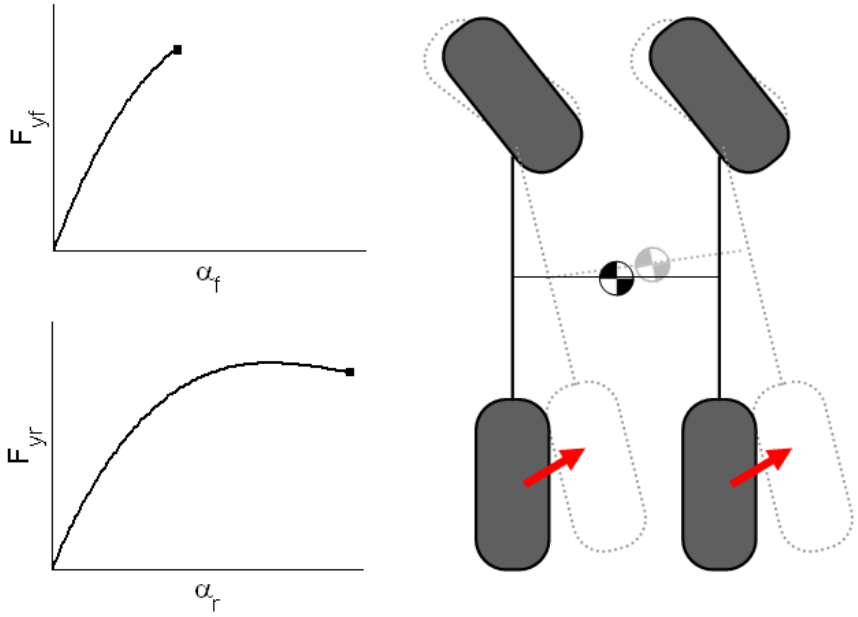

Figure 5.3: Limit Oversteering: Rear Axle Saturation

steer angle command in order to prevent the front tire forces from exceeding their peak. This can be achieved directly as front steering actuation enables immediate influence over the front tire slip angle (neglecting the effects of tire relaxation length).

In the case of rear tire saturation, the actuator and the control variable are non-collocated, with front steering only having an indirect influence over rear slip angle. The desired steering response in a limit oversteering situation is to quickly countersteer to immediately decrease the yaw rate. This serves, on a slower time scale, to reduce the rear slip angle through the vehicle dynamics, bringing the rear tire forces back within their limits of adhesion.

The envelope control system design proposed in this work follows these desirable steering responses to the limit understeering and oversteering situations. The system continually monitors the front and rear slip angles and their peak lateral force limits. When the vehicle is operating within the safe handling envelope, the controller directly sends the driver steering commands through. When either axle is sensed to be close to their maximum lateral grip, the controller intervenes. Using a simple feedback control law, it limits the steer angle when the front tires approach saturation, and countersteers when the rear tires are sensed to be close to their limits of traction.

Given two control objectives and only a single actuator, the control system must prioritize which axle to address in situations where both tires have reached the borders of the envelope. In this case, the controller prioritizes rear saturation over front saturation for driver safety and vehicle stability.

5.2.1 Envelope control algorithm

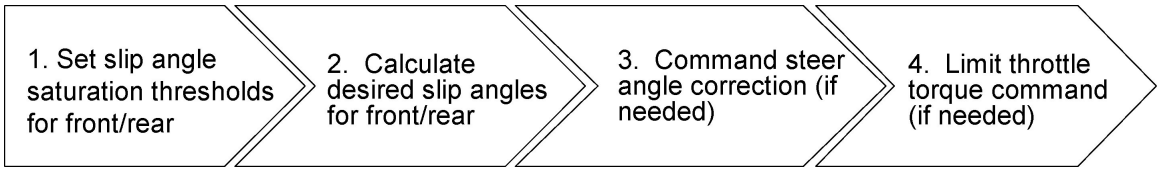

Figure 5.4: Envelope Control Algorithm

The real-time control algorithm is as follows:

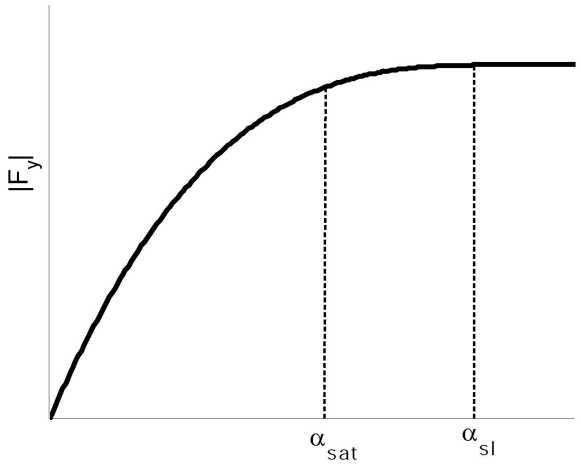

Figure 5.5: Setting a Slip Angle Threshold

1. **Set slip angle threshold for front/rear.**

   We first quantify when an axle is close to saturation by setting a slip angle threshold α_{sat} for each axle (illustrated in Figure 5.5):

$$\alpha_{sat} = sf \cdot \widehat{\alpha}_{sl} \qquad sf \in (0, 1] \tag{5.1}$$

$$= sf \cdot \tan^{-1}\left(\frac{3}{C_\alpha \widehat{I}_f}\right) \tag{5.2}$$

   where $\widehat{\alpha}_{sl}$ is the estimated slip angle at which full sliding occurs, sf is a constant scaling factor chosen a priori, C_α is the axle cornering stiffness and $\widehat{I}_f$ is the estimated inverted peak force limit of the axle as determined from the pneumatic-trail based observer in Section 4.3.2.

2. **Calculate the desired front/rear slip angles.**

   The next step is to calculate the desired front and rear axle slip angles. First, we create a piece-wise linear mapping function that takes the input slip angle α_{in} and outputs a desired slip angle α_{des}:

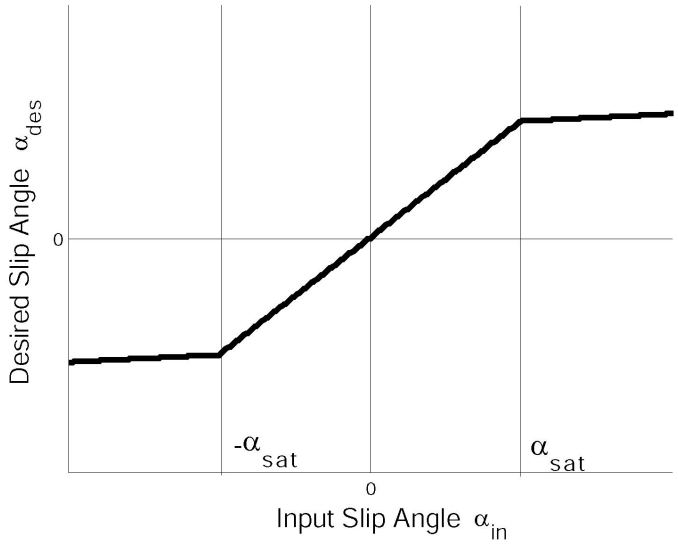

Figure 5.6: Slip Angle Mapping Function

$$\alpha_{des} = \begin{cases} \alpha_{in} & \text{if} \quad |\alpha_{in}| < \alpha_{sat} \\ \frac{3\alpha_{sat}\text{sgn}(\alpha_{in})}{3-\alpha_{in}\text{sgn}(\alpha_{in})+\alpha_{sat}} & \text{else} \end{cases} \tag{5.3}$$

Plotted in Fig. 5.6, this mapping function sets the desired slip angle to be identical to the inputted slip angle when $|\alpha_{in}| < \alpha_{sat}$. When $|\alpha_{in}| \geq \alpha_{sat}$, the desired slip angle is heavily saturated to be near α_{sat}.

For the **front** axle, α_{in} is the driver commanded front slip angle $\widehat{\alpha}_{HW}$, which is calculated from the estimated sideslip angle $\widehat{\beta}$ and translated to the front axle:

$$\widehat{\alpha}_{HW} = \widehat{\beta} + \frac{ar}{V_x} - \delta_{HW}. \tag{5.4}$$

By using the driver commanded steer angle δ_{HW}, instead of the actuated steer angle, the controller prevents the driver from commanding a slip angle that would exceed the limit.

For the **rear** axle, the same mapping function in Eq. (5.3) is used, but with one

difference. Because the driver commanded rear slip angle is equivalent to the actual rear slip angle, the α_{in} for the rear axle is simply $\widehat{\alpha}_r$.

3. **Command steer angle correction (if needed).**

   From the desired slip angles calculated from the previous step, the controller determines the steer angle correction $\Delta\delta$ that is added on top of the driver handwheel command. The final commanded steer angle δ sent to the steer-by-wire steering motors is:

$$\delta = \delta_{HW} + \Delta\delta. \tag{5.5}$$

   To determine $\Delta\delta$, we consider the situations that either the front or rear axles is saturated. If the **front** axle nears saturation, an integral feedback control law is used to maintain the desired steer angle δ_{fdes} corresponding to the maximum front axle force.

$$\dot{\delta}_{fdes} = K_{pf}\left(\widehat{\alpha} - \alpha_{fdes}\right) \tag{5.6}$$

   where K_{pf} is a constant integral feedback gain. Therefore, the steer angle correction $\Delta\delta_f$ necessary to keep the front slip angle within its limit is:

$$\Delta\delta_f = \delta_{fdes} - \delta_{HW} \tag{5.7}$$

   For the case of **rear** axle saturation, the control law actively reduces the rear slip angle rather than holding it near the limits. It countersteers when the rear slip angle exceeds its threshold by using the following proportional control law:

$$\delta_{rdes} = K_{pr}(\widehat{\alpha}_r - \alpha_{rdes}) \tag{5.8}$$

   where K_{pr} is a constant proportional feedback gain. The steer angle correction

$\Delta\delta_r$ necessary to keep the rear slip angle within its limit is:

$$\Delta\delta_r = \delta_{rdes} - \delta_{HW} \tag{5.9}$$

Finally, given two possible steer angle corrections, $\Delta\delta_f$ and $\Delta\delta_r$, the controller must decide which to employ in the case that both tires are near saturation. To maintain vehicle stability, the controller places the priority on preventing limit oversteering situations first. Figure 5.7 illustrates the logic employed to decide which corrective steer angle action (if any) is selected.

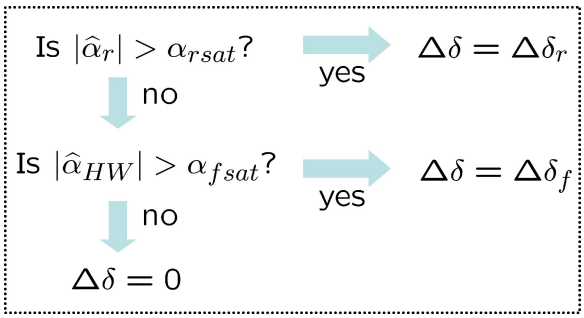

Figure 5.7: Controller Logic Prioritizing Rear Saturation

4. **Limit throttle torque command (if needed).**

   Because the envelope controller thus far only uses steering inputs to stabilize the vehicle, the driver is free to command aggressive speeds even as the controller attempts to bring the vehicle back within the safe envelope with steering corrections. It is for this reason that this final step is included in the controller. In this step, we impose a limit on the throttle torque command when corrective steering action is taken (i.e. $\Delta\delta \neq 0$). The rationale behind this is as follows. The vehicle's lateral acceleration can be modeled by Eq. 1.1. During a turn, the driver commands a turning rate and speed. Yet, on any given road surface, the available tire-road friction limits how much lateral acceleration can be achieved. If the maneuver is not physically attainable (either because yaw rate or speed is too high) the envelope controller could (a) both reduce yaw rate and on a slower

time scale reduce the sideslip rate by briefly countersteering and (b) limit the throttle torque command to allow the vehicle to slow down. Essentially, this step enables the driver to successfully negotiate the desired turn but at a slower speed.

Because the experimental vehicle P1 has rear wheel drive, sudden braking would generate rear longitudinal forces, which decreases the available lateral force capability of the rear axle [43]. Thus, it is be desirable to set the rear torque command to zero (rather than braking) during controller intervention in order to minimize the longitudinal force generation while the vehicle nears the boundary of its lateral limits:

$$\tau_{rear} = \begin{cases} 0 & \text{if} \quad \Delta\delta \neq 0 \\ \tau_{driver} & \text{else} \end{cases} \tag{5.10}$$

The inclusion of this feature assists the steering controller in preventing the driver from continuing to command both unsafe speeds and aggressive steer angle commands.

5.3 Combining the Observer and Controller

Ultimately, the overall system combines the Pneumatic Trail Nonlinear Observer developed in Section 4.3.2 and the controller designed in this chapter. As is generally true for any combined estimator and controller framework, it is crucial to understand the interactions between the two subsystems and the issues raised when combining them. This is especially true for this system, where we rely on the steering motors of the vehicle to operate in dual capacities: as steering actuators (for the controller) and as virtual sensors (for the observer). By linking the sensor and actuator together, we must manage their inevitably coupled relationship. Nonetheless, successfully doing so opens the possibility to stabilize the vehicle while eliminating the need for additional sensing requirements.

The performance of both subsystems is coupled. On one hand, the performance of the envelope controller heavily relies on the accuracy of the slip angle and peak force estimates outputted from the nonlinear observer. Noisy estimates would assuredly cause the envelope controller to unnecessarily intervene with the driver's commands. On the other hand, the estimation method depends on the tire pneumatic trail information in steering torque, requiring sufficient lateral excitation for proper estimation.

Ideally, the controller should receive truthful estimates of slip angle, and early and accurate identification of the peak lateral force. Also, the controller should output smooth steering corrections to keep the vehicle within its limits to enable accurate estimation. We keep these goals in mind when combining the observer and controller together. The following discusses the considerations taken for each subsystem for final system integration.

5.3.1 Controller Gain Selection

For the controller, we have the freedom of adjusting the constant gains K_{pf} and K_{pr} to ensure that the controller output is smooth, yet responsive enough to keep the slip angles within the desired values. Low gains (on the order of 0.1) reduce the variability of the controller output. High gains (greater than 0.5) achieve better response time but can result in overshoot.

Because the limit understeering is inherently a stable vehicle response, a low gain is chosen for the front axle integral gain K_{pf}. On the other hand, limit oversteering results in unstable vehicle motion, so a larger gain is chosen for the rear axle proportional gain K_{pr} to maintain stability.

5.3.2 Observer Algorithm Modification

For the observer, our objective is to yield accurate estimates when there is sufficient information from the steering torque. When the vehicle nears the boundary of handling envelope and the controller takes corrective steering action, it is important that the observer continues to output accurate slip angles. Otherwise, the controller would intervene based on faulty slip angle information.

However, during controller deployment, we recognize that the steering actuator does not serve well as a virtual sensor. Due to the high bandwidth of the steer-by-wire motors, higher frequency effects such as tire relaxation length should be considered for accurate friction estimation. Fortunately, because the controller is designed to intervene once the vehicle approaches its handling limits, we can assume that the system already has sufficient knowledge of the vehicle's peak friction limit during these situations. Therefore, a modification is made to the observer algorithm outlined in Section 4.3.2 for the combined system: When the envelope controller is actively deployed, we suspend peak force (friction) estimation and hold the last estimate.

5.4 System Validation in Simulation

This section applies the combined observer and controller system to a simulated vehicle. The goal of this simulation is to demonstrate that the estimation and control subsystems interact as expected, and that the overall system is able to keep the vehicle within its safe operating envelope. This simulation is also a useful tool to learn about the effects of controller gain tuning and how the resulting vehicle motion is affected with envelope control.

The simulation model includes the following:

- The vehicle is represented by a single-track planar model with variable longitudinal speed (see Fig. 4.2). The bicycle model parameters are chosen to emulate the handling characteristics of P1, the steer-by-wire experimental testbed pictured in Fig. 2.5.

- A 5 Hz low-pass filter is applied to the actuated steer angle to approximate the bandwidth of P1's steering system.

- Front lateral tire forces are represented by the nonlinear Fiala tire model in Eq. (2.9).

- Rear tire forces are represented using the full coupled longitudinal/lateral Fiala model to account for the rear wheel drive and regenerative braking system of

the rear wheels (refer to Eq. (2.10)).

- Static lateral weight transfer model, which was introduced in Section 2.3.4.
- Static longitudinal weight transfer model, which is introduced below:

$$-F_{zf}(a+b) - ma_x h + mgb + \tau_r = 0 \tag{5.11}$$

where a and b are the distances of the front and rear axles from the CG, h is CG height, F_{zf} is the front axle normal force, m is the vehicle mass, a_x is the longitudinal acceleration, g is acceleration due to gravity, and the rear drive torque τ_r is defined to be positive for accelerating and negative for braking. The resulting rear axle load can be found by

$$F_{zr} = mg - F_{zf}. \tag{5.12}$$

- Real-time lateral limits observer from Chapter 4.
- Envelope controller, which can be switched on/off for simulation purposes. Throttle limit can also be switched on/off.

Although the simulation assumes perfect measurements are available to the observer, the tire normal loads resulting from the lateral and longitudinal weight transfer are unknown to the estimation process. The envelope controller relies solely on the observer's slip angle and peak force estimates. The simulation is coded in MATLAB and the results are presented in the next section.

Table 5.1: Simulation Test Matrix for Overall System

Simulated Maneuver	**Steer Angle Amplitude (°)**	**Speed (m/s)**	**Purpose**
1. Slalom	12	15	Investigate system response to quickly changing steering command. Induce rear saturation (limit oversteer).
2. Step steer	10	15	Determine the controller response to a continually aggressive steer angle
3. Dropped throttle oversteer	10	Initially 10	Investigate controller/observer response to a destabilizing maneuver and unmodeled effects of from longitudinal dynamics.

5.4.1 Simulation Results

The simulation results of three representative maneuvers – a slalom, step steer and dropped throttle oversteer – are presented here. Table 5.1 gives the details and investigative purpose of each maneuver. All maneuvers were performed on a theoretical $\mu = 0.6$ surface, which roughly corresponds to driving on gravel. For all of the maneuvers, the following parameters are used: The integral control gain for front axle saturation is $K_{pf} = 0.2$, the proportional control gain for rear saturation is $K_{pr} = 0.5$, the front axle slip angle threshold safety factor is $sf_f = 1$, the rear axle slip angle threshold safety factor is $sf_r = 0.8$, and the observer feedback gain is set to be $K_{\alpha f} = 1.5 \times 10^{-4}$.

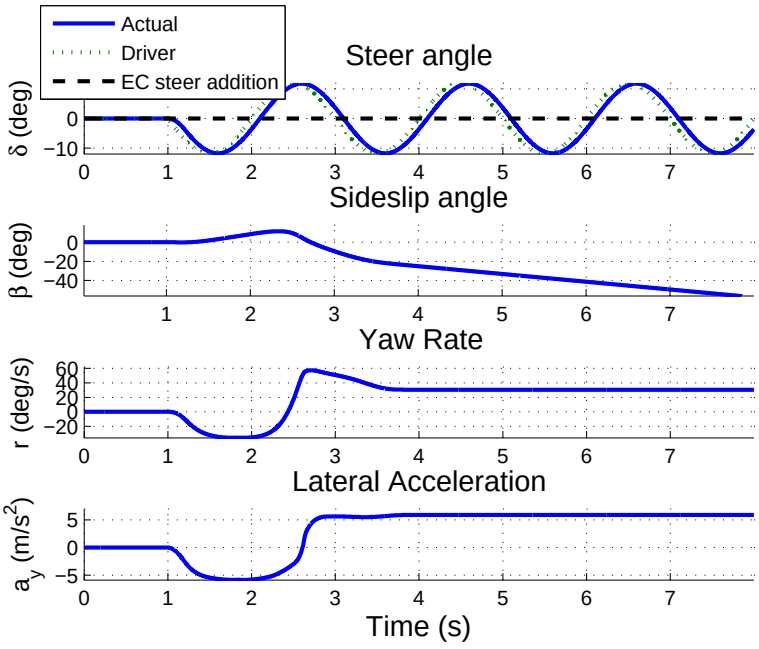

(a) Maneuver Time History

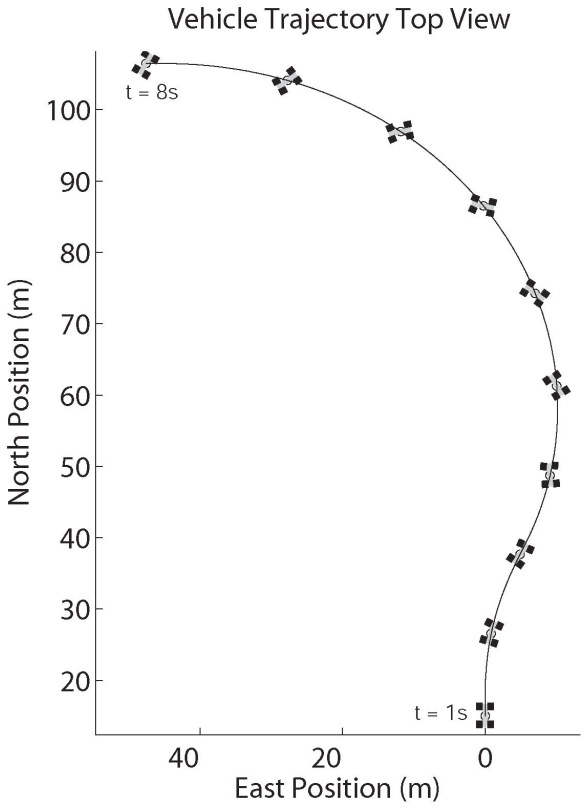

(b) Vehicle Trajectory

Figure 5.8: Simulated Slalom on $\mu = 0.6$ Road (No Control)

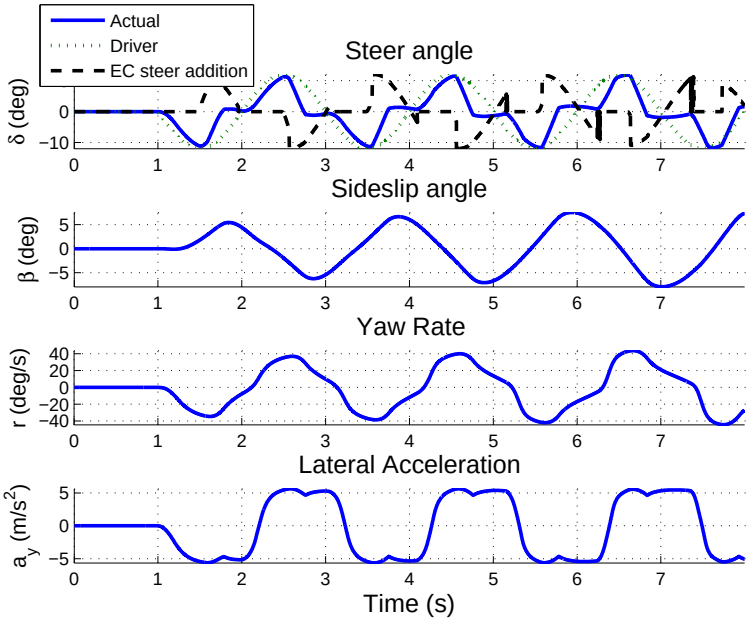

(a) Maneuver Time History

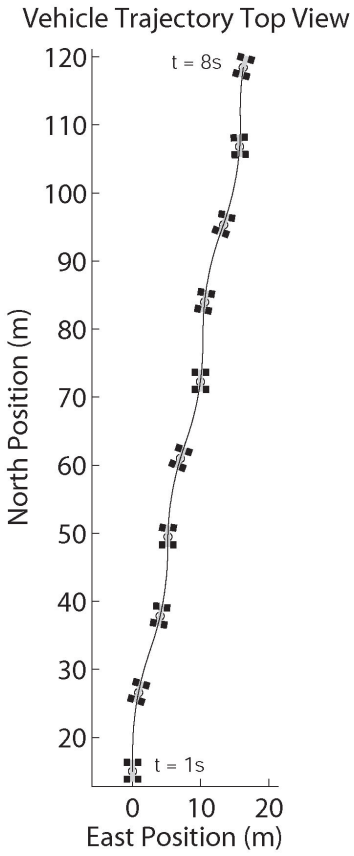

(b) Vehicle Trajectory

Figure 5.9: Simulated Slalom on $\mu = 0.6$ Road (With Control)

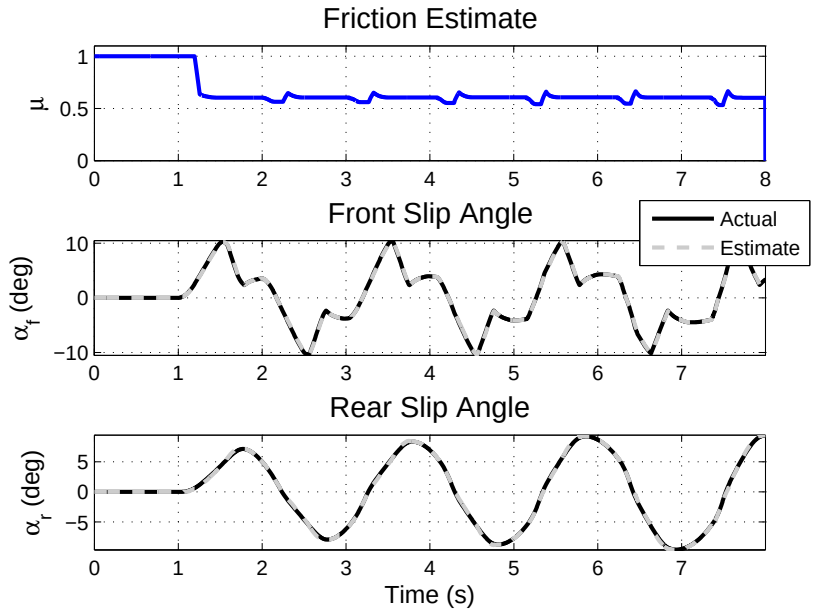

Figure 5.10: Simulated Slalom (With Control): Estimation Results

Slalom

With the controller off, a 12° 0.5 Hz slalom is performed at a constant speed of 15 m/s (Fig. 5.8(a)) on a $\mu = 0.6$ road. As the simulation demonstrates, commanding an aggressive slalom maneuver on this moderate-friction surface results in the vehicle's rear tires losing traction, sending the vehicle into an unstable spin. This is evident from the overhead view of the vehicle's trajectory plotted in Fig. 5.8(b).

With the controller on, the same maneuver is performed. The controller is able to provide periodic countersteering corrections to stabilize the vehicle motion (see Fig. 5.9). The resulting vehicle trajectory closely follows the driver's intended slalom maneuver. The observer's friction and front and rear slip angle results are presented in Fig. 5.10. Throughout the maneuver, the estimation algorithm is able to closely track the actual slip angles and, with slight variation, correctly identify the friction coefficient of $\mu = 0.6$. As expected, the corrective front steering action has immediate influence on the front slip angle, the steering inputs must propagate to the rear slip

angles through the vehicle dynamics.

Step Steer

The second maneuver presented is a step steer maneuver in which the driver maintains an aggressive steer angle command of 10° and a constant speed of 15 m/s, shown in Fig. 5.11(a). Uncontrolled, the vehicle once again enters an unstable drift, illustrated in Fig. 5.11(b).

With the controller on, the vehicle remains stable, shown in Fig. 5.12(a). (Note that in this maneuver, the throttle limit feature of the envelope controller was turned off to investigate how the control system responds to a continually aggressive steer angle and speed.) Interestingly, we observe a cyclical deployment of the controller in response to the step steer. As the vehicle nears the limits of lateral tire grip, the controller countersteers, bringing the vehicle back within the safe operating envelope. Steering authority is then returned to the driver, at which point the driver maintains the 10° steer angle command and pushes the car back near the boundary of safe handling. The cycle is repeated throughout the maneuver, resulting in the catch and release behavior of the car.

Although the oscillations in yaw rate may appear extreme in Fig. 5.12(a) and would certainly be noticeable to onboard passengers, it is important to note that the resulting vehicle trajectory (presented in Fig. 5.12(b)) is not oscillatory and closely follows the intended path. However, with only front steering as the available actuator, it is not surprising that the controller's corrective action must be disruptive in order to stabilize the car while maintaining a constant speed. This result strongly motivates the potential benefit of imposing a torque throttle limit, described in Section 5.2.1 in the control algorithm. Placing limits on the vehicle's speed would serve to both prevent the driver from commanding unsafe vehicle trajectories and perhaps reduce the extremity of the controller's corrective steering inputs. This point is further explored in experiment in Section 5.5.

Finally, for this maneuver, the observer's friction and slip angle estimates are shown in Fig. 5.13. Again, the estimator is able to closely track the slip angles and detect the correct friction coefficient of $\mu = 0.6$.

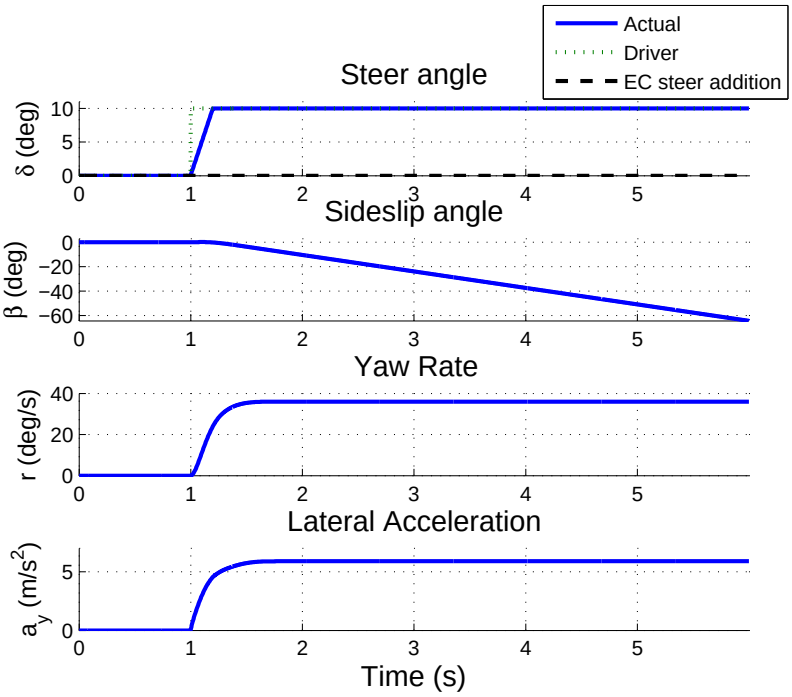

(a) Maneuver Time History

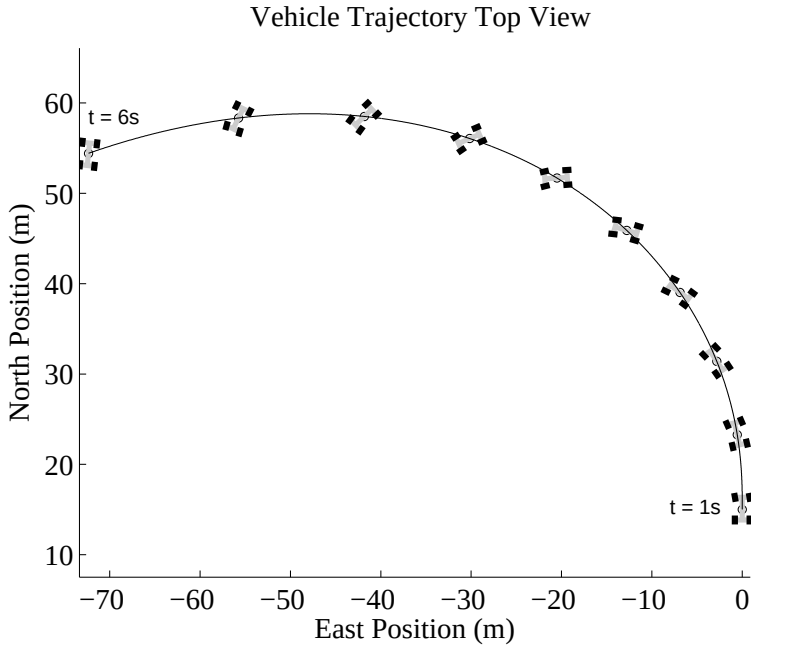

(b) Vehicle Trajectory

Figure 5.11: Simulated Step on $\mu = 0.6$ Road (No Control)

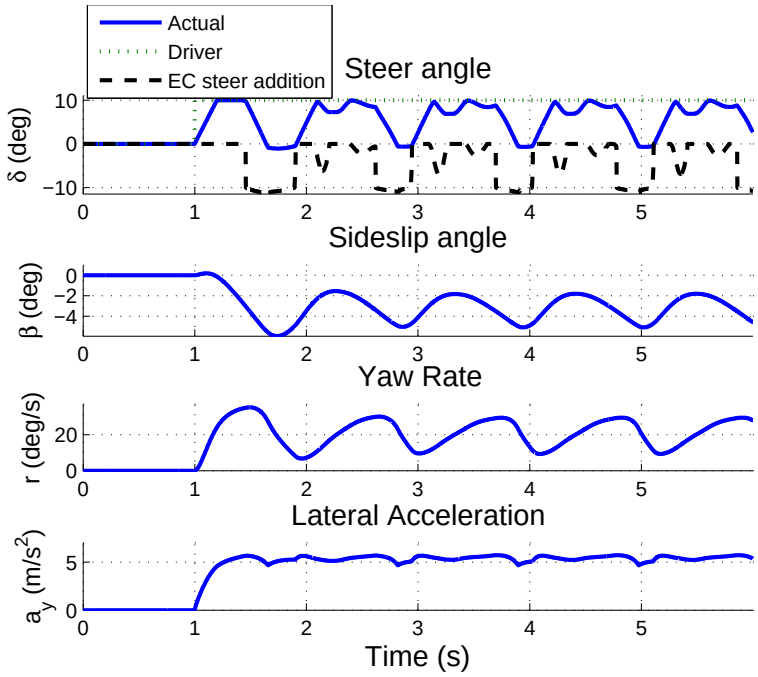

(a) Maneuver Time History

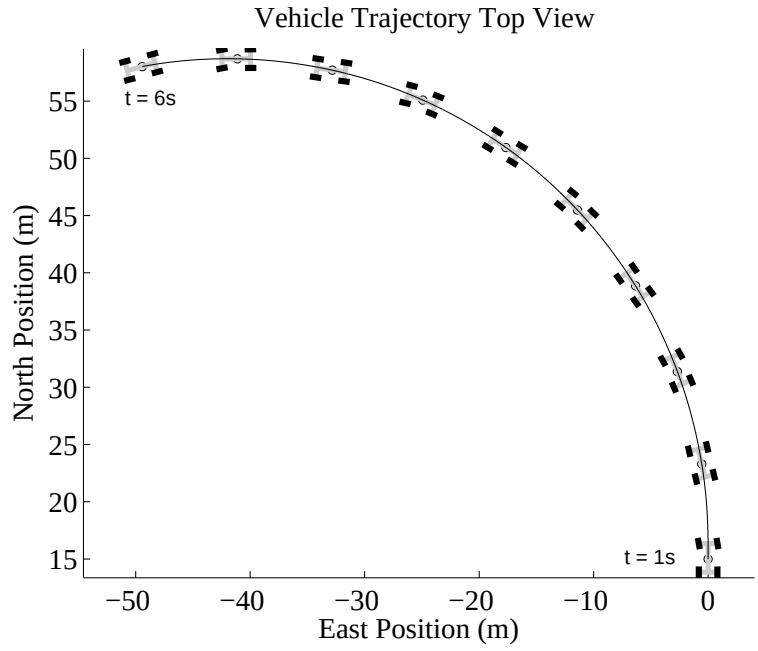

(b) Vehicle Trajectory

Figure 5.12: Simulated Step on $\mu = 0.6$ Road (With Control)

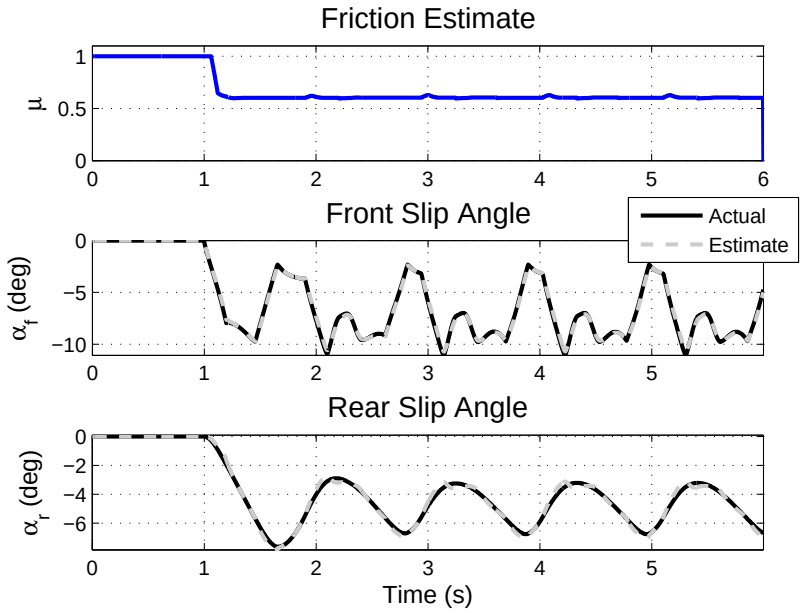

Figure 5.13: Simulated Step (With Control): Estimation Results

Dropped Throttle Oversteer

The final maneuver simulated is a dropped throttle oversteer, shown in Fig. 5.14. In this maneuver, the driver commands a 10° step steer with an initial speed of 10 m/s. (If the driver were to continue this moderate speed, the vehicle would follow the intended turn and remain within the limits of traction, as plotted in light gray in Fig 5.14(b).) However, while turning, at $t = 3$s the driver suddenly "drops the throttle", letting go of the accelerator pedal, which on P1 briefly engages the rear regenerative brakes for 0.5s. This induces a forward weight shift to the front axle. Because the vehicle is already cornering near the limits of handling, braking causes the rear tires to saturate, creating an oversteer condition and resulting in an unstable drift.

With the envelope control system on, the onboard estimator quickly senses that the rear tire forces are near their limits of traction. A steer angle is added on top of the driver command, resulting in an immediate countersteer that brings the rear slip

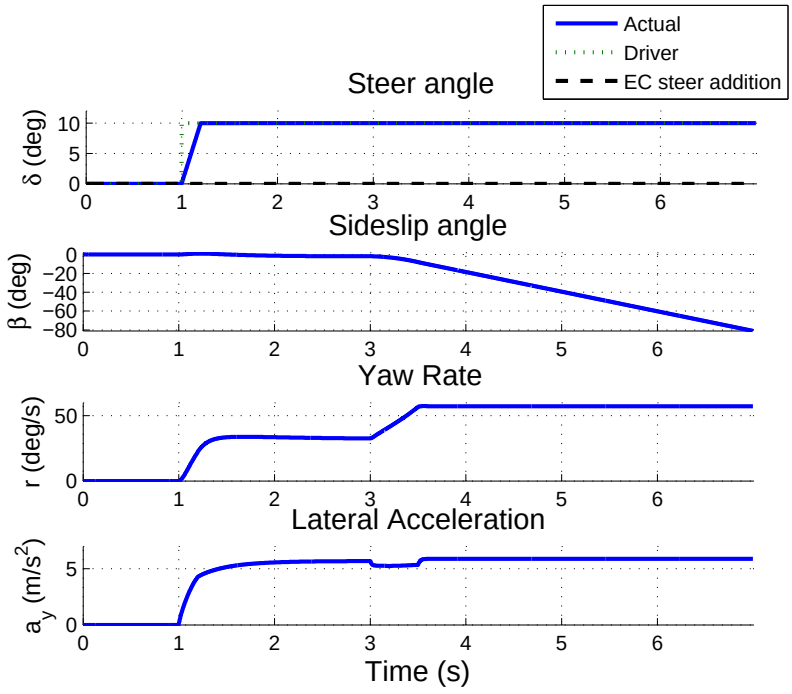

(a) Maneuver Time History

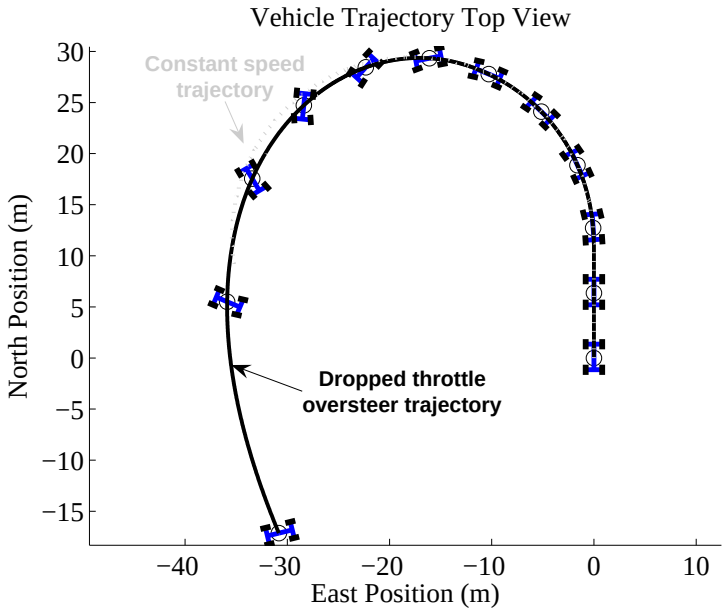

(b) Vehicle Trajectory

Figure 5.14: Simulated Dropped Throttle Oversteer on $\mu = 0.6$ Road (No Control)

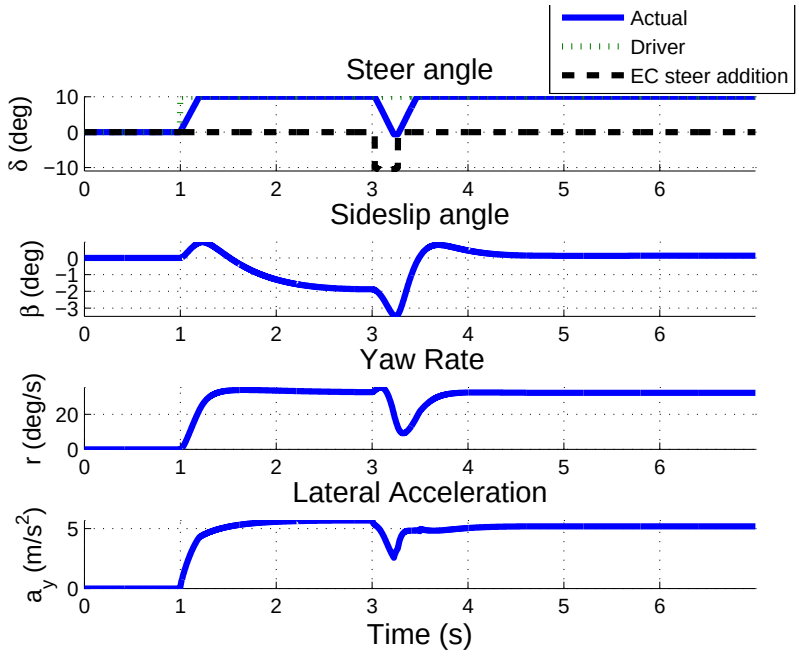

(a) Maneuver Time History

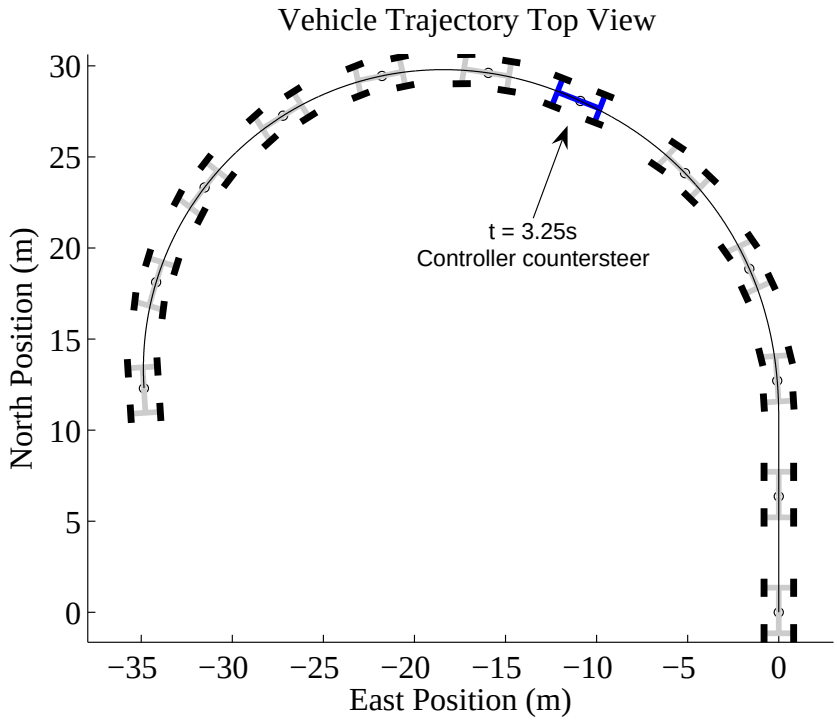

(b) Vehicle Trajectory

Figure 5.15: Simulated Dropped Throttle Oversteer on $\mu = 0.6$ Road (With Control)

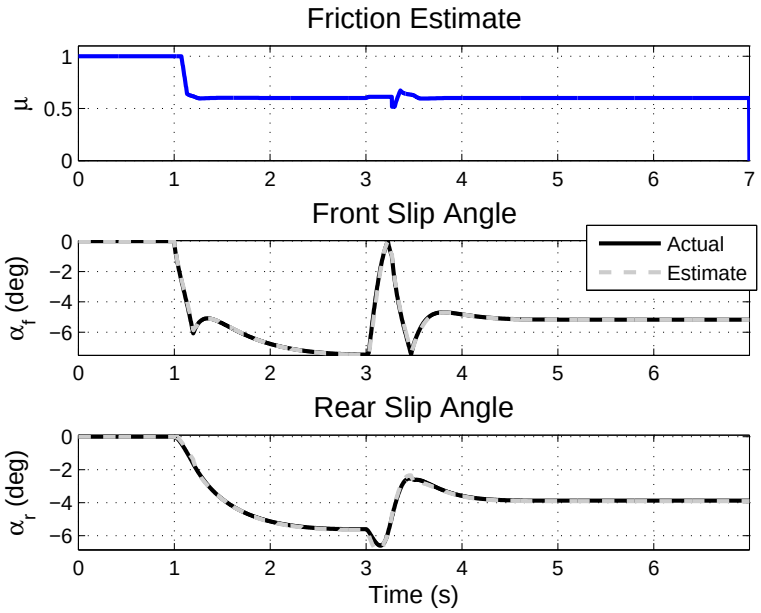

Figure 5.16: Simulated Dropped Throttle Oversteer (With Control): Estimation Results

angle back into the safe operating envelope (see Fig. 5.15(a)). Figure 5.14(b) plots the resulting vehicle trajectory and countersteer command at $t = 3.25$s.

Shown in Fig. 5.16, the slip angle estimates from the observer agree well with truth. The friction coefficient is correctly identified. Overall, these results demonstrate the potential for the combined envelope controller and observer system to keep tire forces within their limits and prevent unstable vehicle responses.

5.5 Experiments

Experimental results are presented from the overall control system implemented onboard P1 (see Section 3.2.2). The following three experimental maneuvers are chosen:

1. **Slalom** at constant speed - control system **on**
2. **Dropped throttle oversteer** - control system **off**

Table 5.2: Controller Status Flag Legend

Controller status	Indication
-1	OFF
0	ON, no saturation
1	ON, front saturation
2	ON, rear saturation

3. **Series of three dropped throttle oversteer maneuvers** - control system **on**

All maneuvers are driven at the Shoreline testing lot, which provides a loose gravel on asphalt surface with a variable friction coefficient of $\mu = 0.5$ to 0.7.

For these experimental plots, an integer controller status flag is outputted to indicate whether the control system is on, and which axle, if any, is near saturation (see Fig. 5.2).

5.5.1 Slalom - Controller On

The first maneuver is a slalom driven at a constant speed of 9 m/s. For this maneuver, the throttle limit feature of the envelope controller is inactive. The time history of the maneuver is shown in Fig. 5.17(a). When the vehicle is turning, the observer for the most part senses that the front axle is near saturation, as indicated by the controller status flag equaling 1. This agrees with the inherent handling characteristics of P1, which exhibits limit understeering characteristics for most maneuvers. Only during the initial left and right turns of the slalom does the controller briefly countersteer to prevent the rear axle from exceeding the estimated boundary. Otherwise, the actuated steer angle magnitude is limited to prevent excessive front axle saturation. Figure 5.17(b) plots the overhead view of the vehicle trajectory, which demonstrates that the vehicle follows the intended slalom path.

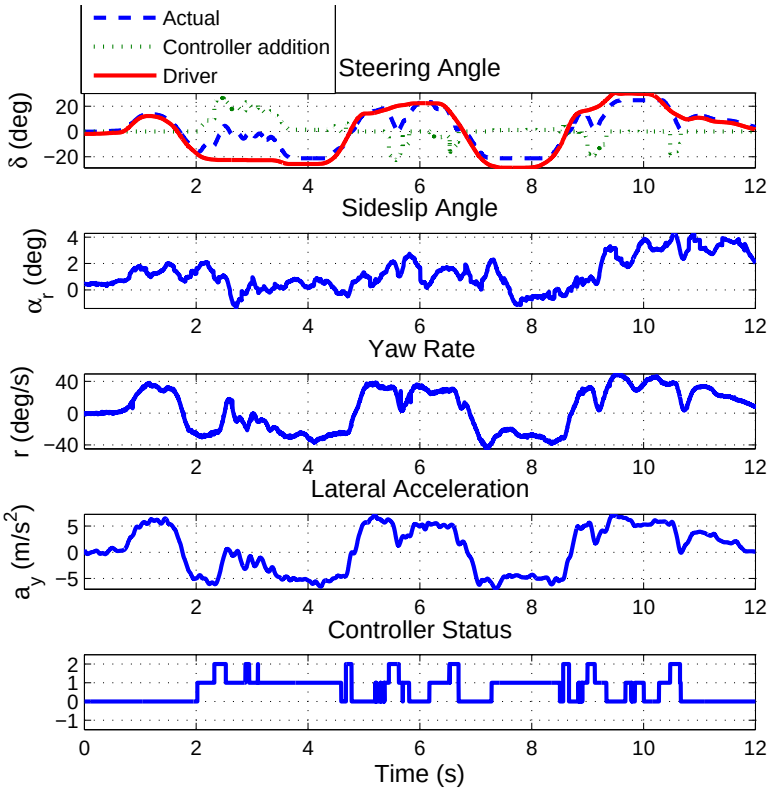

(a) Maneuver Time History

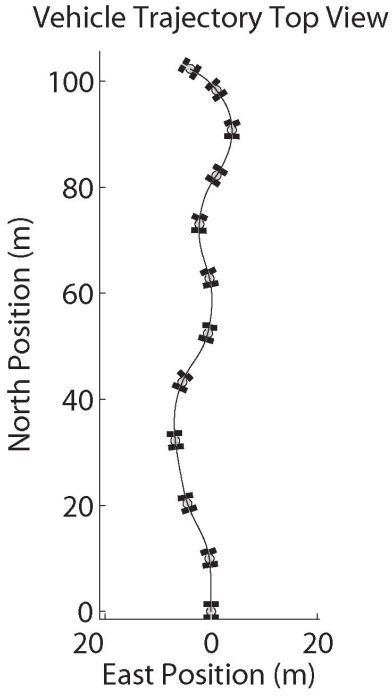

(b) Vehicle Trajectory

Figure 5.17: Experimental Slalom (Controller On)

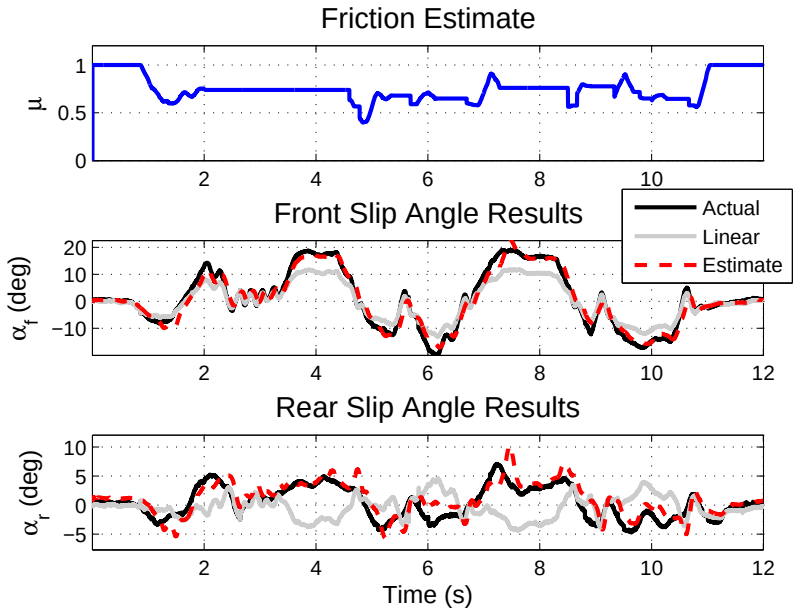

Figure 5.18: Experimental Slalom (Controller On): Estimation Results

The observer's estimates are presented in Fig. 5.18. As expected, the nonlinear observer outperforms the pure linear slip angle estimator. The observer's front slip angle estimates track the GPS-based measurements well. The slight rear slip angle estimation error is likely due to the lag from tire relaxation length, which is more pronounced at slower speeds such as this.

When friction estimation is on, the average estimate is $\mu = 0.7$, which falls within the expected range for dry, loose gravel. The variation of the friction estimate is due to two factors. First, the actual testing surface is uneven in its gravel distribution: patches of road with a build up of loose gravel provide less tire grip than areas with more asphalt exposure. Thus, a certain level of estimation variation is expected. Second, the peak force estimator block in the estimation algorithm is purely algebraic (see Fig. 4.1). Thus, any modeling errors in the linear pneumatic trail model and in the steering system model would result in errors in the peak force (friction) estimate.

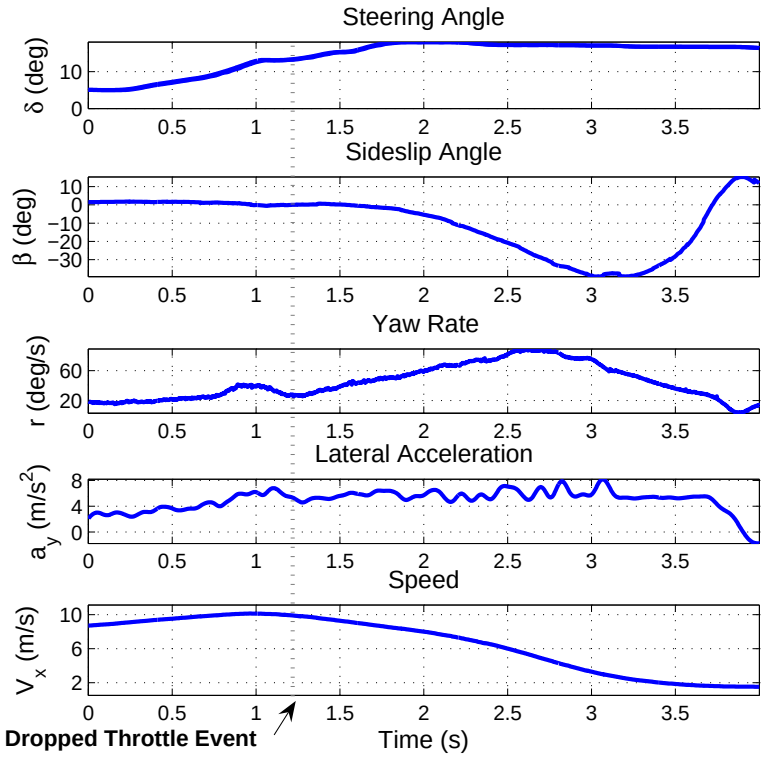

(a) Maneuver Time History

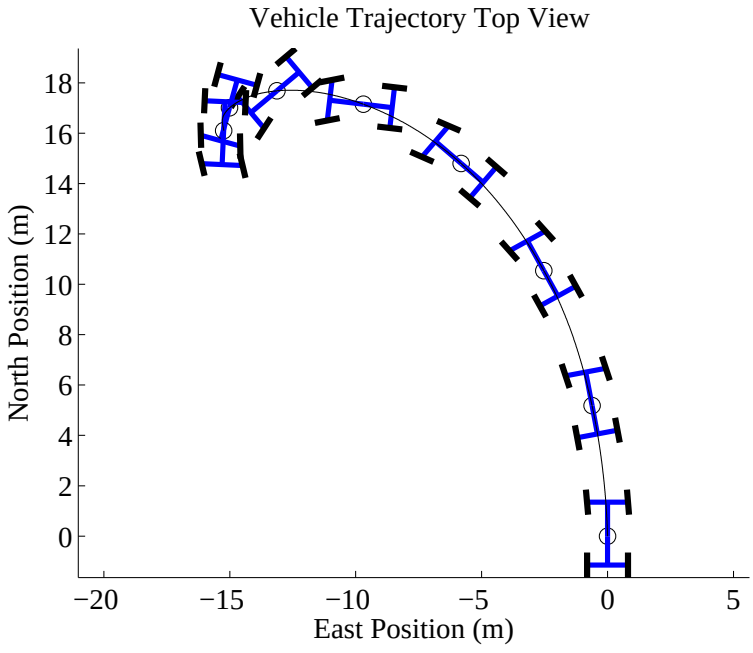

(b) Vehicle Trajectory

Figure 5.19: Experimental Dropped Throttle (Controller Off)

5.5.2 Dropped Throttle - Controller Off

The second maneuver presented is a dropped throttle oversteer with the envelope control system **off**. By letting go of the throttle suddenly during the turn, the driver applies the regenerative brakes of the drive motors of the rear wheels, inducing longitudinal weight transfer to the front axle. Because the vehicle is already cornering near the limits of handling, braking causes the rear tires to lose traction, creating an oversteer condition (see Fig. 5.19). The vehicle slows down to a stop after the spinout since the regenerative brakes were continually applied after the drop throttle was initiated.

This maneuver demonstrates that in experiment, without a stabilizing controller or a well-timed driver countersteer, a dropped throttle oversteer results in an unstable spin (illustrated in the overhead view of the car trajectory in Fig. 5.19(b)).

Figure 5.20(a) presents the estimation results for the maneuver. This kind of maneuver in which both tires are fully saturated provides an opportunity to investigate how the observer responds when the system becomes unobservable. The front and rear slip angle estimates track GPS well until the tires fully saturate after $t = 2.2$s. (To illustrate the degree of tire saturation at this point in the maneuver, Fig. 5.20(b) presents the tire curve calculated from the Fiala tire model using GPS slip angle measurements up until $t = 2.2$s, showing that both axles have exceeded their handling limits.) After $t = 2.2$s, the slip angle estimation error understandably grows, but the estimates quickly returns to tracking the actual values after the tires return to the observable region.

5.5.3 Series of Dropped Throttles - Controller On

The final experimental maneuver presented is a series of three dropped throttle oversteer maneuvers performed in succession. Figure 5.21(a) plots the time history of the overall maneuver. As shown in Fig. 5.21(b), the onboard observer is able to estimate front/rear slip angles accurately throughout test run. In addition, the friction coefficient is correctly identified even at low levels of lateral acceleration. The observer's performance is particularly encouraging given the variability of the driving surface

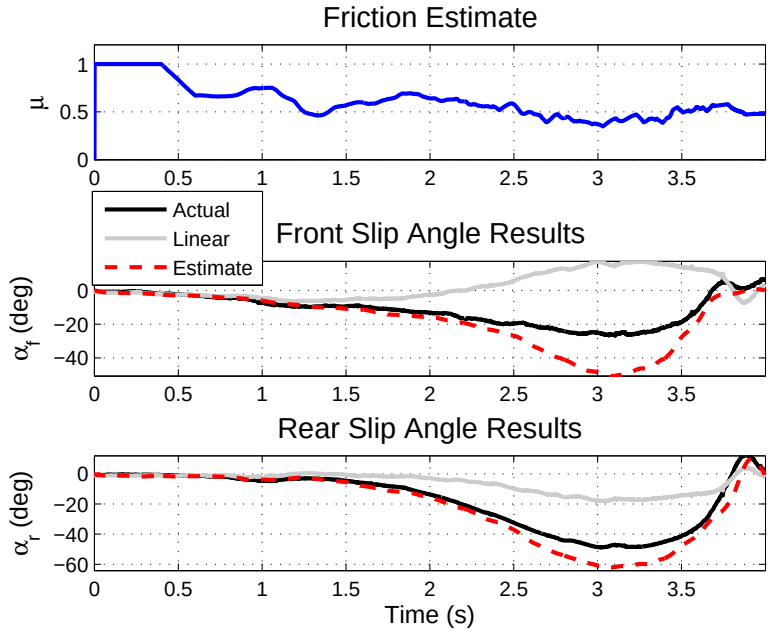

(a) Estimation Results

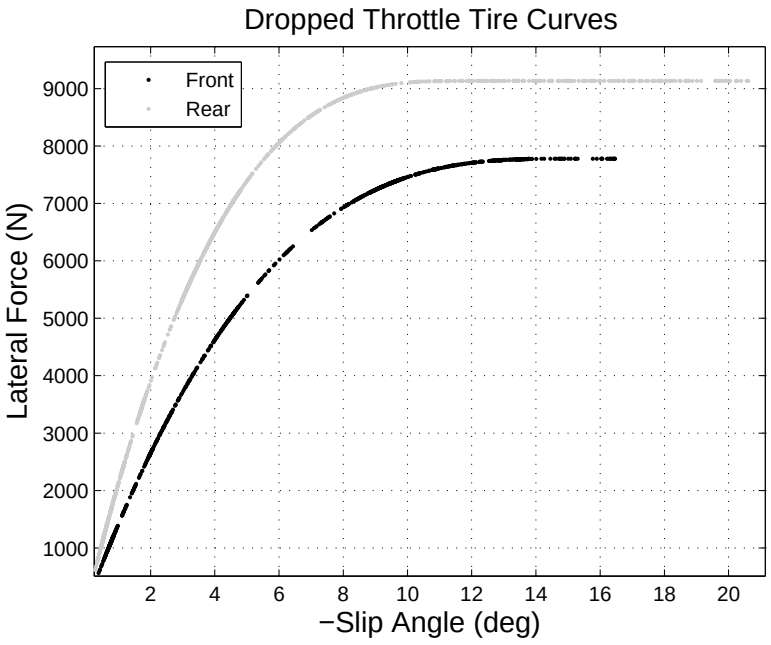

(b) Tire Curve

Figure 5.20: Experimental Dropped Throttle (Controller Off): Observer Results

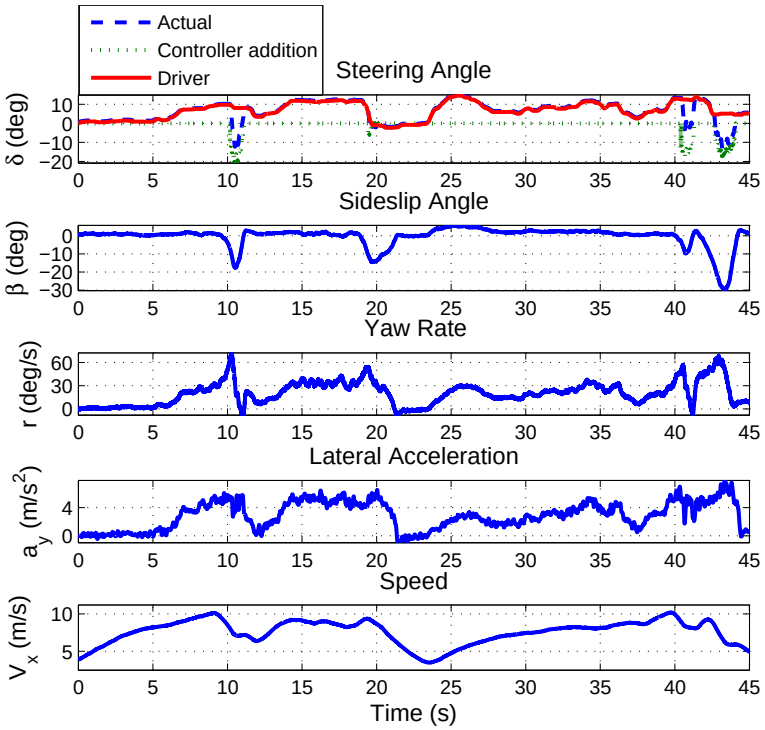

(a) Maneuver Time History

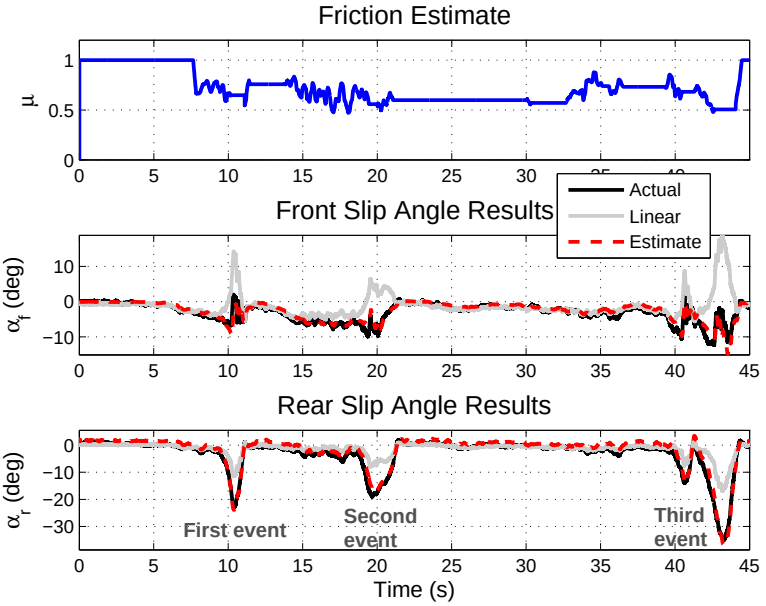

(b) Estimation Results

Figure 5.21: Experimental Series of Dropped Throttles (Controller On)

and the presence of unmodeled longitudinal dynamics in this maneuver.

For the remainder of our discussion, we focus our analysis on the controller's response during the maneuver. Because each of the three dropped throttle events exemplifies a different aspect of the control system, they are discussed separately below. Note that for this maneuver, the throttle limit feature of the envelope controller is active.

First Dropped Throttle: Controller Correction

For the first dropped throttle event, the driver suddenly engages the rear regenerative brakes during the turn. Without corrective action, this would result in the rear tires losing traction and pushing the car into an unstable spin similar to what was illustrated in Fig. 5.19.

With the envelope control system on, however, the onboard estimator senses that the rear tire forces are near their limits of traction. Using the proportional feedback controller and steer-by-wire actuation, a steer angle is added on top of the driver command, resulting in a quick countersteer that brings the rear slip angle back into the safe operating envelope (see Fig. 5.22(b)). These results indicate that the combined envelope controller and observer system is able to keep tire forces within their limits and prevent unstable vehicle motion.

Second Dropped Throttle: Driver Correction

In the second dropped throttle event, the driver initiates her own countersteering correction to stabilize the vehicle (shown in Fig. 5.23). Because the driver successfully counteracts the potential instability, the envelope controller's steering action is minimal and simply serves to marginally increase the magnitude of the countersteer. This result highlights a desirable characteristic of envelope control that should not be lost: a stability control system should be unobtrusive to drivers who are able to make their own self-corrections. In situations where the driver does not self-correct, the controller would intervene to stabilize vehicle motion automatically, as was illustrated in the first dropped throttle event.

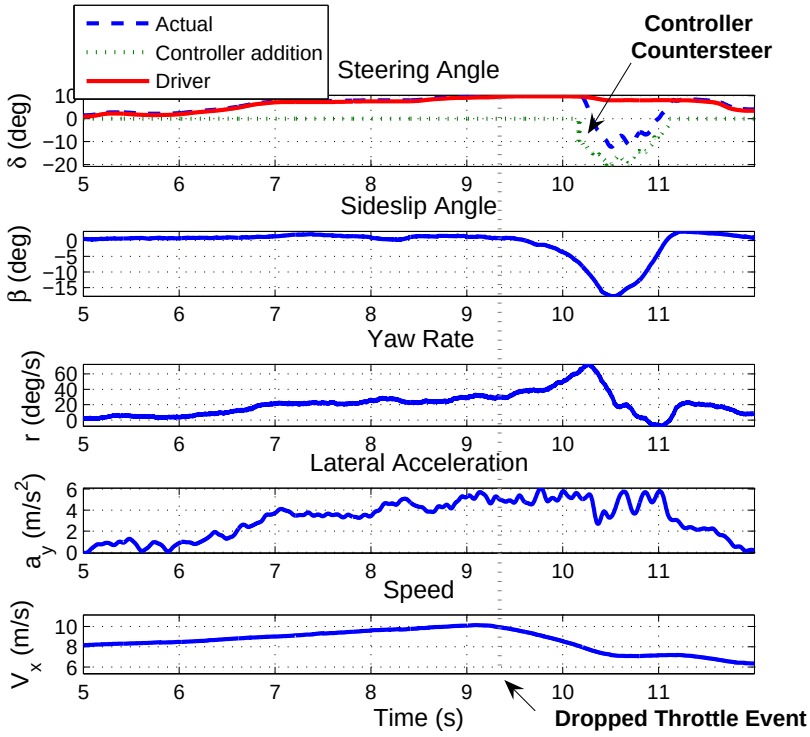

(a) Maneuver Time History

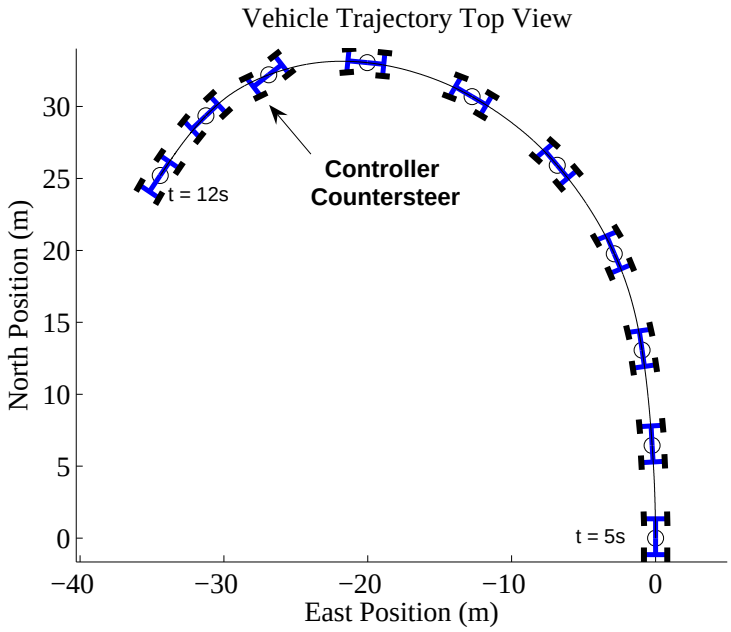

(b) Vehicle Trajectory

Figure 5.22: First Dropped Throttle (Controller On)

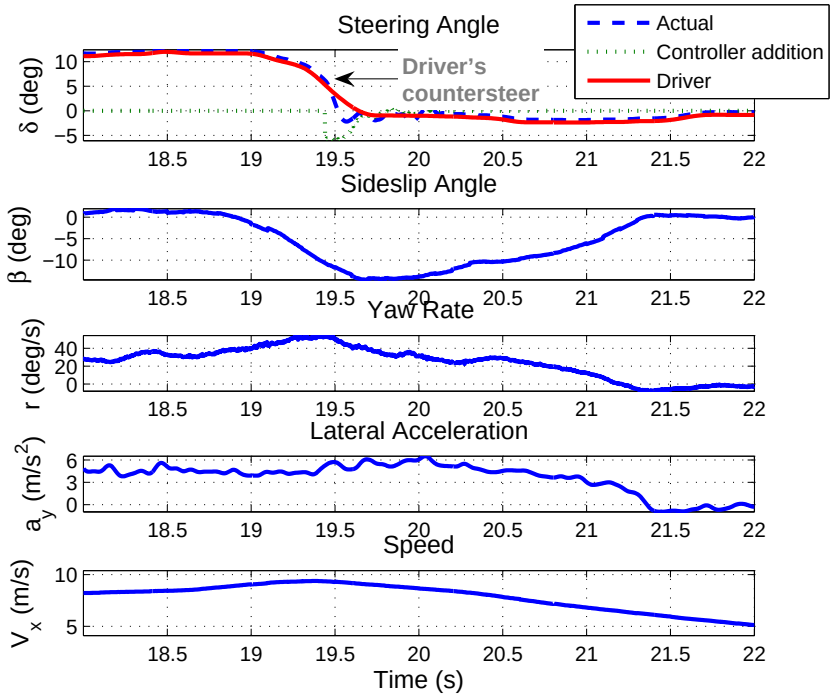

Figure 5.23: Second Dropped Throttle (Controller On, Driver Stabilized)

Third Dropped Throttle: Controller Catch/Release Corrections

The final dropped throttle event provides a good example of the controller having to make two steering corrections in quick succession (see Fig. 5.24). In this maneuver, the driver initiates the first dropped throttle at $t = 40$s. The controller senses the rear tire saturation and countersteers to immediately reduce yaw rate, which eventually decreases the sideslip angle and stabilizes the vehicle. However, shortly after at $t = 41.5$s, the driver speeds up, commanding an additional longitudinal drive force that reinitiates the rear axle slide. This produces a spike in rear slip angle, at which point the controller must countersteer for a second time and for a longer duration.

This maneuver demonstrates that using a feedback proportional control law on the rear axle's slip angles exhibits the desired behavior for the controller: for maneuvers that achieve larger sideslip angles, the controller's countersteering action is necessarily longer. Moreover, the longer intervention has the added benefit of slowing the vehicle

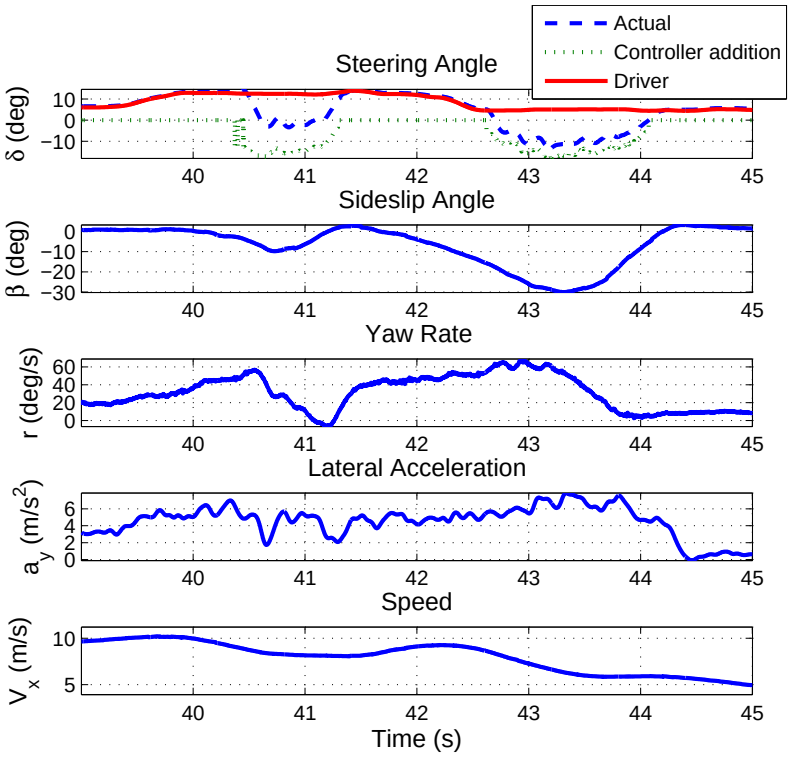

(a) Maneuver Time History

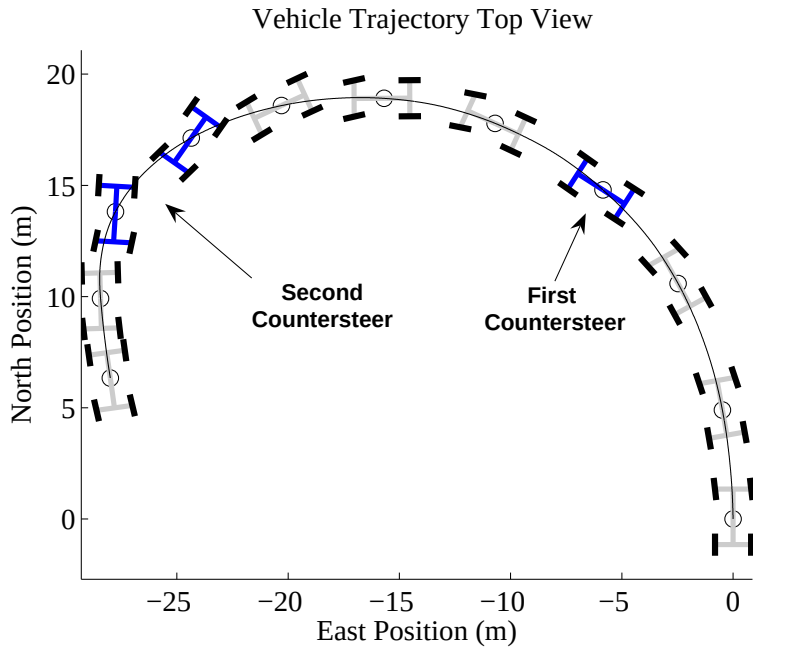

(b) Vehicle Trajectory

Figure 5.24: Third Dropped Throttle (Controller On, Sequential Deployment)

down more, resulting in safer vehicle trajectories after the steering correction has completed.

5.6 Comparison of Envelope Control and ESC

A natural question extending from this work is how the envelope control might compare with the production Electronic Stability Control (ESC) systems. Recall that from Chapter 1, ESC improves vehicle stability primarily through two mechanisms. First, it momentarily applies individual brakes to provide corrective yaw moments to keep the vehicle on an intended path as determined by the driver's steer angle input. Second, ESC serves to slow the vehicle down, making the reachable vehicle trajectories safer. To make a fair comparison with ESC, we consider the general form of envelope control which may utilize multiple actuators (for example, a combination of steering and differential braking corrections) and the early friction information contained in pneumatic trail.

There are some similarities between this general form of envelope control and ESC. In a limit oversteering response, the main action of both systems is to quickly reduce yaw rate (and on a slower time scale the sideslip angle). In addition, both systems act to slow the vehicle down during emergency situations and are designed to prevent unintended vehicle motion.

The differences between the two systems are quite notable. Taking advantage of the pneumatic trail information in steering torque, envelope control has access to information of the operating limits of the vehicle that ESC does not. Early knowledge of the lateral limits opens many possibilities in the future with envelope control. Although this investigation used a simple feedback control structure, it is conceivable that substantial improvements could be made in the design of the envelope controller to enable predictive and unobtrusive corrections. Moreover, envelope control with front steering actuation has access to an additional control input (front steering) to stabilize the vehicle motion.

5.7 Conclusions

First developed for aircraft, envelope protection is a control strategy that aims to prevent the aircraft from entering state or control regions outside of the safe flight regime. Using this as inspiration, the envelope control system introduced in this chapter was designed to keep passenger vehicles within a safe operating envelope using front steering actuation. Relying on accurate limit detection from the pneumatic-trail based observer, the controller used steering to keep the front and rear tires away from their lateral handling limits.

A simple feedback controller was demonstrated in simulation and experiment to maintain vehicle stability on a moderate-friction surface. With direct sensing and actuation of the front tires, the system was able to immediately affect front lateral force, preventing the front tires from exceeding their lateral grip. With indirect sensing and indirect actuation of the rear tires, the controller required aggressive actuator commands to influence rear tire forces. This was due to the fact that the controller's front steering inputs had to go through the dynamics of the vehicle before they could command a reduction in the rear tire forces. The addition of limiting the throttle input during envelope control intervention helped bring the vehicle to safer trajectories.

Utilizing the front steering motors both as the system's control actuator and virtual sensor raised interesting issues. By linking the actuation and sensing capabilities together, we had to make thoughtful design decisions that enabled both subsystems to work well together. Experimental results of the overall system demonstrated that steering actuators can serve effectively in dual capacities: to both steer the vehicle to a stable handling region and provide early lateral limit detection even at modest lateral accelerations.

Two aspects that remain to be studied for envelope control design and implementation on P1 include:

1. Investigating a control strategy that could determine earlier steering corrections that possibly would avoid overly-intrusive corrections. Dynamic trajectory planning might be a better use of the predictive limit information supplied by the

nonlinear observer.

2. Using the differential rear drive and regenerative brake of P1 to induce additional moment corrections on the vehicle during oversteering or understeering situations. This addition would require extending the estimation algorithm to include longitudinal forces.

Finally, this idea could also be extended to a vehicle with a 4-wheel steering system with direct sensing and actuation of each tire to allow for full control of vehicle.

Chapter 6

Conclusions

Vehicle control systems seek to prevent unintended vehicle behavior by assisting drivers in maintaining control of their vehicles. Unfortunately, current systems are limited by the lack of knowledge of the vehicle's state and operating conditions. Specifically, knowledge of the vehicle's sideslip angle and the tire's lateral handling limits are important information that is largely unavailable for current safety systems due the lack of accurate, inexpensive, and reliable sensor measurements in the highly cost sensitive automotive industry. Current and future vehicle control systems would benefit from knowledge of the vehicle's lateral handling potential and current state.

Motivated by this necessity, this thesis developed several estimation approaches that utilized the lateral limit information contained in total aligning moment, a quantity readily available from steering torque measurements in vehicles with steer-by-wire, EPS or Active Steering systems. When basing estimation on lateral force and GPS-based slip angle measurements to identify tire cornering stiffness and tire-road friction, experimental results demonstrated that friction detection was available after the tires achieved 80% of its peak lateral force capability. Using methods based on total aligning moment (or pneumatic trail) and GPS slip angle measurements, early friction identification was possible when the tires were operating at only 50% of its peak limits.

During periods of GPS signal loss, a final estimation approach was developed to estimate lateral tire properties. This method estimated peak lateral force directly

from pneumatic trail and provided slip angle estimates that were mathematically guaranteed to converge. This approach was advantageous for two reasons. First, it took advantage of the early friction information directly encoded in tire pneumatic trail, enabling early detection of the limits (when the tires utilized 50% of the peak lateral force). Second, it relied on measurements which are readily available on production vehicles. This method may allow future safety systems to predictively prevent, rather than react to, loss of control situations and can be integrated with GPS-based estimation approaches.

Finally, this work developed an envelope controller to keep the vehicle in a safe operating region using the estimated handling limits information from the nonlinear pneumatic trail based observer. The combined observer/controller system successfully used front steering corrections to maintain vehicle stability on a low-friction surface both in simulation and experiment.

There are several issues related to the estimation and control of the lateral tire forces that are important and left for future work:

- The consideration of longitudinal forces in the estimation of the lateral handling limits. As longitudinal and lateral tire forces are coupled through the friction circle [43], accurate identification of the tire's lateral grip during braking or accelerating should incorporate the effect of longitudinal forces.

- The development of a control strategy for vehicle envelope control that anticipates unsafe trajectories and smoothly corrects them. Certain techniques may better utilize the predictive limits information provided by the observer work in this thesis to more smoothly keep the vehicle within the safe envelope.

- The use of additional actuators beyond front steering to provide the controller with additional degrees of freedom. Rear steering, independent drive/brake forces, and active camber are some examples. In particular, previous studies have shown that independent braking is very effective at correcting vehicle yaw moment [34].

- The inclusion of handwheel force feedback in the overall system as a cue to the

driver that the vehicle is nearing its limits, which may result drivers commanding safer vehicle trajectories without controller intervention.

Although these areas are left for future investigation, the contributions of this thesis demonstrate steering torque as an effective means for both the estimation and control of lateral tire forces.

Appendix A

Experimental Studies of τ_a Model on Various Road Conditions

As we learned in Chapter 2, total aligning moment is a useful source of information for tire characterization because it decreases well before tire force saturation due to its dependence on pneumatic trail. By modeling steering torque and lateral force, Chapters 3 and 4 demonstrated experimentally the ability to estimate the tire's friction limits at half the peak tire force and sideslip angle up to the limits of handling. However, experimental studies thus far have been focused on *flat* roads. In order to explore the issues and limitations associated with this method during other types of road conditions, this section investigates the accuracy of the total aligning torque and lateral force models introduced in Chapter 2 under experimental test conditions that include flat and banked roads, road grade, and transient maneuvers.

As before, the vehicle considered here is the steer-by-wire research vehicle, P1 (see Fig. 2.5). However, for this study, P1 is equipped with Hoosier A6 R-compound autocross racing tires, which achieve a friction coefficient of $\mu = 1.3$. This tire modification enables us to validate the force and aligning torque models on a new, high tire-road friction value.

First, this appendix describes the experimental testing conditions. Then, it compares experimental data with the models presented in Chapter 2 Section 2.3.3 in order to determine their applicability in estimating sideslip and friction during these

varying road conditions.

A.1 Test Track

The experimental test runs were conducted on Altamont Motor Sports Park in Altamont, CA. The driven test course is a subset of the overall test track, highlighted in Fig. A.1(a). The course consists of a dry paved road with sharp turns and varying levels of bank angle. For ease of reference, the track is divided into numbered segments from 0 to 6. As illustrated by the shading in Fig. A.1(b), portions of the track are flat (segments 4.5 to 0.5) and portions are banked up to -8 degrees (segments 3.9 to 4.3). The transitions between the flat and banked portions, shown as transitions in color, also exhibit a road grade ranging from approximately 5-10 degrees.

The bank angle of the course was empirically estimated by driving P1 at very slow speeds around the track, minimizing dynamic vehicle roll. The roll angle measured by GPS was recorded as a function of the segment progress from 0 to 6, which functioned as a lookup table to approximate bank angle during later dynamic test runs. Note that because the degree of bank angle increases on the outer edge of the track, this empirical lookup table is only an approximation of the actual course bank angle.

A.2 Experimental Results

The maneuver performed for model validation was obtained by driving P1 multiple times around the track at a constant speed of 17 m/s (38 mph) to heat up the racing tires to the manufactured specified operating temperatures. Figure A.2 illustrates the time history of one loop of the overall maneuver. This loop is representative of the data collected over the entire maneuver. The plot presents the commanded steer angle, GPS-based front slip angle, lateral acceleration, vehicle roll angle corrected for road bank angle, and segment progress along the track. The position of the vehicle recorded by GPS is presented in Fig. A.1(b). With the racing tires, the achieved tire-road friction during the maneuver was $\mu = 1.3$.

(a) Altamont Motor Sports Park

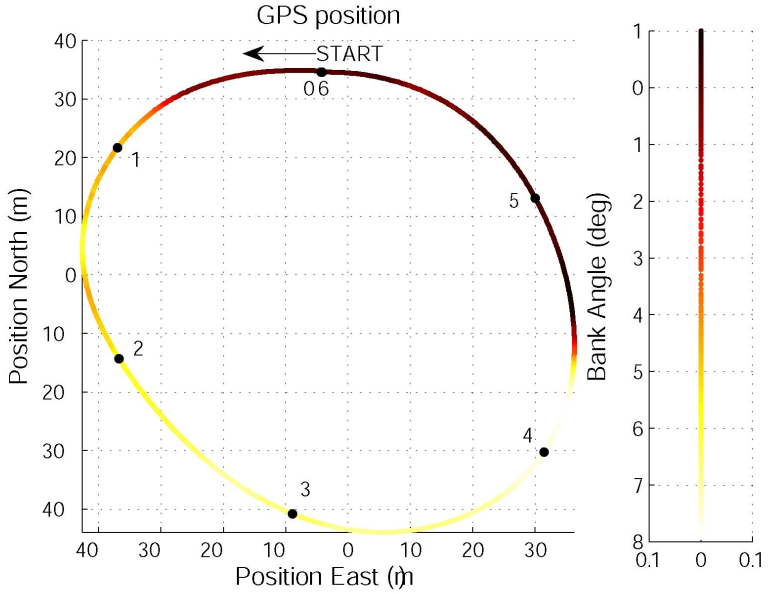

(b) Test Course

Figure A.1: Altamont Experimental Test Track in Altamont, CA

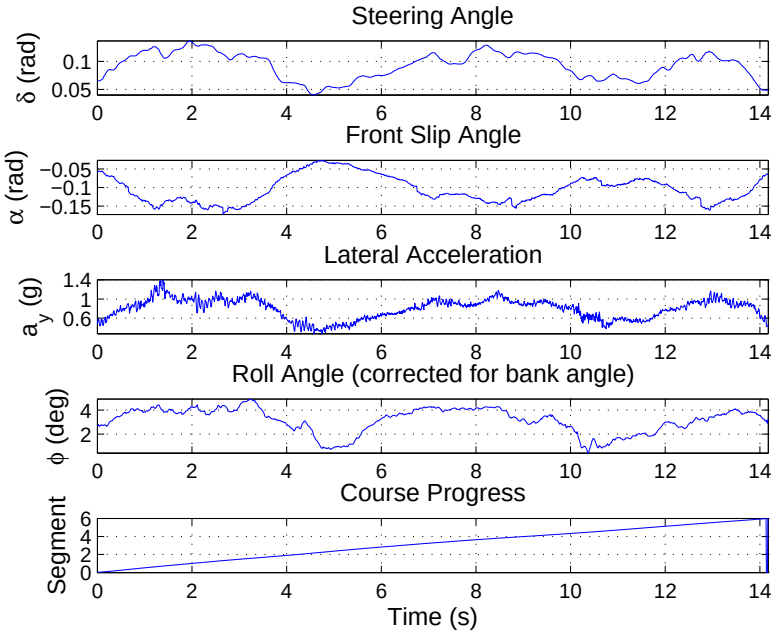

Figure A.2: Maneuver Time History

First, the Fiala model of the front axle lateral force from Section 2.3.3 (which assumes the absence of longitudinal force) is compared to the experimentally measured force derived from the lateral acceleration measurement:

$$F_{yf,meas} = \frac{a_y}{gF_{zf}}. \tag{A.1}$$

where a_y is corrected for bank angle, g is the acceleration due to gravity, and F_{zf} is the nominal front axle normal load. The time history comparison between the model and measured values are shown in Fig. A.3(a).

Overall, the Fiala tire model agrees well with the measured force both during the banked portions and flat portions of the track, i.e. t = 12-14 s and t = 4-10 s, respectively. The model also agrees with experiment during the transient turns. However, during the flat to banked road transition, highlighted in the rectangle overlayed on the plot, there is a noticeable model mismatch where the Fiala model overpredicts

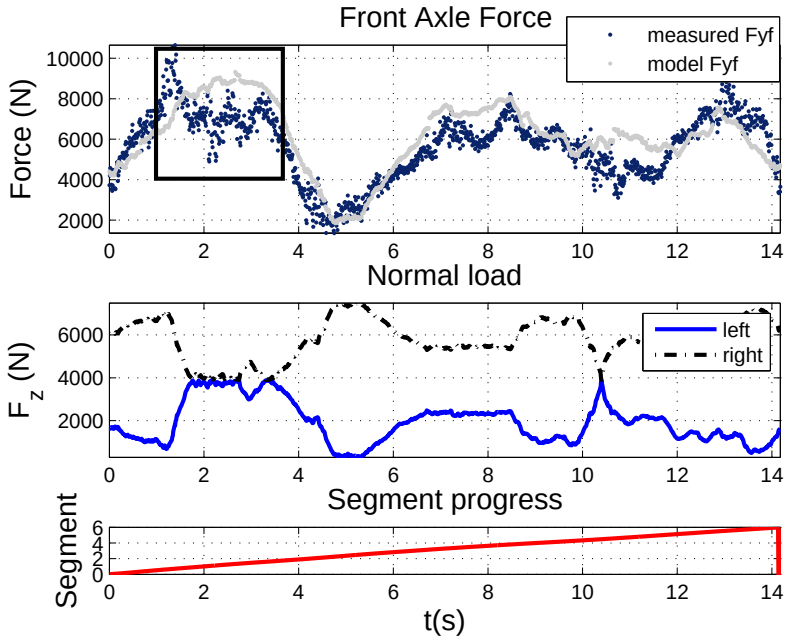

(a) Force Time History

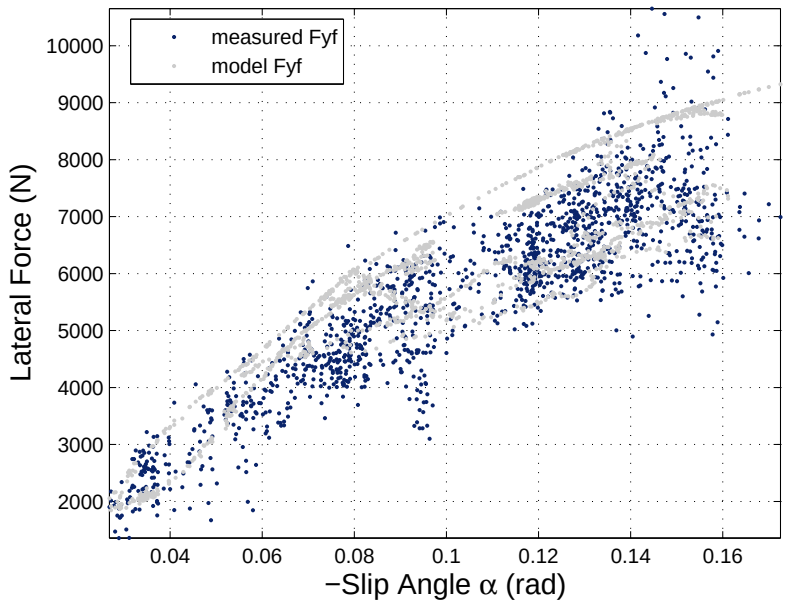

(b) Experimental Tire Curve

Figure A.3: Fiala Lateral Force Model Comparison

the front lateral force. Because the vehicle roll angle with respect to flat ground is close to zero during this time, the load transfer model incorrectly predicts little to no lateral load transfer. In actuality, the uphill change in road grade causes longitudinal weight transfer, shifting the weight of the vehicle to rear and reducing the available normal load on the two front tires. Accordingly, the Fiala model overpredicts the force available on the front axle. This mismatch demonstrates a need for a load transfer model that incorporates longitudinal weight transfer. As illustrated in Fig. A.3(b), despite the model mismatch during the flat the banked transition, the experimental tire curve is described well by the Fiala model.

Second, the total aligning moment model is validated with the torque measured from the onboard load-cells. Figure A.4(a) presents the comparison between the model and experimental data for the left and right sides separately as the maneuver progresses. Similar to the force model results, the total aligning moment model matches well with experiment on the flat and banked portions of the course and during transient maneuvers. During the flat to banked road transition, highlighted in the rectangle in the plot, there is noticeable model mismatch on both sides. The sudden transition to a banked surface causes significant vehicle suspension deflection, causing the outside wheel to experience a heavier load than the inside tire. This accounts for load cells measuring less aligning torque on the inside left tire and more on the outside right tire than the model would predict. This mismatch is illustrated clearly in the torque curves in Fig. A.4(b) highlighted in the boxed regions. However, the aligning torque curve demonstrates that during other portions of the course, the model agrees with experiment.

In summary, both the Fiala force and the total aligning moment models perform well during extreme, transient experimental maneuvers. While there are limitations to the models mainly due to unmodeled effects of longitudinal load transfer and suspension deflection on vertical tire load, both models match well with experiment on flat ground and on banked surfaces where the bank angle is known.

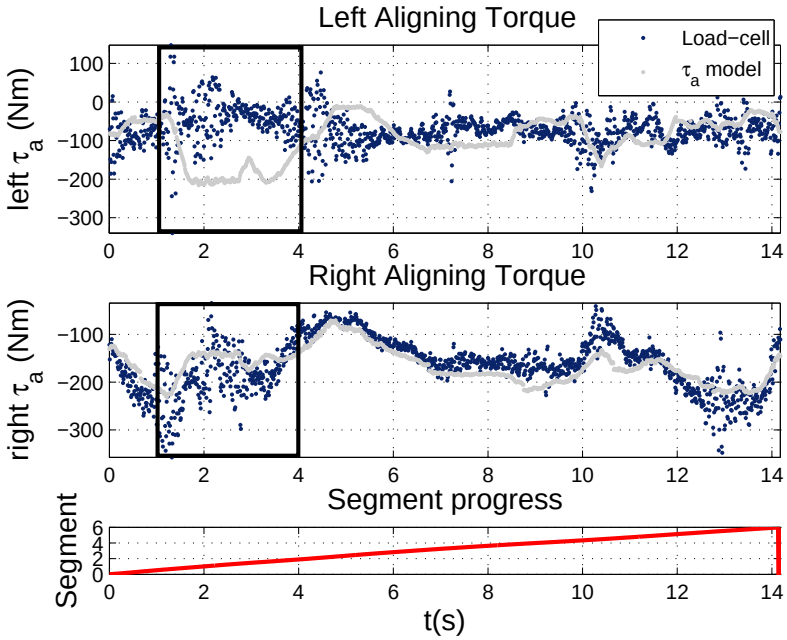

(a) Total Aligning Moment Time History

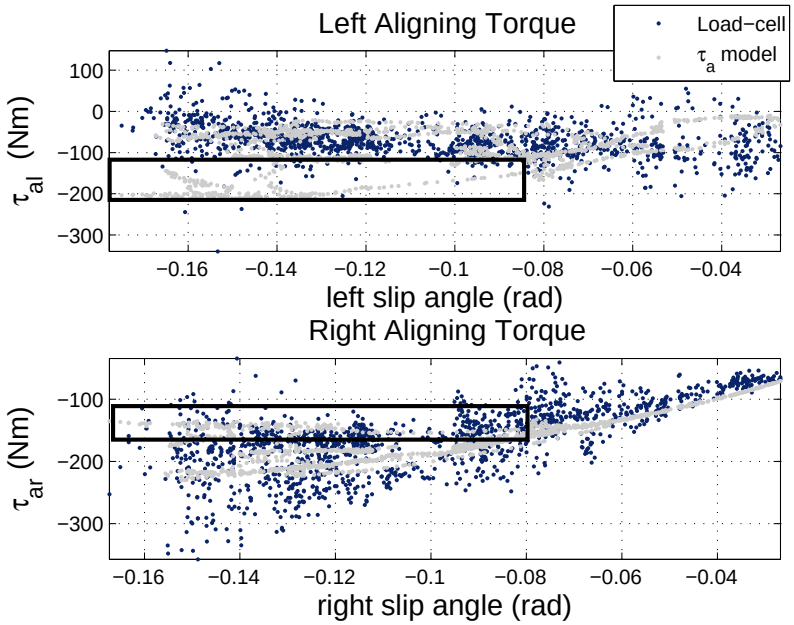

(b) Experimental Total Aligning Moment Curve

Figure A.4: Total Aligning Moment Model Comparison

A.3 Conclusions

The contributions of this thesis have shown that steering torque, along with other available measurements, can provide real-time estimates of vehicle sideslip angle and friction at half the peak tire force. This additional experimental study serves as an extension of this approach. Experiments were performed to validate the lateral force and total aligning moment models on roads that were flat, banked and exhibited altitude changes.

These experiments demonstrated that the models agree well with experiment on flat and banked roads during transient maneuvers when the bank angle is known. Furthermore, the load transfer model used directly affects the accuracy of both lateral force and aligning moment models during extreme lateral maneuvers. Thus, bank angle estimation should be conducted in parallel with estimation methods that use steering torque to characterize tire forces. Finally, a load transfer model is required that includes longitudinal weight transfer and captures the effect suspension deflection due to road grade. Future work should aim to address this issue by instrumenting the research vehicle to measure the load on each tire during dynamic maneuvers to design a more accurate load transfer model.

Bibliography

[1] Electronic stability control coalition fact sheet, 2003. ESC Coalition and DEKRA Automotive Research.

[2] *Bosch Automotive Handbook, 6th Edition*. SAE Society of Automotive Engineers, Inc, 2004.

[3] M. Abe, Y. Kano, Y. Shibihata, and Y. Furukawa. Improvement of vehicle handling safety with vehicle sideslip control by direct yaw moment. *Proceedings of the 16th IAVSD*, 1999.

[4] M. Abe, Y. Kano, K. Suzuki, Y. Shibihata, and Y. Furukawa. An experimental validation of side-slip control to compensate for a loss of stability due to nonlinear tyre characteristics. In *AVEC00*, 2000. Ann Arbor, MI.

[5] M. Aga and A. Okada. Analysis of vehicle stability control (vsc)s effectiveness from accident data. In *Proceedings of the 18th International Technical Conference on the Enhanced Safety of Vehicles*, number 541, 2003.

[6] Guillaume Baffet and Ali Charara. An observer of tire-road forces and friction for active security vehicle systems. *IEEE/ASME Transactions on Mechatronics*, 12(6), 2007.

[7] David M. Bevly, J. Christian Gerdes, Christopher Wilson, and Gengsheng Zhang. The use of GPS based velocity measurements for improved vehicle state estimation. In *Proceedings of the 2000 American Control Conference (ACC), Chicago, Illinois*, 2000.

[8] David M. Bevly, Robert Sheridan, and J. Christian Gerdes. Integrating INS sensors with GPS velocity measurements for continuous estimation of vehicle sideslip and tire comering stiffness. In *Proceedings of the 2001 American Control Conference (ACC), Arlington, Virginia*, 2001.

[9] CarAdvice.com.au. Electronic stability control getting more popular, August 2007.

[10] Christopher R. Carlson and J. Christian Gerdes. Identifying tire pressure variation by nonlinear estimation of longitudinal stiffness and effective radius. In *AVEC02*, 2002.

[11] Andy Chuter. Aibus launches more safety aids. *Flight International*, page 26, 1997.

[12] John Croft. Taming loss-of-control: Solutions are elusive. *Aviation Week & Space Technology*, 157(9):50, August 2002.

[13] John Dixon. *Tires, Suspension and Handling*. Society of Automotive Engineers, Inc, 400 Commonwealth Dr. Warrendale, PA 15096-0001, 1996.

[14] Howard Dugoff, P. S. Fancher, and Leonard Segel. An analysis of tire traction properties and their influence on vehicle dynamic performance. 1970. SAE Paper No. 700377.

[15] Masaya Endo, Kenji Ogawa, and Masahiko Kurishige. Cooperative control of active front steering and electric power steering based on self-aligning torque. *Proceedings of the International Symposium on Advanced Vehicle Control (AVEC), Taipei, Taiwan*, 2006.

[16] Paolo Falcone, Francesco Borrelli, H. Eric Tseng, Jahan Asgari, and Davor Hrovat. Low complexity mpc schemes for integrated vehicle dynamics control problems. In *AVEC08*, 2008.

[17] H.J. Föerster. Der fahrzeugfhrer als bindeglied zwischen reifen, fahrwerk und fahrbahn. *VDI-Berichte*, (916), 1991.

[18] Y. Fukada. Estimation of vehicle slip-angle with combination method of model observer and direct integration. *Proceedings of the International Symposium on Advanced Vehicle Control (AVEC), Nagoya, Japan*, 1998.

[19] Y. Furukawa and M. Abe. On-board-tire-model reference control for cooperation of 4ws and direct yaw moment control for improving active safety of vehicle handling. In *Proceedings of Proceedings of the International Symposium on Advanced Vehicle Control (AVEC)*, 1996. Aachen.

[20] Thomas D. Gillespie. *Fundamentals of Vehicle Dynamics*. Society of Automotive Engineers, Inc, 1992. SAE Order No. R-114.

[21] Havard Fjaer Grip, Lars Imsland, Tor A. Johansen, Thor I. Fossen, Jens C. Kalkkuhl, and Avshalom Suissa. Nonlinear vehicle velocity observer with road-tire friction adaptation. *Proceedings of the 45th IEEE Conference on Decision & Control, San Diego, CA*, 2006.

[22] Hal Gurgenci. Mech3100 - mechanical systems design: Steering, 2001.

[23] Fredrik Gustafsson. Monitoring tire-road friction using the wheel slip. *IEEE Control Systems Magazine*, pages 42–49, 1998.

[24] Jin-Oh Hahn, Rajesh Rajamani, and Lee Alexander. GPS-based real-time identification of tireroad friction coefficient. *IEEE Transactions On Control Systems Technology*, 10(3):331–342, 2002.

[25] Rami Y. Hindiyeh, Kirstin L. R. Talvala, and J. Christian Gerdes. Lanekeeping at the handling limits. In *AVEC08*, 2008.

[26] Yung Hsiang Judy Hsu, Shad Laws, Christopher D. Gadda, and J. Christian Gerdes. A method to estimate the friction coefficient and tire slip angle using steering torque. *Proceedings of ASME International Mechanical Engineering Congress and Exposition (IMECE)*, 2006.

[27] Wookug Hwang and Byung-Suk Song. Road condition monitoring system using tire-road friction estimation. In *AVEC00*, 2000.

[28] U. Kiencke and A. Daib. Observation of lateral vehicle dynamics. *Control Engineering Practice*, 5(8):1145–1150, 1997.

[29] K. Langwieder. Mit esp schwere unfälle vermeiden oder mildern. Technical report, ESP-Workshop, Boxberg, Germany, November 1999.

[30] Tiffany Lapp and Leena Singh. Model predictive control based trajectory optimization for nap-of-the-earth NOE flight including obstacle avoidance. In *ACC2004*, 2004.

[31] Shad Laws, Christopher D. Gadda, Scott Kohn, Paul Yih, J. Christian Gerdes, and J. Craig Milroy. Steer-by-wire suspension and steering design for controllability and observability. *Proceedings of IFAC World Congress, Prague*, 2005.

[32] Li Li, Fei-Yue Wang, and Qunzhi Zhou. Integrated longitudinal and lateral tire/road friction modeling and monitoring for vehicle motion control. *IEEE Transactions on Intelligent Transportation Systems, VOL. 7, NO. 1, MARCH 2006*, 7(1), 2006.

[33] E. K. Liebemann, K. Meder, J. Schuh, and G. Nenninger. Safety and performance enhancement: The bosch electronic stability control (esp). In *Proceedings of International Technical Conference on the Enhanced Safety of Vehicles (ESV)*, 2005.

[34] W.J. Manning and D.A. Crolla. A review of yaw rate and sideslip controllers for passenger vehicles. *Transactions of the Institute of Measurement and Control*, 29(2):117–135, 2007.

[35] Koji Matsuno, Ryi Nitta, Koichi Inoue, Katsufumi Ichikawa, and Yutaka Hiwatashi. Development of a new all-wheel drive control system. In *Seoul FIRSTA World Automotive Congress*, June 2000.

[36] David R. McLellan, Joseph P. Ryan, Edmund S. Browaiski, and John W. Heinricy. Increasing the safe driving envelope - abs, traction control and beyond. In *SAE 92C014*, 1992.

[37] P. Misra and P. Enge. *Global Positioning System: Signals, Measuements and Performance*. Ganga-Jamuna Press, Lincoln, MA, 2001.

[38] Kenji Nakajima, Masahiko Kurishige, Masaya Endo, and Takayuki Kifuku. A vehicle state detection method based on estimated alignment torque using EPS. 2005. SAE Paper No. 2005-01-1265.

[39] NHSTA. Traffic safety facts 2004: A compilation of motor vehicle crash data from the fatality analysis reporting system and the general estimates system. Technical report, National Center for Statistics and Analysis, 2004.

[40] NHTSA. Traffic safety facts research note. 2008. DOT HS 810 936.

[41] David M. North. Finding common ground in envelope protection systems. *Aviation Week & Space Technology*, 153(9):66, August 2000.

[42] Eiichi Ono, Kenji Asano, and Ken Koibuchi. Estimation of tire grip margin using electric power steering system. In *Proceedings of the 18th International Association for Vehicle System Dynamics (IAVSD) Symposium, Kanagawa, Japan*, 2003.

[43] Hans B. Pacejka. *Tire and Vehicle Dynamics*. Society of Automotive Engineers, Inc, 400 Commonwealth Dr. Warrendale, PA 15096-0001, 2002.

[44] Wim R. Pasterkamp and Hans B. Pacejka. Application of neural networks in the estimation of tire/road friction using the tire as sensor. *SAE Paper No. 971122*, 1997.

[45] M. Peden, K. McGee, and E. Krug (Eds.). Injury: A leading cause of the global burden of disease, 2000. Technical report, World Health Organization, 2002. Geneva.

[46] Margie Peden, Richard Scurfield, David Sleet, Dinesh Mohan, Adnan A. Hyder, Eva Jarawan, and Colin Mathers (Eds.). World report on road traffic injury prevention. Technical report, World Health Organization, 2004. Geneva.

[47] Laura Ray. Nonlinear tire force estimation and road friction identification, simulation and experiments. *Automatica*, 33(10):1819–1833, 1997.

[48] Kirstin L. Rock, Sven A. Beiker, Shad Laws, and J. Christian Gerdes. Validating GPS based measurements for vehicle control. *Proceedings of ASME International Mechanical Engineering Congress and Exposition (IMECE)*, 2005.

[49] Jihan Ryu, Eric Rossetter, and J. Christian Gerdes. Vehicle sideslip and roll parameter estimation using GPS. In *AVEC02*, pages 373–380, 2002.

[50] Nilesh A. Sahani. *Envelope Protection Systems for Piloted and Unmanned Rotorcraft*. PhD thesis, Pennsylvania State University, 2005.

[51] Nilesh A. Sahani and Joseph F. Horn. Command limiting for full-envelope guidance and control of rotorcraft. In *AIAA Guidance, Navigation, and Control Conference and Exhibit*, 2005. AIAA 2005-6348.

[52] H. Sakai. Theoretical and experimental studies on the dynamic properties of tyres part 4: Investigations of the influences of running conditions by calculation and experiment. *Int. J. of Vehicle Design, No. 3*, 3:333–375, 1982.

[53] Shankar Sastry. *Nonlinear Systems: Analysis, Stability, and Control*. Springer-Verlag New York, Inc, 175 Fifth Avenue, New York, NY 10010, 1999.

[54] K. H. Senger and W. Schwartz. The influence of a four wheel steering system on the stability behaviour of a vehicledriver system. *Vehicle System Dynamics Supplement*, 17, 1987.

[55] Wolfgang Sienel. Estimation of the tire cornering stiffness and its application to active car steering. In *Proceedings of the 36th Conference on Decision & Control, San Diego, California*, December 1997.

[56] C. Sierra, E. Tseng, A. Jain, and H. Peng. Cornering stiffness estimation based on vehicle lateral dynamics. *Vehicle System Dynamics*, 44:1:24–38, 2006.

[57] Nicholas D. Smith. Understanding parameters influencing tire modeling. *Formula SAE Platform*, 2004.

[58] Andrew G. Sparks, James M. Buffington, and Siva S. Ban. Fighter aircraft lateral axis full envelope control law design. In *Second IEEE Conference on Control Applications, Vancouver, B.C.*, 1993.

[59] Joanny Stephant, Ali Charara, and Dominique Meizel. Virtual sensor: Application to vehicle sideslip angle and transversal forces. *IEEE Transactions on Industrial Electronics*, 51(2), 2004.

[60] Claire Tomlin, John Lygeros, and Shankar Sastry. Aerodynamic envelope protection using hybrid control. In *American Control Conference*, pages 1793–1796, 1998.

[61] Hongtei Eric Tseng. Dynamic estimation of road bank angle. *Vehicle System Dynamics*, 36(4-5), 2001.

[62] Suraj Unnikrishnan. *Adaptive Envelope Protection Methods for Aircraft*. PhD thesis, Georgia Institute of Technology, August 2006.

[63] Anton T. van Zanten. Evolution of electronic control systems for improving the vehicle dynamic behavior. In *AVEC02*, pages 7–15, 2002.

[64] P. J. T. Venhovens and K. Naab. Vehicle dynamics estimation using kalman filters. *Vehicle System Dyanmics*, 32:171–184, 1999.

[65] Klaus H. Well. Aircraft control laws for envelope protection. In *AIAA Guidance, Navigation, and Control Conference and Exhibit*, 2006. AIAA 2006-6055.

[66] J.C. Whitehead. Four wheel steering: maneuverability and high speed stabilisation. *Proceedings of the SAE*, 1988. Detroit, MI.

[67] X. Xia and E. H. Law. Nonlinear dynamic response of four wheel steering automobiles to combined braking and steering commands in collision avoidance maneuvers. *Proceedings of SAE*, 1990. Detroit, MI.

[68] Yoshiyuki Yasui, Wataru Tanaka, Yuji Muragishi, Eiichi Ono, Minekazu Momiyama, Hiroaki Katoh, Hiroaki Aizawa, and Yuzo Imoto. Estimation of lateral grip margin based on self-aligning torque for vehicle dynamics enhancement. *SAE 2004-01-1070*, 2004. SAE Paper No. 2004-01-1070.

[69] Ilkay Yavrucuk, Suraj Unnikrishnan, and J.V.R. Prasad. Envelope protection in autonomous unmanned aerial vehicles. In *American Helicopter Society 59th Annual Forum, Phoenix, Arizona*, 2003.

[70] Paul Yih and J. Christian Gerdes. Steer-by-wire for vehicle state estimation and control. In *Proceedings of the International Symposium on Advanced Vehicle Control (AVEC), Arnhem, The Netherlands*, 2004.

[71] Paul Yih, Jihan Ryu, and J. Christian Gerdes. Vehicle state estimation using steering torque. In *ACC04*, 2004.